CZECH TECHNICAL UNIVERSITY IN PRAGUE

Faculty of Civil Engineering
Department of Geomatics

Processing of hyperspectral data

DOCTORAL THESIS

Ing. Jan Hanuš

Doctoral study programme: Geodesy and Cartography
Branch of study: Geodesy and Cartography

Doctoral thesis tutor: prof. Dr. Ing. Karel Pavelka

Prague, 2023

CZECH TECHNICAL UNIVERSITY IN PRAGUE
Faculty of Civil Engineering
Thákurova 7, 166 29 Praha 6

DECLARATION

Ph.D. student's name: Ing. Jan Hanuš

Title of the doctoral thesis: Processing of hyperspectral data

I hereby declare that this doctoral thesis is my own work and effort written under the guidance of the tutor prof. Dr. Ing. Karel Pavelka. All sources and other materials used have been quoted in the list of references.

In Brno on ………………   …………………………
                                                                    signature

Abstrakt

Hyperspektrální obrazová data získávají v oblasti dálkového průzkumu stále větší prostor. Tradičnější letecká nebo pozemní obrazová hyperspektrální data začínají častěji doplňovat data snímaná z družic. Technologie výroby a miniaturizace hyperspektrálních senzorů pokročila natolik, že relativně kvalitní obrazová data dokážeme nasnímat i z bezpilotních prostředků. Tato disertační práce se bude zabývat zejména leteckými hyperspektrálními daty a postupy při jejich snímání, zpracování a analyzování. První část práce je věnována popisu vývoje metod pro snímání a zpracování hyperspektrálních dat. Druhá část se zabývá využitím a analýzou dat z hyperspektrální laboratoře. Výsledky výzkumu byly publikovány ve vědeckých časopisech nebo sbornících konferencí registrovaných v databázi Web of Science. Disertační práce je předložena jako komentovaný soubor článků.

Klíčová slova: hyperspektrální data, obrazová spektroskopie, zpracování dat, radiometrické korekce, geometrické korekce, atmosférické korekce, laserový skener, termální data

Abstract

Hyperspectral imagery is becoming increasingly important in remote sensing. Traditional airborne or ground-based hyperspectral imagery is more often complemented by satellite imagery. The technology for production and miniaturisation of hyperspectral sensors has advanced to the point where relatively high quality imagery can be acquired from unmanned airborne systems. In particular, this thesis focuses on hyperspectral airborne data and the methods used to acquire, process and analyse them. The first part of the thesis is dedicated to the description and development of methods for the acquisition and processing of hyperspectral data. The second part deals with the use and analysis of the data produced by the hyperspectral laboratory. The research results were published in scientific journals or conference proceedings registered in the Web of Science database. The thesis is presented as a commented set of articles.

Keywords: hyperspectral data, imaging spectroscopy, data processing, radiometric corrections, geometric corrections, atmospheric corrections, laser scanner, thermal data

Acknowledgement

Here I would like to thank many people who helped to reach the possibility of submitting my doctoral thesis. First of all, I would like to thank my supervisor Karel Pavelka, who guided me through my doctoral studies.

My gratitude belongs to the team at the Academy of Sciences (Global Change Research Institute - CzechGlobe) where I work. First of all, to the director Michal V. Marek and Zbyněk Malenovský, whose visions were at the beginning of establishing the hyperspectral remote sensing team. The team has developed over the years, so I really appreciate the help and support I received from the whole team, especially from Lucie Homolova, Tomáš Fabiánek, Lukáš Slezák and Lukáš Fajmon.

Last but not least, I would like to thank my family for always encouraging me in times when my motivation was low.

List of Articles

The doctoral thesis is prepared as a commented series of articles published in scientific journals.

1) HANUŠ, J., SLEZÁK, L., FABIÁNEK, T., FAJMON, L., HANOUSEK, T., JANOUTOVÁ, R., KOPKÁNĚ, D., NOVOTNÝ, J., PAVELKA, K., PIKL, M., ZEMEK, F., HOMOLOVÁ, L., Flying Laboratory of Imaging Systems: Fusion of Airborne Hyperspectral and Laser Scanning for Ecosystem Research. *Remote Sensing.* 2023, 15(12)), 3130. E-ISSN 2072-4292. doi: 10.3390/rs15123130.

2) BÁRTA, V., HANUŠ, J., DOBROVOLNÝ, L., HOMOLOVÁ, L., Comparison of field survey and remote sensing techniques for detection of bark beetle-infested trees. *Forest Ecology and Management.* 2022, 506(FEB)), 119984. ISSN 0378-1127. E-ISSN 1872-7042. doi: 10.1016/j.foreco.2021.119984.

3) SKOUPÝ, O., ZEJDOVÁ, L., HANUŠ, J., The use of hyperspectral remote sensing for mapping the age composition of forest stands. *Journal of Forest Science.* 2012, 58(6), 287-297. ISSN 1212-4834.

4) VINCIKOVÁ, H., HANUŠ, J., PECHAR, L., Spectral reflectance is a reliable water-quality estimator for small, highly turbid wetlands. *Wetlands Ecology and Management.* 2015, 23(5), 933-946. ISSN 0923-4861. E-ISSN 1572-9834. doi: 10.1007/s11273-015-9431-5

Two articles, which were previously published in conference proceedings, were included. The author of the thesis considered them to be important for a comprehensive description of the historical development of the hyperspectral laboratory.

0a) HANUŠ, J., FABIÁNEK, T., KAPLAN, V; ZEMEK, F., Airborne imaging spectroscopy at CzechGlobe – potential, data processing and quality indicators. International Multidisciplinary Scientific GeoConference Surveying Geology and Mining Ecology Management, SGEM, 2, pp. 557–563, 2013, ISBN 978-954-91818-9-0, doi: 10.5593/SGEM2013/BB2.V2/S10.002, ISSN: 1314-2704, 2013

0b) HANUŠ, J., FABIÁNEK, T., FAJMON, L., Potential of airborne imaging spectroscopy at CzechGlobe. In: *XXIII ISPRS Congress: Technical Commission VII.* Vol. 2016. Göttingen: Copernicus Gesselschaft, 2016, s. 15-17. International Archives of the Photogrammetry Remote Sensing and Spatial Information Sciences, 41 B1. ISSN 1682-1750. doi: 10.5194/isprsarchives-XLI-B1-15-2016

List of Abbreviations

3D	three dimensional
AISA	Airborne Imaging Spectroradiometer
ASD	Analytical Spectral Devices, Inc.
ATCOR	Atmospheric / Topographic Correction
BBT	Broadband Brightness Temperature
CAS	The Czech Academy of Sciences
CCD	Charge-Coupled Device
CzechGlobe	Global Change Research Institute CAS
DEM	Digital Elevation Model
DLR	Deutsches Zentrum für Luft- und Raumfahrt e. V.
DSM	Digital Surface Model
DTM	Digital Terrain Model
ESA	European Space Agency
FLAASH	Fast Line-of-sight Atmospheric Analysis of Spectral Hypercubes
FLEX	FLuorescence EXplorer
FLIS	Flying Laboratory of Imaging Systems
FLIS	Flying Laboratory of Imaging Systems
FODIS	Fiber Optic Downwelling Irradiance Sensor
FOV	Field of View
FUB	Freie Universität Berlin
FZJ	Forschungszentrum Jülich
GFZ	GeoForschungZentrum
GNSS	Global Navigation Satellite System
chl-a	chlorophyll-a
IMU	Inertial Measurement Unit
INTA	Instituto Nacional de Técnica Aerospacial
JRA	Joint Research Activity
LiDAR	Light Detection and Ranging
LIST	Luxembourg Institute of Science and Technology
LST	Land Surface Temperature
LWIR	Long Wave Infrared
MODTRAN	MODerate resolution atmospheric TRANsmission
nDSM	normalised DSM
NEON	National Ecological Observatory Network
ONERA	Office National d'Etudes et de Recherches Aerospatiales
PML	Plymouth Marine Laboratory
PRISMA	Precursore Iperspettrale della Missione Applicativa
SWIR	Short Wave Infrared
TAU	Tel Aviv University
TSS	total suspended solids
UAS	Unmanned Airborne System
UZH	University Of Zurich
VITO	Vlaamse Instelling voor Technologisch Onderzoek
VNIR	Visible and Near Infrared
WUR	Wageningen University
ε	emissivity

Table of Content

Chapter 1

1   Introduction

The doctoral thesis is prepared as a commented set of published articles showing the continuous development of the hyperspectral laboratory at the Global Change Research Institute CAS and examples of its use.

Airborne imaging spectroscopy techniques, often referred to as airborne hyperspectral remote sensing, were firstly introduced in the1980s (Vane et al., 1984) and provide powerful tools for spatial and temporal monitoring of landscapes at local to regional scales. Unlike traditional multispectral data, hyperspectral imagery provides continuous coverage of electromagnetic spectrum, and hyperspectral sensors measure hundreds to thousands of contiguous narrow spectral bands, allowing the capture of complete 'spectral signatures' of the Earth's surface rather than discrete values from multi spectral sensors. This capability enables the development of new methods for detecting Earth surface objects with high accuracy and retrieving surface properties quantitatively. Today, almost half a century after the first use of hyperspectral sensors, imaging spectroscopy is still evolving and the first reliable satellite data are becoming available.

The applications of hyperspectral remote sensing data span a wide range of scientific and commercial domains, making it a versatile tool for mapping and facilitating valuable insights. In the agricultural sector, hyperspectral data supports yield prediction and precision agriculture, optimising agricultural practices (Klem et al., 2018) for greater efficiency. In forestry, it enables monitoring of forest health status (Mišurec et al., 2012), biomass estimation (Brovkina et al., 2017) and species composition mapping, contributing to sustainable forest management. In geology, hyperspectral imaging plays an important role in mineral mapping and land degradation assessment, supporting resource exploration and environmental monitoring.

In addition, hyperspectral remote sensing finds applications in limnology for the assessment of water quality (Vinciková et al., 2013), contributing to the conservation and management of aquatic ecosystems. Furthermore, its use extends to various other fields, including military applications, where it supports target detection (Bárta and Hanuš, 2018) and reconnaissance efforts.

The accessibility and availability of hyperspectral data have increased its usage in both scientific (Hanus et al., 2013) and commercial communities. The rich information provided by hyperspectral imagery can provide researchers and decision-makers with comprehensive insights into Earth's surface dynamics. It can aid informed decision-making across multiple disciplines.

To summarize, hyperspectral remote sensing from airborne platforms provides an innovative and evolving approach to Earth observation, enabling comprehensive and detailed monitoring of land surfaces. Hyperspectral imaging plays an important role in advancing various fields of study and supporting sustainable practices in natural resource management and environmental protection, thanks to its wide range of applications and continuing technological advances.

1.1   Goals of the thesis

The thesis has two main goals. The first goal, outlined in chapter 2, is to develop and establish a data pre-processing chain for data produced by the hyperspectral laboratory. This involves mainly the development of a pre-processing chain for VNIR and SWIR sensors, as well as implementing upgrades. The second goal, discussed in chapter 3, focuses on describing the possible utilization of the hyperspectral laboratory and the related data analysis, again primarily in the VNIR and SWIR spectral regions.

Chapter 2

2 Development of hyperspectral laboratory

Since 2004 the Global Change Research Institute, which use short name CzechGlobe (Academy of Sciences of the Czech Republic) has been developing a laboratory for hyperspectral imaging.

The Institute has been operating the AISA Eagle airborne hyperspectral sensor, which covers the VNIR region. Sensor was developed by Spectral Imaging (Specim Ltd, Finland) and was usually installed on an aircraft of Argus Geo System Ltd.

From 2014 to 2016, CzechGlobe's hyperspectral laboratory was significantly improved, and a European-level Flying Laboratory of Imaging Systems (FLIS) was built. Currently, FLIS consists of an airborne carrier Cessna Grand Caravan C208B, which is equipped with hyperspectral sensors covering the VNIR, SWIR, and LWIR spectral regions. These sensors are provided by the Canadian company Itres. In addition, FLIS has been equipped with an airborne laser scanner.

The development of the laboratory and processing chains is described in the following subchapters.

2.1 Development of data pre-processing chain

Development of a hyperspectral laboratory is more structural task with necessity to properly balance properties of each sensor to create complementary unit, which ended by proper assemble of all components. The development of a data pre-processing chain is never-ending task, that must be properly designed for each sensor and its changing performance. The data pre-processing chain needs to be designed such way that final product, in the case of imaging spectroscopy usually georeferenced at surface reflectance, is delivered to the user in a standardized way. Several basic steps are involved in the pre-processing of hyperspectral data.

The first step is to perform radiometric correction, which converts raw digital numbers into radiance values. During radiometric correction, it is possible to apply other corrections to remedy unwanted influences that negatively affect the acquired hyperspectral data. For example, scattered light correction, frame shift smear correction, second order light correction, etc. Radiometric corrections are typically based on procedures recommended by the sensor designer. Nonetheless, it is always necessary to check the performance and make minor improvements designed specifically for the sensor. This is described, for example, in Purket et al. (2019) and it results in improved data quality. For some lightweight sensors designed for UAS, it could be advantageous to revise the entire processing chain recommended by the producer, like is described in Minařík et al. (2019).

The next step involves geo-referencing the image data. This process for airborne imaging spectroscopy data includes making geometric corrections to compensate for aircraft movements, orthogonalizing based on the sensor's optical model and the Digital Elevation Model (DEM), and resampling the data into the desired coordinate system. Geo-referencing is typically done using software developed by the sensor producer or programs specifically designed for pushbroom sensors (Schläpfer and Richter, 2002). The output quality of these programs should be tested for all sensors. Developers of these programs often welcome feedback and continuously improve the software. However, a perfectly functioning program still relies on the quality of its inputs, which should be checked and potentially improved, as suggested by Slezák et al., (2021).

The most critical part of the hyperspectral data pre-processing chain is usually the application of atmospheric corrections. There are typically two ways of correctly performing atmospheric corrections on hyperspectral data cubes. The most straightforward method is to perform the empirical line vicarious correction using ground reference targets with known spectral properties. This correction can be beneficially used for ground-based image acquisitions (Ač et al., 2009) or is typically used for smaller areas acquired by UAS (Minařík et al., 2019). For small areas with homogeneous topography, the use of simple empirical line correction (Smith and Milton, 1999) is the most effective approach (Ben-Dor et al., 2013).

Data acquired at the regional scale, with variable topographic or even atmospheric conditions, could be effectively corrected using radiative transfer models. This is currently the most common and universal approach. Atmospheric corrections can be coupled with other corrections such as topographic or nadir normalization corrections. For the atmospheric correction of hyperspectral data, the MODTRAN radiative transfer

model (Berk et al., 1999) progressively dominated and is commonly used. Software packages such as FLAASH or ATCOR (Schläpfer and Richter, 2002) use the MODTRAN for atmospheric correction of hyperspectral data.

Articles describing history of the hyperspectral laboratory are presented below. Two historically oldest articles (0a, 0b) were presented to the scientific community within conference proceedings.

2.2 Articles

2.2.1 Article 1

Flying Laboratory of Imaging Systems: Fusion of Airborne Hyperspectral and Laser Scanning for Ecosystem Research

The article presents the fully equipped Flying Laboratory of Imaging Systems (FLIS). Operated by the Global Change Research Institute of the Czech Academy of Sciences (CzechGlobe), FLIS consists of three commercial imaging spectroradiometers that cover the visible, near-infrared, shortwave infrared, and thermal infrared regions of the electromagnetic spectrum. Furthermore, FLIS is equipped with a full waveform laser scanning system, which enables the acquisition of 3D landscape data. This platform enables the synchronous acquisition of multiple data sources that, in turn, provides a complex analytical and data framework for assessing various vegetation ecosystems, such as plant species composition, functional traits, biomass, and carbon stocks.

FLIS aims to operate as an infrastructure for the acquisition of remote sensing data of high quality. This data should be capable of facilitating the study of complex and long-term ecosystem research, including the processes and fluxes of energy and matter, within and between ecosystems at corresponding spatial scales. The platform's versatility will make it a valuable tool for identifying synergies between observations from different sources, at different times and at different scales. It is therefore an beneficial tool for addressing complex ecological questions. In recent decades, remote sensing technology has become an increasingly important information source on ecosystem status and change. It has now grown to become an very important source of such information.

Satellite data provide important insights into global trends and changes in forest cover, vegetation phenology and ecosystem evapotranspiration, including acquisitions from global coverage providers such as Landsat and Copernicus Sentinels. Nevertheless,

satellite data's restricted spatial resolution makes it unsuitable for analysing local patterns. On the other hand, unmanned aerial systems (UAS) and airborne remote sensing platforms such as FLIS establish a connection between broad-scale satellite observations and narrow-scale field measurements. Airborne high spatial resolution data are useful to suit particular research objectives and seamless integration with field campaigns. Airborne data play a significant role in calibrating and validating satellite products, simulating future satellite data, and retrieving various landscape elements structural and functional properties with high spatial detail.

The design of FLIS and its instrument configuration enable it to acquire data for wide range of research requirements. Combining hyperspectral scanners, thermal sensors, and laser scanning capabilities enables researchers to investigate biochemical properties of vegetation, soil characteristics, water properties, surface emissivity, temperature properties, landscape orography, and 3D structure. Simultaneously acquiring these diverse datasets offers comprehensive information for assessing various aspects of ecosystems, making FLIS a valuable asset for ecological research.

FLIS has a noteworthy capability in supporting the study of urban ecosystems. The dataset provided by high-resolution reflectance and thermal data, combined with detailed digital terrain and surface models obtained from laser point clouds, is useful in evaluating the relationship between 3D urban structures, properties of urban elements, and thermal performance. Urban planners highly require such detailed information, however its acquisition from satellite data is impossible due to limited spatial resolution in the thermal domain and legal restrictions on UAS flights in populated areas.

Similar systems to FLIS exist in the United States and Europe. FLIS, however, distinguishes itself as one of the fully operational platforms in Europe, providing researchers with valuable data primarily for ecosystem research. Additionally, the platform facilitates calibration and validation activities for ongoing and upcoming satellite missions; for example, FLEX, with the purpose of mapping global photosynthetic activity through sun-induced fluorescence measurements from space or PRISMA.

The FLIS data pre-processing chain ensures the reliability and accuracy of the acquired data. The process involves radiometric corrections, georeferencing, fusion of hyperspectral data cubes, atmospheric corrections, and the extraction of 3D point cloud data from laser scanning. The data products derived from FLIS include surface

reflectance, land surface temperature, land surface emissivity, and digital terrain and surface models.

In conclusion, the Flying Laboratory of Imaging Systems (FLIS) plays an important role in advancing ecosystem research through its operational multi-sensor platform. The multi-sensor platform can acquire optical, thermal, and laser scanning data simultaneously which provides researchers with extensive datasets for studying various aspects of terrestrial ecosystems, vegetation, and urban environments. The platform's versatility, high spatial resolution, and synchronization of multiple data sources make it a useful tool for addressing complex ecological questions and supporting calibration/validation activities for satellite missions. FLIS contributes significantly to the understanding of ecosystem dynamics and helps pave the way for sustainable land management and environmental conservation efforts.

The article is attached as appendix 1 of the thesis.

2.2.2   Article 0a

Airborne imaging spectroscopy at CzechGlobe – potential, data processing and quality indicators

HANUŠ, J., FABIÁNEK, T., KAPLAN, V; ZEMEK, F... International Multidisciplinary Scientific GeoConference Surveying Geology and Mining Ecology Management, SGEM, 2, pp. 557–563, 2013, ISBN 978-954-91818-9-0, doi: 10.5593/SGEM2013/BB2.V2/S10.002, ISSN: 1314-2704, 2013

The article describes the hyperspectral laboratory that was established at CzechGlobe, as well as the processing chains that include quality layers that were developed for users.

The article briefly introduces airborne hyperspectral remote sensing, also called imaging spectroscopy. Airborne imaging spectroscopy offers unique tools for monitoring landscapes spatially and temporally. In contrast to traditional multispectral data, hyperspectral data provides almost continuous coverage of electromagnetic spectra, capturing "spectral profiles" instead of discrete values. This enables accurate

object detection and quantitative surface property retrieval to be developed. Hyperspectral remote sensing is widely used in agriculture, forestry, geology, limnology, and even military domains.

The article shortly describes the AISA Eagle sensor, which was operated by the Global Change Research Institute, also known as CzechGlobe. The AISA Eagle is an airborne hyperspectral pushbroom system, which was manufactured by the Finnish company Specim Ltd.

The main topic of this article is the pre-processing chain developed at CzechGlobe, followed by possible branches of processing. To pre-process hyperspectral data, radiometric, geometric, and atmospheric corrections are necessary. To perform these corrections software packages such as CaliGeo, PARGE, and ATCOR-4 were used to perform geo-orthorectification, radiometric and atmospheric compensation. To perform atmospheric correction, several approaches were employed, including empirical methods, FODIS ratio (an empirical method based on an irradiance sensor mounted on the aircraft fuselage), and radiative transfer models.

This article contains a significant section about quality layers created for the AISA Eagle instrument and integrated into the CzechGlobe pre-processing chain. The quality layers were developed within the EUFAR FP7 project, respectivelly Joint Research Activity No.2 - HYQUAPRO (JRA2). The HYQUAPRO activity included several hyperspectral data providers and users, such as DLR, TAU, VITO, ONERA, PLM, CzechGlobe, WU, UZH, INTA, FUB. The HYQUAPRO activity led to the production of 13 standardized quality layers. Additionally, each data operator integrated relevant quality layers into its pre-processing chain, and eventually, created and integrated quality layers that were specific to their pre-processing chain. Quality layers integrated into the CzechGlobe pre-processing chain are described at Bachmann et al. (2011).

Finally, the article outlines possible future development of the hyperspectral laboratory at CzechGlobe.

The article is attached as appendix 5 of the thesis.

2.2.3 Article 0b

Potential of airborne imaging spectroscopy at CzechGlobe

This article details the transformation of the hyperspectral laboratory at CzechGlobe, from a single-sensor operator to a fully equipped hyperspectral laboratory including an airborne carrier. The laboratory was named the Flying Laboratory of Imaging Systems (FLIS) and consists of an airborne carrier equipped with hyperspectral sensors that acquire data in the VNIR, SWIR, and LWIR spectral regions. This article also describes the pre-processing chain developed for new hyperspectral sensors, specifically the one designed for hyperspectral thermal data. The article also outlines the geo-referencing and quality assessment methods employed.

The pre-processing chain for hyperspectral data includes radiometric, geometric, and atmospheric corrections. Radiometric correction involves laboratory determined calibration parameters, whereas atmospheric correction uses radiative transfer models or empirical methods. The mentioned apparent reflectance method is suitable for some remote sensing applications where part of the atmospheric effects may remain uncorrected.

For thermal data, atmospheric corrections are conducted using specific procedures, and relies on a radiative transfer model incorporating atmospheric variables gained from external sources e.g. MODIS. The text further explains the process of geo-referencing, which involves compensating for geometric distortions and resampling image data into a desired coordinate system.

The FLIS platform, which is operated by CzechGlobe - Global Change Research Institute, enables sophisticated monitoring of ecosystems at different scales. The hyperspectral sensors on the FLIS platform cover the visible, near-infrared, short-wave infrared and thermal spectral ranges, providing detailed spectral information about the Earth's surface.

The article highlights the significance of quality assessment to verify the accuracy of atmospheric, radiometric and geo-referencing corrections. This is achieved through a comparison with ground-measured spectra and Ground Control Points.

Finally, the article discusses the utilization of the FLIS platform for ecosystem monitoring, using hyperspectral sensors. It mainly highlights the pre-processing steps for hyperspectral and thermal data, as well as the geo-referencing and quality assessment methods. The text also mentions that the laboratory is ready for the installation of an airborne laser scanner.

The article is attached as appendix 6 of the thesis.

Chapter 3

3 Utilization of the hyperspectral laboratory

The FLIS hyperspectral laboratory, operated by CzechGlobe, presents an advantageous resource for ecological research, providing dependable information to researchers. The complex design of the laboratory supports the convenient utilization of all onboard sensors for heterogeneous forest ecosystems. The laboratory applies hyperspectral optical sensors for the estimation of vegetation traits. Additionally, it employs an airborne laser scanner for assessing forest structure (Novotný et al., 2023) and a thermal sensor to help estimate the water regime, thereby providing a comprehensive analysis of ecological systems. The use of the FLIS hyperspectral laboratory for forestry was described in Malenovský et al. (2013) or Hovi et al. (2022). From a social perspective, the utilisation of the infrastructure for conducting research in agriculture (Klem et al., 2018) and food security in general, is of even greater importance. However, the utilisation of the hyperspectral laboratory at CzechGlobe is primarily focused on vegetation, although other research areas are also explored, mainly in collaboration with other research institutions. For instance, research conducted at the hyperspectral laboratory includes estimation of soil composition or water quality of inland water bodies (Orság et al., 2023; Vinciková et al., 2013).

The importance of studying the urban environment, specifically the urban heat islands and perceived temperature, has increased over the last year (Urban et al., 2022). FLIS

provides continuous spectral measurements in the VNIR and SWIR region, supported by thermal and laser scanner measurements. It can be used for various research and applications, ranging from traditional vegetation, soil and water exploitation to satellite calibration, archaeology, or military tasks (Bárta and Hanuš, 2018). In general, the usage of FLIS, like other instruments developed by humans, is constrained solely by people's imaginations.

With the increasing accessibility and reliability of hyperspectral satellite data, airborne hyperspectral remote sensing would be less effective for traditional study areas like soil and water, where spatial resolution plays a minor role. The availability of UAS equipped by hyperspectral sensors has increased, making them ideal for local field experiments such as phenotyping. However, this has led to a narrowing of the niche for airborne remote sensing research. On the other hand, the quality and complexity of sensors that can be installed on aircraft exceed the sensors available for UAS. Sensors mounted on satellite platforms also need to be tested at airborne levels. The niche for airborne remote sensing research is narrowing, but aircraft still plays a vital role in remote sensing research. In the next few years, applications developed by means of airborne remote sensing will likely focus on heterogeneous urban or forest environments.

3.1 Articles

3.1.1 Article 2

Comparison of field survey and remote sensing techniques for detection of bark beetle-infested trees

This article investigates the possibilities for early detection of bark beetle infestations, which is important for proactive forest management in Central European forests. Remote sensing methods are increasingly popular for this purpose, allowing for the monitoring of infestations even at the level of individual trees. The focus of this study was to compare remote sensing methods (using the VNIR airborne sensor) to classical field surveys in their ability to detect newly infested trees.

The introduction provides context on the threat that bark beetles pose to Eurasian forests. This threat became particularly evident during the outbreak from 2015 to 2019, leading to an increase in salvage felling. Due to long-term drought and rising temperatures, European countries experienced high rates of salvage felling, which benefited the expansion of bark beetles. To address the increased spread of bark beetles caused by rising temperatures, the study highlights the importance of multiple forms of data collection. These include remote sensing, field surveys, and phenology modelling, to prevent massive outbreaks and economic losses.

The common practice of bark beetle monitoring in the Czech Republic involved laborious and time-consuming field surveys to locate infested trees based on specific traits accompanying bark beetle attack. In contrast, remote sensing presented an effective tool for large-scale monitoring using hyperspectral data, capable of supporting individual tree-level approaches. The study employed aerial hyperspectral scans with a spatial resolution of 0.5 m, spectral resolution 15nm and mapped the transition from healthy to red-attack stages of almost 100 infested Norway spruce trees and the similar number of healthy trees. Several spectral indices were analysed to differentiate between healthy and infested trees, with emphasis on chlorophyll absorption and near-infrared regions. The study showed that indices using red and red-edge regions detected infestation earlier than those using near-infrared spectral information.

The study discussed utilizing phenology models to determine the ideal time for obtaining remote sensing data for bark beetle infestation detection. The authors emphasized that combining remote sensing data, field surveys, and phenology models for bark beetle development could facilitate improved planning and timing of forest management strategies to address bark beetle infestations.

The conclusion of the study highlighted that remote sensing-based detection, despite being delayed by 23 days when compared to field survey in case of this study, can still be considered adequate for proactive management. The article suggests exploring information from SWIR and thermal regions to enhance early detection. To monitor larger areas, the combination of phenology models and local field surveys can determine the most appropriate timing for airborne sensing. In conclusion, the study provides valuable insights into the potential of remote sensing methods and phenology modelling in detecting bark beetle infestations early, which can aid proactive forest management strategies.

The article is attached as appendix 2 of the thesis.

3.1.2   Article 3

The use of hyperspectral remote sensing for mapping the age composition of forest stands

This article explores the possibility of estimating the age composition of tree stands, specifically Norway spruce forest stands, using hyperspectral data. Remote sensing is recognised as a fast-developing method that allows the rapid acquisition and subsequent processing of data. This offers the advantage of creating up-to-date maps of vast areas. The article tests the possibility of retrieving age composition from high spatial resolution hyperspectral data.

Aerial and satellite spectroscopy developed as a specific branch of remote sensing, aiming to improve the identification of surface properties by means of knowledge of continuous spectral profile. Geological investigations have successfully mapped mineral compositions, while studies in forestry have identified specific spectral features of canopy biochemical properties. Recently, ecological investigations have taken the forefront in the research on the use of imaging spectroscopy in forestry.

The study carried out an innovative object-oriented method to analyse the age of forest stands, specifically Norway spruce, using supervised classification algorithms. The study evaluated the Nearest Neighbor (NN) algorithm using eCognition and artificial neural networks (ANN) through ENVI software environment. The findings indicate that age differentiation of spruce stands is possible through spectral characteristics, with higher accuracy achieved by the ANN compared to the NN classifier.

Further verification is needed in various conditions to develop a universally applicable function that estimates stand ages with greater accuracy using this methodology. This methodology shows promise in mapping the age composition of stands consisting of evenly aged groups as well as estimating the average age of unevenly aged stands.

This text offers insights into the possibilities of remote sensing, especially hyperspectral remote sensing, for analysing the species and age composition of forest stands. Although further testing and refinement are necessary for improved accuracy and wider applicability, the object-oriented approach and supervised classification algorithms show promise. This study opens up new avenues for research and implementation in the fields of forestry and remote sensing applications.

The article is attached as appendix 3 of the thesis.

3.1.3 Article 4

Spectral reflectance is a reliable water-quality estimator for small, highly turbid wetlands

The study described in the article was carried out in the Třeboň basin located in South Bohemia. The region is characterized by fishponds and wetlands, making up 15% of the area, with 465 fishponds filling an area of 7.5 km2. The fishponds are artificial water bodies, which are primarily used for fish production, have been in existence for several hundred years. The majority of the water for the fishponds is supplied by the Lužnice River. The study also included flooded quarries that have been transformed into lake-like water bodies. The quarries are several decades old. Younger quarries serve as raw water sources, while older ones are utilised for purposes such as recreation and sport fishing.

Water samples were collected from 28 fishponds and quarries in the Třeboň basin from July to September of 2008 and 2009 for data collection. The laboratory analysed the water samples, and a spectroradiometer was used to take in situ reflectance measurements.

During the work it became necessary to classify the water bodies into three categories and to use specific algorithms for each category. The classification of water bodies was based on their reflectance spectra and the concentration of chlorophyll-a (chl-a) and total suspended solids (TSS). Three distinct spectral classes were identified: oligotrophic waters, low chl-a waters and high chl-a and TSS waters.

Different algorithms were used to estimate chl-a and TSS concentrations from reflectance data. Power regression was found to be the best method for both chl-a and TSS estimation. Finally, the methods developed for in-situ measurements were applied to airborne hyperspectral data, which has the potential to monitor areas at a regional scale. The results showed a close relationship between the results obtained from in-situ measurements and airborne datasets.

In general, this study showed that remote sensing is an efficient method for monitoring the water quality in small, highly turbid aquatic habitats. The study also provided useful algorithms for estimating the concentrations of chl-a and TSS in these water bodies.

The article is attached as appendix 4 of the thesis.

Chapter 4

4 Conclusions

This thesis discusses the historical development of the hyperspectral laboratory at CzechGlobe in three articles. The remaining three articles demonstrate the use of the hyperspectral laboratory by practical examples.

4.1 Summary of thesis

The first part of the thesis presented in chapter 2 describes the development of the hyperspectral laboratory. Apart from the development of hyperspectral laboratory instrumentation, an important aspect described is the pre-processing chain that has evolved in tandem with the lab's instrumentation and its changing performance. The development of quality layers for the outputs of processing chain established at CzechGlobe are also described. Subsequent methods that improve data acquisition and processing are outlined. Some of these methods could be used only for specific data pre-processing chains, such as the fusion of CASI and SASI data for forested areas. Other remote sensing platforms equipped with push broom sensors could utilize some of these methods, for example, planning of data acquisition within 10° around the actual solar principle plane.

Three examples were used to illustrate the utilisation of hyperspectral data within the second part of the thesis. Two of the examples were focused on the forest ecosystem, which could be advantageously monitored using the FLIS airborne laboratory. The

main result of the first study is possibility to determine individual trees infested by bark beetle. Infestations were detected 23 days after the field survey using remote sensing methods, which is still suitable for proactive management. The second forestry study presents a possible method for determining the age of a forest stand based on hyperspectral data. The last example shows how hyperspectral data was used to estimate water quality. The study recommends classifying water bodies into three categories (oligotrophic waters, low chl-a waters, and high chl-a and TSS waters) and use different algorithms to estimate water parameters for each category. More examples of laboratory use can be found in the bibliography.

4.2 Fulfilments of goals

The goals of the thesis were fulfilled. Processing chains for individual sensors were developed and established. Pre-processing chains for VNIR and SWIR sensors were developed and established by the author of this thesis, as well as subsequent processing upgrades. The pre-processing chains established for the FLIS sensors are currently in use and provide data on a daily basis. Within the second part of the thesis, the beneficial use of the hyperspectral laboratory was demonstrated on several examples with the contribution of the author. Within the thesis all developments are documented by means of articles presented to the scientific community.

4.3 Summary of the author contributions

The author dedicated to the field of imaging spectroscopy number of last years and was involved in several national as well as international projects. Short summarisation of achievements follows. Among contributions of the author to the research field of imaging spectroscopy could be counted following items:

- development of ground reference panels for airborne, UAS and ground based image acquisition
- testing of usability of the apparent reflectance methods for Specim as well as Itres hyperspectral sensors
- continuous development and establishing of hyperspectral data pre-processing chains for daily data processing, especially for VNIR and SWIR spectral regions
- establishing of the FLIS

- establishing of radiometric calibration laboratory and radiometric calibration of imaging sensors
- establishing of facility equipped for supportive ground measurements for airborne campaigns
- establishing of joint UAS/laboratory facility (same hyperspectral imaging sensors are used at UAS platform and for scanning in the laboratory)
- characterization of the imaging sensors (e.g. smile effect)
- putting into action several of hyperspectral sensors including rules for further proper operation
- development of quality layers for hyperspectral image data
- improvement of ASD integrating sphere for transmittance measurements
- improvement of holder for Norway Spruce needles for spectral measurements
- processing of datasets acquired by other hyperspectral sensors e.g. HyMap
- co-investigator role in number of international projects (EUFAR, Hyper-I-Net,..)
- co-investigator role in number of national projects (HyDAP, GAČR,..)
- co-investigator role in number of ESA projects (CAIRTEX, HYPER,,..)
- activities within number of ESA campaigns (FlexSense, TomoSense, SurfSense,..)
- Support and development of applications involving hyperspectral data for number of topics (water, soil, archaeology, oil contamination,…)
- Involving of FLIS into international scientific infrastructures (EUFAR, AnaEE)
- Propagation of imaging spectroscopy at national and international conferences

4.4 Further development

To ensure that the hyperspectral laboratory works properly, it's necessary to check the performance of the sensors on a regular basis and eventually develop additional maintenance methods in the case of changed performance. For possible further publication, it seems interesting to elaborate the data acquisition scheme in the solar principal plane (Article 3, Appendix 1). Perform simulations and evaluate possibilities for different surfaces and platforms (UAS, airborne).

Probably most significant improvement for the processing chains would be direct incorporation of the new MODTRAN-6 radiative transfer model. The new model can

be integrated into the processing chain for both the reflective spectral range (VNIR+SWIR) and the thermal spectral range.

For better spatial co-registration of all sensors, it would be useful to develop an automatic determination of boresight angles.

Bibliography

Ač, A., Malenovský, Z., Hanuš, J., Tomášková, I., Urban, O., Marek, M.V., 2009. Near-distance imaging spectroscopy investigating chlorophyll fluorescence and photosynthetic activity of grassland in the daily course. Funct. Plant Biol. 36, 1006. https://doi.org/10.1071/FP09154

Bachmann, M., Adar, S., Ben-Dor, E., Biesemans, J., Briottet, X., Grant, M., Hanus, J., Heuvelink, G., Holzwarth, S., 2011. EUFAR FP7 JRA2 - HYQUAPRO DJ2.2.3 – Quality Layers for USBE, TAU-BarKal and FUB.

Bárta, V., Hanuš, J., 2018. Collecting information for spectral boundaries determination, in: Target and Background Signatures IV. Presented at the Target and Background Signatures IV, SPIE, pp. 9–16. https://doi.org/10.1117/12.2325465

Ben-Dor, E., Schläpfer, D., Plaza, A.J., Malthus, T., 2013. Hyperspectral Remote Sensing, in: Airborne Measurements for Environmental Research. John Wiley & Sons, Ltd, pp. 413–456. https://doi.org/10.1002/9783527653218.ch8

Berk, A., Anderson, G.P., Bernstein, L.S., Acharya, P.K., Dothe, H., Matthew, M.W., Adler-Golden, S.M., Chetwynd, Jr., J.H., Richtsmeier, S.C., Pukall, B., Allred, C.L., Jeong, L.S., Hoke, M.L., 1999. MODTRAN4 radiative transfer modeling for atmospheric correction, in: Larar, A.M. (Ed.), . Presented at the SPIE's International Symposium on Optical Science, Engineering, and Instrumentation, Denver, CO, USA, p. 348. https://doi.org/10.1117/12.366388

Brovkina, O., Novotny, J., Cienciala, E., Zemek, F., Russ, R., 2017. Mapping forest aboveground biomass using airborne hyperspectral and LiDAR data in the mountainous conditions of Central Europe. Ecol. Eng. 100, 219–230. https://doi.org/10.1016/j.ecoleng.2016.12.004

Hanus, J., Fabianek, T., Kaplan, V., Zemek, F., 2013. Airborne imaging spectroscopy at Czechglobe - Potential, data processing and quality indicators. Presented at the International Multidisciplinary Scientific GeoConference Surveying Geology and Mining Ecology Management, SGEM, pp. 557–563. https://doi.org/10.5593/SGEM2013/BB2.V2/S10.002

Hovi, A., Schraik, D., Hanuš, J., Homolová, L., Juola, J., Lang, M., Lukeš, P., Pisek, J., Rautiainen, M., 2022. Assessment of a photon recollision probability based forest reflectance model in European boreal and temperate forests. Remote Sens. Environ. 269, 112804. https://doi.org/10.1016/j.rse.2021.112804

Klem, K., Záhora, J., Zemek, F., Trunda, P., Tůma, I., Novotná, K., Hodaňová, P., Rapantová, B., Hanuš, J., Vavříková, J., Holub, P., 2018. Interactive effects of water deficit and nitrogen nutrition on winter wheat. Remote sensing methods for their detection. Agric. Water Manag. 210, 171–184. https://doi.org/10.1016/j.agwat.2018.08.004

Malenovský, Z., Homolová, L., Zurita-Milla, R., Lukeš, P., Kaplan, V., Hanuš, J., Gastellu-Etchegorry, J.-P., Schaepman, M.E., 2013. Retrieval of spruce leaf chlorophyll content from airborne image data using continuum removal and radiative transfer. Remote Sens. Environ. 131, 85–102. https://doi.org/10.1016/j.rse.2012.12.015

Minařík, R., Langhammer, J., Hanuš, J., 2019. Radiometric and Atmospheric Corrections of Multispectral μMCA Camera for UAV Spectroscopy. Remote Sens. 11, 2428. https://doi.org/10.3390/rs11202428

Mišurec, J., Kopačková, V., Lhotáková, Z., Hanuš, J., Weyermann, J., Entcheva-Campbell, P., Albrechtová, J., 2012. Utilization of hyperspectral image optical indices to assess the Norway spruce forest health status. J. Appl. Remote Sens. 6, 063545–1. https://doi.org/10.1117/1.JRS.6.063545

Novotný, J., Navrátilová, B., Hanuš, J., Brovkina, O., 2023. Hodnocení lesní nadzemní biomasy pomocí dat leteckého laserového skenování. Lesn. Práce 102, 3.

Orság, M., Meitner, J., Fischer, M., Svobodová, E., Kopp, R., Mareš, J., Spurný, P., Pechar, L., Beděrková, I., Hanuš, J., Semerádová, D., Balek, J., Radojičić, M., Hanel, M., Vizina, A., Žalud, Z., Trnka, M., 2023. Estimating Heat Stress Effects on the Sustainability of Traditional Freshwater Pond Fishery Systems under Climate Change. Water 15, 1523. https://doi.org/10.3390/w15081523

Purket, T., Hanuš, J., Fajmon, L., Fabiánek, T., 2019. Improvements in the Processing Chain of Thermal Hyperspectral Data from TASI-600, in: 11th EARSeL SIG Imaging Spectroscopy Workshop 2019. Presented at the 11th EARSeL SIG Imaging Spectroscopy Workshop 2019, EARSeL, Brno.

Schläpfer, D., Richter, R., 2002. Geo-atmospheric processing of airborne imaging spectrometry data. Part 1: Parametric orthorectification. Int. J. Remote Sens. 23, 2609–2630. https://doi.org/10.1080/01431160110115825

Slezák, L., Hanuš, J., Purket, T., 2021. Development of smoothed DSM for improvement of airborne data georectification, in: 40th EARSeL Symposium 2021 European Remote Sensing-New Solutions for Science and Practice. Presented at the 40th EARSeL Symposium 2021 European Remote Sensing-New Solutions for Science and Practice, EARSeL, Warsaw.

Smith, G.M., Milton, E.J., 1999. The use of the empirical line method to calibrate remotely sensed data to reflectance. Int. J. Remote Sens. 20, 2653–2662. https://doi.org/10.1080/014311699211994

Urban, J., Pikl, M., Zemek, F., Novotný, J., 2022. Using Google Street View photographs to assess long-term outdoor thermal perception and thermal comfort in the urban environment during heatwaves. Front. Environ. Sci. 10.

Vane, G., Goetz, A.F.H., Wellman, J.B., 1984. Airborne imaging spectrometer: A new tool for remote sensing. IEEE Trans. Geosci. Remote Sens. GE-22, 546–549. https://doi.org/10.1109/TGRS.1984.6499168

Vinciková, H., Pechar, L., Hanuš, J., 2013. Meření a využití spektrální odrazivosti (reflektance) slunečního záření z hladiny povrchových vod. Certifikovaná Metod.

Appendix 1

Article 1

Technical Note

Flying Laboratory of Imaging Systems: Fusion of Airborne Hyperspectral and Laser Scanning for Ecosystem Research

Jan Hanuš [1,2,*], Lukáš Slezák [1,3], Tomáš Fabiánek [1], Lukáš Fajmon [1], Tomáš Hanousek [1,3], Růžena Janoutová [1], Daniel Kopkáně [1], Jan Novotný [1], Karel Pavelka [2], Miroslav Pikl [1], František Zemek [1,4] and Lucie Homolová [1]

1 Global Change Research Institute of the Czech Academy of Sciences (CzechGlobe), Bělidla 986/4a, 603 00 Brno, Czech Republic
2 Department of Geomatics, Faculty of Civil Engineering, Czech Technical University in Prague, Thákurova 7, 166 29 Prague 6, Czech Republic
3 Department of Geography, Faculty of Science, Masaryk University, Kotlářská 2, 611 37 Brno, Czech Republic
4 Faculty of Agriculture and Technology, University of South Bohemia in České Budějovice, Studentská 1668, 370 05 České Budějovice, Czech Republic
* Correspondence: hanus.j@czechglobe.cz

Abstract: Synergies of optical, thermal and laser scanning remotely sensed data provide valuable information to study the structure and functioning of terrestrial ecosystems. One of the few fully operational airborne multi-sensor platforms for ecosystem research in Europe is the Flying Laboratory of Imaging Systems (FLIS), operated by the Global Change Research Institute of the Czech Academy of Sciences. The system consists of three commercial imaging spectroradiometers. One spectroradiometer covers the visible and near-infrared, and the other covers the shortwave infrared part of the electromagnetic spectrum. These two provide full spectral data between 380–2450 nm, mainly for the assessment of biochemical properties of vegetation, soil and water. The third spectroradiometer covers the thermal long-wave infrared part of the electromagnetic spectrum and allows for mapping of surface emissivity and temperature properties. The fourth instrument onboard is the full waveform laser scanning system, which provides data on landscape orography and 3D structure. Here, we describe the FLIS design, data acquisition plan and primary data pre-processing. The synchronous acquisition of multiple data sources provides a complex analytical and data framework for the assessment of vegetation ecosystems (such as plant species composition, plant functional traits, biomass and carbon stocks), as well as for studying the role of greenery or blue-green infrastructure on the thermal behaviour of urban systems. In addition, the FLIS airborne infrastructure supports calibration and validation activities for existing and upcoming satellite missions (e.g., FLEX, PRISMA).

Keywords: remote sensing; hyperspectral; imaging spectroscopy; thermal; laser scanning; LiDAR; reflectance; surface temperature; ecosystem assessment

1. Introduction

The role of remote sensing in ecological research has increased in importance in recent decades as it has become an irreplaceable source of information on ecosystem status and change [1–3]. Ecological research tends to become increasingly complex in order to understand the interactions of organisms, including humans, with the environment at different scales [4–6]. To answer such complex questions, synergies of multi-source, multi-temporal and multi-scale observations are needed, and remote sensing technology can provide such data [7–11].

On the one hand, there are satellite data with regular acquisitions, typically with global coverage and spatial resolution varying between 10 m and 1 km (e.g., Landsat, Copernicus Sentinels). Regular satellite-based observations have improved our ability to detect global trends and changes in forest cover [12], shifts in vegetation phenology [13], declines in land

evapotranspiration [14], etc., but are less suitable for studying local phenomena. Recently, the availability of hyperspectral satellite data has increased thanks to the PRISMA [15] and EnMAP [16] missions, and there are also emerging constellations of small satellites providing data with very high spatial resolution [17]. On the other hand, there is a boom in unmanned aerial systems (UAS) used for ecosystem research [18–23]. The UAS systems compete with remote sensing from aircraft platforms, the most traditional form of remote sensing, due to their higher operability and lower acquisition costs. The niche for airborne remote sensing is therefore becoming smaller.

However, airborne remote sensing data provide an intermediate-scale link between large-scale satellite and point-scale field observations [24]. They are essential for the calibration and validation of satellite products [25], the simulation of future satellite data [26], flexible to address specific research needs for testing and developing methods at the local scale [27,28], and provide greater flexibility for integration with field campaigns [29]. In addition, it is a stable platform that can accommodate multiple sensors simultaneously (multi- or hyperspectral scanners, lasers, thermal scanners and radars) and operate them under the same illumination conditions. Multi-sensor airborne data increase our ability to retrieve structural and functional properties of different landscape elements in high spatial detail [9]. Airborne data also play an indispensable role in the study of urban ecosystems [30,31]. High spatial/spectral resolution in reflectance and thermal, together with detailed digital terrain and surface models derived from dense laser point clouds, provide a data portfolio for assessing relationships between 3D urban structures, properties of urban elements and thermal performance. Such detailed information is very important for urban planners and cannot currently be obtained either from satellite (very low spatial resolution in the thermal domain) or UAS (legal obstacles in populated areas).

The concept of an airborne multi-sensor platform is not new. To our knowledge, there are currently two systems in operation in the United States and three in Europe. In the United States, these are the Carnegie Airborne Observatory (CAO) and its next-generation CAO-2 Airborne Taxonomic Mapping System [32,33] that is used within the National Ecological Observatory Network's Airborne Observation Platform (NEON AOP; [34]) and NASA's Goddard's LiDAR, Hyperspectral and Thermal (G-LiHT) airborne imager [35]. In Europe, it is the Swiss Airborne Research Facility ARES [36], the NERC Airborne Research and Survey Facility in the United Kingdom [37] and the Flying Laboratory of Imaging Systems FLIS [38,39] operated by the Global Change Research Institute of the Czech Academy of Sciences (CzechGlobe). The main goal of this contribution is to describe the FLIS research infrastructure and provide details on data pre-processing and fusion.

2. System Design and Instruments

The scientific objective of FLIS is to provide an operational infrastructure for high-quality remote sensing data combining hyperspectral, thermal and laser scanning from a single platform to support complex and long-term ecosystem research at spatial scales corresponding with processes and fluxes of energy and matter within and between ecosystems.

FLIS consists of four main instruments and their associated control and computing systems installed in a photogrammetric aircraft (Figure 1). The aircraft is Cessna 208 B Grand Caravan, which was modified to acquire data through two custom-made hatches. The instruments onboard are three commercial imaging spectroradiometers (or hyperspectral scanners) produced by the Canadian company ITRES Research Limited. These are CASI-1500 (Compact Airborne Spectrographic Imager), which captures data in the visible and near-infrared (VNIR) region between 380 and 1050 nm, and SASI-600 (SWIR Airborne Spectrographic Imager), which captures data in the shortwave infrared (SWIR) region between 950 and 2450 nm. These two sensors are mounted on a gyro-stabilised platform in the front hatch and together provide full spectral data between 380 and 2450 nm. Their main application is the assessment of vegetation biochemical, soil and water chemical properties. The third imaging spectroradiometer, TASI-600 (Thermal Airborne Spectrographic Imager), captures data in the long-wave infrared (LWIR) thermal region between 8000 and

11,500 nm. It allows for the mapping of surface emissivity and temperature properties. The three imaging spectroradiometers (hereafter referred to as CASI, SASI and TASI) are push-broom sensors that scan an area of interest in individual rows using the aircraft's forward motion. The basic technical specifications of the FLIS hyperspectral scanners are summarised in Table 1.

(a)

(b)

Figure 1. (**a**) Cessna 208 B Grand Caravan airborne carrier and (**b**) the instruments onboard (from right to left: LSM Q780 laser scanner, TASI-600, CASI-1500 and SASI-600 on a gyro-stabilised platform, a rack with acquisition computers).

Table 1. Basic technical specifications of the FLIS hyperspectral instruments.

	CASI-1500	SASI-600	TASI-600
Spectral domain	VNIR	SWIR	LWIR
Spectral range [nm]	380–1050	950–2450	8000–11,500
Max. spectral resolution [nm]	2.7	15	110
Max. number of spectral bands	288	100	32
Across-track spatial pixels	1500	600	600
Field of view [°]	40	40	40
Instantaneous field of view [mrad]	0.49	1.2	1.2
Typical spatial resolution [1] [m]	0.5–2.0	1.25–5.0	1.25–5.0

[1] The minimum spatial resolution corresponds to the flight altitude of about 1000 m above ground level (AGL), while the maximum corresponds to 4000 m AGL.

The fourth instrument onboard is the LMS Q780 full waveform laser scanning system (or LiDAR, abbreviated from Light Detection and Ranging), manufactured by RIEGL Laser Measurement Systems GmbH [40]. It provides data on landscape orography and the 3D structure of vegetation and non-vegetation surfaces. The laser scanner uses a polygon rotating mirror to produce straight parallel scan lines and equally dense laser footprint patterns on the ground. The basic technical specifications of the laser scanner are summarised in Table 2. The laser scanner is mounted with TASI in the rear hatch. Thanks to its wide field of view of 60°, the area of interest is typically covered with double point density, as the flight plan is often optimised for hyperspectral sensors with a narrower field of view of 40°.

Table 2. Basic technical specifications of the FLIS airborne laser scanner LMS Q780.

	LMS Q780
Laser pulse repetition rate [kHz]	Up to 400
Maximum measuring range [m]	Up to 5800 [1]
Wavelength [nm]	1064
Laser beam divergence [mrad]	≤ 0.25
Field of view [°]	60
Typical point density [pts/m^2]	0.5–4 [2]

[1] For targets with 60% reflectivity, for targets with 20% reflectivity the maximum range is 4100 m. The maximum range is also dependent on atmospheric conditions. [2] The minimum point density of 0.5 pts/m^2 corresponds to the flight altitude of 4000 m AGL, and the maximum of 4 pts/m^2 to 1000 AGL. Due to flight line overlap, point densities are usually between 1 and 8 pts/m^2.

The aircraft is equipped with other devices and systems (such as a navigation system, a gyro-stabilised platform, etc.) to improve the quality of the hyperspectral and laser data and to acquire auxiliary data for the final processing. The current altitude and position of the aircraft and sensors are monitored using GNSS/IMU inertial navigation units. The POS AV 410 system monitors CASI and SASI, while the AP60 system monitors TASI and the laser scanner. The data acquired by the hyperspectral sensors are synchronised with the signal from the GNSS/IMU units and recorded in the acquisition computers.

The installation of the instruments in the aircraft (Figure 1) can also be viewed on a 3D image available at [41]. The total payload, including the instruments and their accessories, has a mass of about 360 kg. More technical details about FLIS and example datasets can be found at [38].

In addition to the four primary sensors, the aircraft is certified to carry the HyPlant instrument [42,43], an airborne demonstrator for the upcoming ESA FLuorescene EXplorer satellite mission FLEX. FLEX will map global photosynthetic activity through sun-induced fluorescence measurements from space and is expected to be launched in 2025 [44]. The PTR-TOF 6000 instrument [45] for measurements of volatile organic compounds is also certified for onboard installation.

3. Flight Planning and Data Acquisition

Flight planning is an essential part of successful data acquisition. Creating a single optimal acquisition plan for all sensors is challenging. Each sensor requires specific planning to achieve its optimal performance [46], e.g., (i) flight altitude affects the spatial resolution and laser point density; (ii) VNIR and SWIR data are least affected by Bidirectional Reflectance Distribution Function (BRDF) effects when flying in the solar principle plane direction; (iii) thermal data are optimal to acquire as quickly as possible to avoid significant changes in surface temperature within an area of interest; (iv) laser scanner acquisition direction is optimal to plan according to topography. It is, therefore, necessary to properly evaluate all requirements related to a data acquisition task, sensors' specifications, and flight cost efficiency.

The area of interest is very often covered by multiple flight lines. A multi-line VNIR/SWIR image mosaic suffers from inconsistent reflectance values at the overlay between the flight lines. This inconsistency is caused by surface reflectance properties that vary with different sun illumination and observation angles, as described by the BRDF. In most cases, users prefer a "seamless" mosaic where the same surface is characterised by the same reflectance. The BRDF effect in the across track direction, caused by the relatively wide field of view of the airborne hyperspectral sensors, can be effectively suppressed on hyperspectral images by appropriate flight geometry without the need for subsequent corrections such as nadir normalisation, across track illumination correction, or the BREFCOR algorithm [47]. To minimise the BRDF effect, the flight plan is realised in the actual solar principal plane direction. To support and demonstrate this, simulations of the anisotropic reflectance behaviour of vegetation were performed for a virtual 3D forest stand (see Appendix A). To minimise the BRDF effect in an area of interest, we generate 12

flight plans with an azimuth in steps of 15°. During data acquisition, an operator selects the flight plan closest to the actual solar principal plane direction (between −7.5° and +7.5°). This enables the acquisition of hyperspectral image data (across-track scanning with a push-broom sensor) perpendicular to the solar principal plane with a maximum deviation of 10°. It is necessary to use a gyro-stabilised platform to correct for the non-zero yaw angle caused by an eventual side wind, which results in deviations from the solar principal plane, to ensure proper performance. This approach is particularly useful for sites that could be imaged within a time range when the sun's azimuth changes from the selected flight plan azimuth by a maximum of ±10°. Sites with "seamless" mosaics, generated without the need for additional BRDF corrections, can be used, for instance, as calibration surfaces for satellite data or time-series analysis.

4. Data Pre-Processing and Products

The FLIS data pre-processing chain (Figure 2) is divided into three branches: (i) for CASI and SASI sensors, which scan the reflected solar radiation in the VNIR-SWIR domain; (ii) for TASI, which scans the emitted thermal radiation in the LWIR domain; and (iii) for the laser scanner. The pre-processing data chains are described separately, while the boresight alignment is common to all sensors.
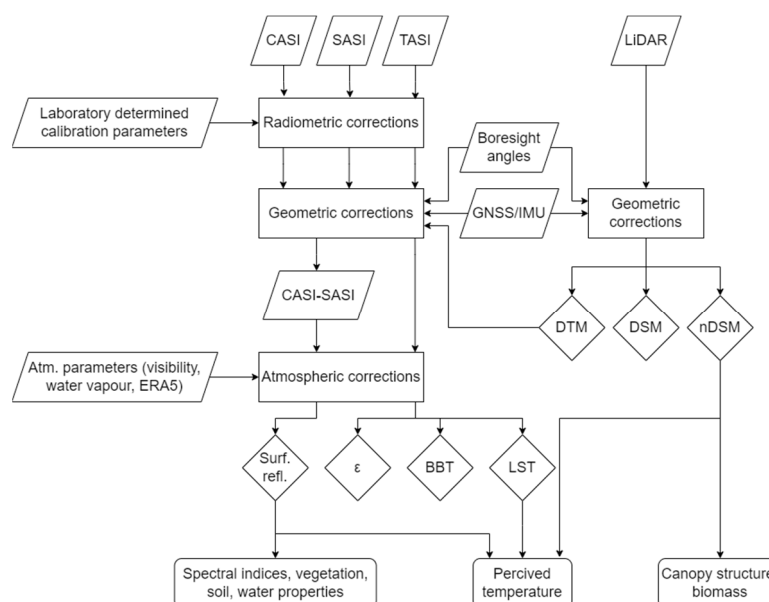

Figure 2. Flow chart of the Flying Laboratory of Imaging Systems (FLIS) data pre-processing chains for CASI, SASI, and TASI imaging spectroscopy data and for laser scanning (LiDAR) data. Abbreviations: GNSS—Global Navigation Satellite System; IMU—Inertial Measurement Unit; DTM—Digital Terrain Model; DSM—Digital Surface Model; nDSM—normalised DSM; Surf. refl.—Surface reflectance; ε—Emissivity; BBT—Broadband Brightness Temperature; LST—Land Surface Temperature.

4.1. Boresight Alignment

The alignment of the IMU/GNSS coordinate system and the coordinate systems of the sensors (boresight angles) is calculated at least once per season and every time the sensors are installed in the aircraft. The boresight angles are computed from data acquired over a calibration site selected in the Brno district Modřice near the Brno-Tuřany Airport (the FLIS home base). This calibration site was chosen because of the large number of small perpendicular streets with gardens and houses with double-pitched roofs, which provide good ground control points for the hyperspectral sensors and the laser scanner (Figure 3). Around 400 ground control points were measured there by a geodetical GNSS system, and about 70 control planes (pitched roofs) were geodetically measured to help with laser

scanner calibration. Two boresight flights are always carried out, one optimised for the hyperspectral sensors and the second optimised for the laser scanner.
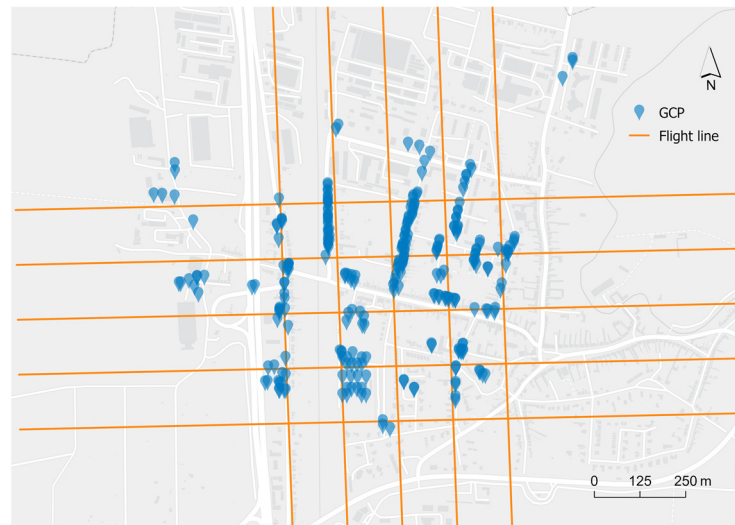

Figure 3. Overview of the boresight calibration site in Brno district Modřice (49.1289N, 16.6094E) with about 400 ground control points (GCP) and a calibration flight plan for hyperspectral sensors.

4.2. CASI and SASI Data

4.2.1. Radiometric Corrections

All hyperspectral sensors are under the ITRES maintenance programme and are regularly serviced and calibrated. Radiometric and spectral calibrations are performed every year by the sensor producer. Radiometric calibration parameters are determined for each pixel of the sensor matrix in a laboratory (Figure 4). The basic radiometric correction procedure for CASI and SASI data consists of subtracting dark current and converting raw values in digital numbers scanned by the sensor into physically defined radiance units. Radiometric corrections are performed using the RadCorr 12.1.3.0 software [48]. The values of the final image data are given in radiometric units [$\mu W \cdot cm^{-2} \cdot sr^{-1} \cdot nm^{-1}$] multiplied by a scaling factor of 1000 to make better use of the unsigned integer range.
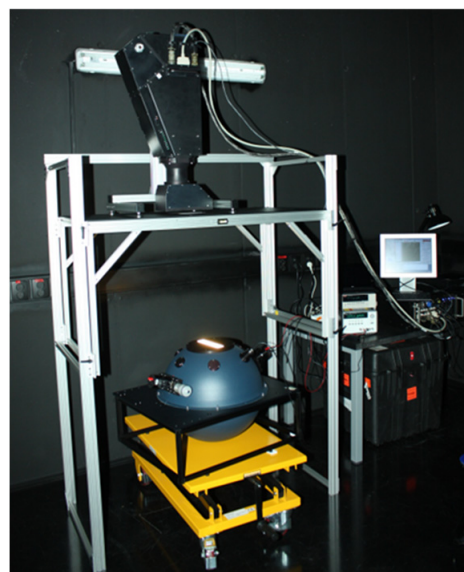
Figure 4. Laboratory determination of radiometric calibration coefficients for the SASI-600 sensor using the LabSphere CSTM-LR-20-M-C integrating sphere at the CzechGlobe calibration premises.

Additional corrections can be applied to CASI and SASI hyperspectral data during the radiometric corrections to compensate for various negative artefacts in the data. For CASI data, the accuracy of the applied spectral correction is checked during the radiometric correction using a spectral calibration file produced on the fly by a built-in calibration source. Each CASI flight line is accompanied by a spectral calibration file measured before image data acquisition. The scattered light correction is particularly important for CASI, as it removes light scattered in the optical sensor system and is performed on individual rows using defined detector columns that do not receive the image signal. Frameshift smear correction addresses the added signal during data readout in the CCD detector. Second-order light correction adjusts the effect of the diffraction grating on the broad spectral range of the CASI sensor, which causes artificial amplification of the signal at specific wavelengths. This effect is corrected using a model based on laboratory experiments with the given sensor. Finally, residual correction, which uses homogenised uniformity data measured at the beginning and end of each flight line, can address random effects that influence individual pixels that cannot be removed during standard processing, such as dust particles on the detector.

For SASI data, additional spectral verification and corrections are based on atmospheric features. Correction of bad pixels is particularly important for SASI and TASI, which are equipped with mercury cadmium telluride detectors. This correction involves detecting and replacing the values of defective pixels with the interpolated values from the surrounding area in spatial or spectral dimensions. The total number of bad pixels is less than 1% of the total array for both sensors. The CASI sensor with the CCD detector has remained free from defective pixels, with only a few instances of bad pixels occurring since 2022 (less than 0.05%).

4.2.2. Georeferencing

Georeferencing, which includes geometric correction and orthorectification, is performed in a single step through parametric geocoding using auxiliary data logged by the POS AV 410 GNSS/IMU unit and a digital terrain model in the GeoCor 5.10.17.1 software [48]. The standard approach involves using a digital terrain model. For campaigns that target forest ecosystems, a digital surface model derived from the laser point cloud data is used to improve georeferencing accuracy. For the resampling of data to the coordinate system (ETRS-89, UTM), the nearest neighbour method is used to prevent spatial interpolation resulting in unrealistic spectral signatures [49,50]. If a mosaic is created, the min. nadir method is typically used, placing a pixel closer to the nadir from two overlapping lines into the mosaic. This mosaicking method reliably eliminates marginal pixels that are more affected by the BRDF effect.

### 4.2.3. Fusion of CASI and SASI Data

To fully utilise the VNIR-SWIR range for some spectral analysis, it is advantageous to aggregate CASI and SASI data into a single hyperspectral data cube. Due to different spatial resolutions, slightly different viewing angles (sensor models), and potential inaccuracies in georeferencing between CASI and SASI, there are discontinuities in a spectral profile at the VNIR-SWIR boundary [51,52]. Spectral discontinuities mainly occur on highly heterogeneous surfaces, such as forests with changes between sunlit and shaded pixels and urban areas with many spectrally different surfaces. For these ecosystems, it is not possible to use a simple pixel aggregate method to merge CASI and SASI hyperspectral cubes, which, on the other hand, works well for spectrally homogeneous surfaces such as meadows and crop fields. Therefore, we developed our own CASI-SASI Fuse (CSF) method optimised for forest areas.

The CSF method compares the overlapping spectral regions of CASI and SASI data. Input data to CSF are georeferenced and radiometrically corrected CASI and SASI hyperspectral cubes. In the first step, CASI data are spectrally resampled to the SASI spectral resolution and positions of the central wavelength using a third-order Butterworth filter. In

the second step, the CASI data are resampled to match the SASI spatial resolution using the pixel aggregate method with a kernel size of 2.5 × 2.5 original CASI pixels. Pixel aggregation is calculated for 64 virtual positions, as illustrated in Figure 5. The original SASI pixel radiance is compared with the 49 variants of the averaged CASI radiance at the wavelength of 1004 nm (Figure 6). The virtual position with an average CASI radiance value that best matches the SASI radiance at 1004 nm is selected as the final position. Once the final spatial position of the CASI pixels for aggregation is determined, the original spectral resolution of the CASI data is used to compute the average radiance values, allowing the spatially resampled CASI data to maintain their original spectral resolution.

The CSF method is currently not optimised for urban systems with many small and spectrally different surfaces. For urban studies, the CASI and SASI datasets are analysed separately.
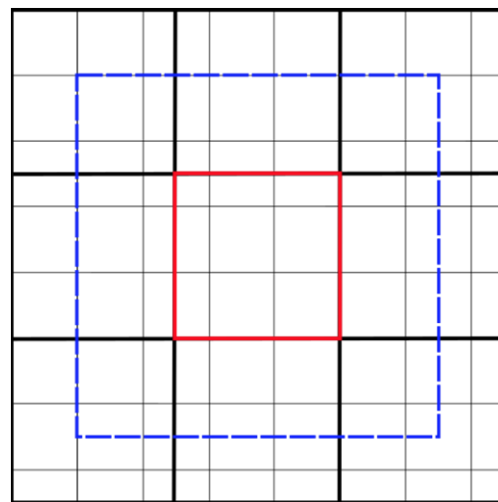
Figure 5. Schematic representation of the CASI-SASI Fuse (CSF) method. Thick black lines represent SASI pixels, and thin black lines represent CASI pixels. The CSF method creates 49 virtual positions of aggregated CASI pixels in SASI spatial resolution within the blue rectangle (the red kernel moves within the blue rectangle in steps of 0.5 CASI pixels). The final kernel position for CASI resampling is the minimum difference between the average CASI and SASI radiance values at 1004 nm.
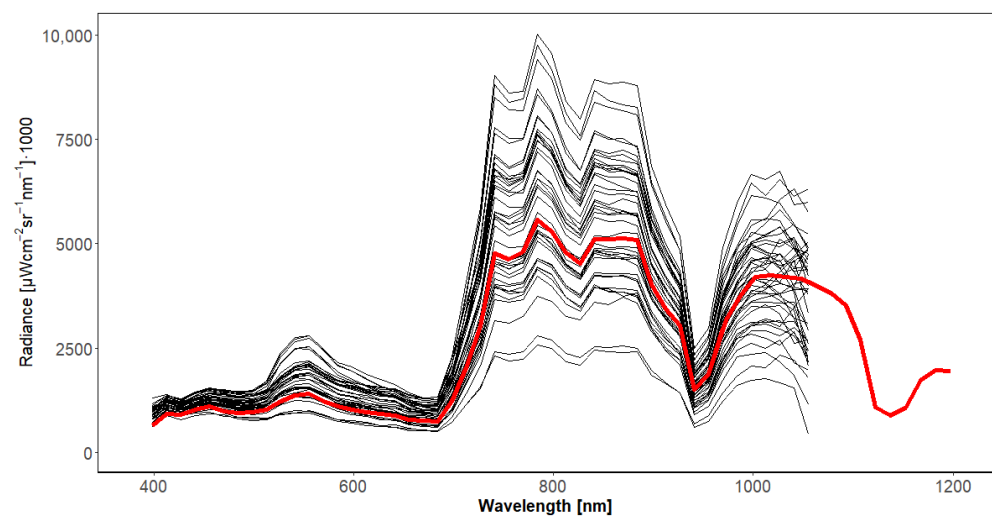

Figure 6. Example of the spectral radiance profile of a CASI-SASI fused pixel (red line) over a forested area. The black lines show a radiance variation of nine CASI pixels within one SASI pixel that would be used for a simple spatial pixel aggregation.

4.2.4. Atmospheric Correction

Atmospheric corrections are based on a radiative transfer model that allows for the calculation of surface reflectance from at-sensor radiance without prior knowledge of surface reflectance properties. This calculation is divided into two parts: the estimation of atmospheric parameters and the calculation of surface reflectance. Key atmospheric parameters include the type and quantity of aerosols (aerosol optical thickness) and water vapour content, which significantly affect the passage of radiation through the atmosphere and can vary with time. These parameters can be measured using a sunphotometer during a ground support campaign or estimated directly from the image data.

Atmospheric corrections of CASI and SASI data are performed in the ATCOR-4 software package ver. 7.4.0 [47] using the MODTRAN4 radiative transfer model of the atmosphere [53,54]. Both path and adjacency radiances are corrected during the atmospheric corrections, and the resulting reflectance is calculated from the reflected radiance. The corrected data are expressed in reflectance values at the surface level (hemispherical-conical reflectance factor) multiplied by a constant of 100 to make better use of the unsigned integer range (a value of 1000 means a reflectance of 10%). An example of fully corrected CASI and CASI-SASI fused data is shown in Figure 7a,c.

(**a**)　　　　　　　　　(**b**)

(**c**)　　　　　　　　　(**d**)
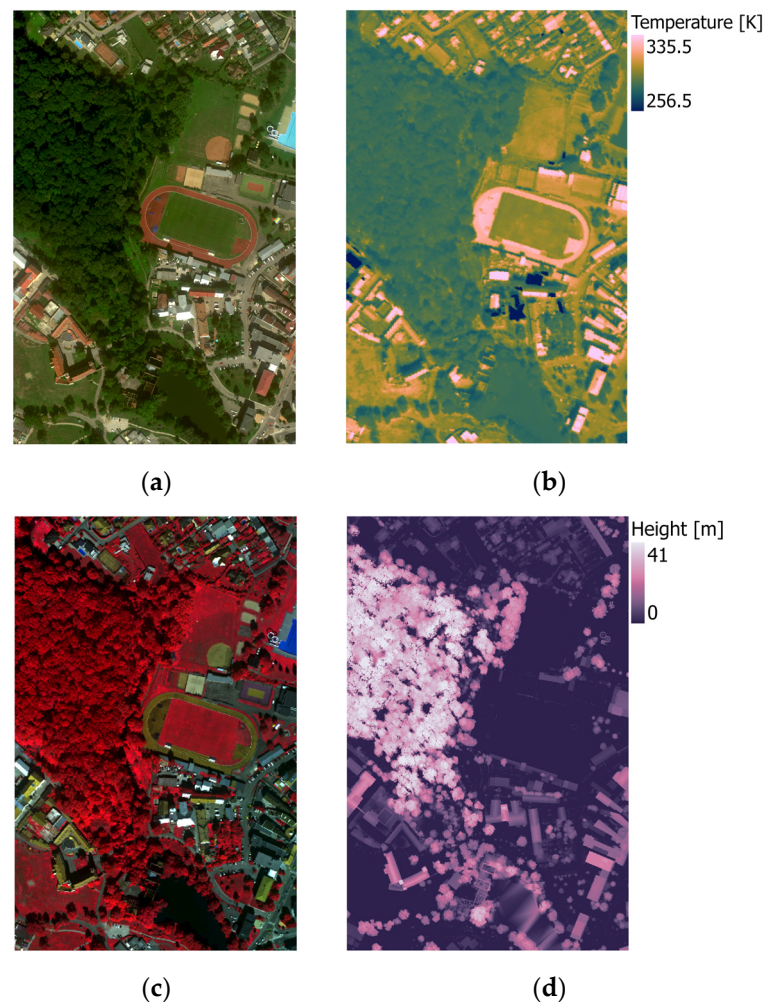
Figure 7. Example of the Flying Laboratory of Imaging Systems (FLIS) final products: (**a**) VNIR hyperspectral data obtained from CASI (displayed as the true-colour composite, pixel size of 0.5 m); (**b**) land surface temperature obtained from TASI (pixel size of 1.25 m); (**c**) VNIR-SWIR hyperspectral data obtained by the fusion of CASI and SASI data (displayed as the false-colour composite R—725 nm, G—652 nm, B—552 nm, pixel size of 1.25 m); and (**d**) normalised digital surface model obtained from the laser scanner (pixel size of 0.5 m).

Corrections for the BRDF effect caused by topography are necessary for data acquired over hilly terrain [47]. High-priority flight campaigns are usually accompanied by ground support measurements for verification/calibration purposes, including measurements of aerosol optical thickness, spectral measurements of ground reference targets, etc. [55]. Spectral reflectance field measurements could be used for vicarious calibration [56], which recalibrates the radiometric correction coefficients to the actual flight conditions, thus improving the atmospheric corrections performed within the ATCOR-4 software package.

4.3. TASI Data

4.3.1. Thermal Radiometric Corrections

The TASI sensor has a dual black body calibration system for onboard radiometric calibration. The first black body keeps an ambient temperature, while the second black body is heated to about 20 °C higher than the first black body. The onboard auxiliary radiometric calibration data are used for radiometric corrections performed in the RadCorr software [48]. There are two basic approaches to radiometric calibration. The first uses laboratory-determined calibration parameters when the onboard calibration data are obtained from a single black calibration body during the flight. The second approach, the dual black body method, uses calibration coefficients specific to each flight line using the data from two calibration black bodies scanned during the flight.

In most cases, the dual black body method is used. Data from the heated black body are also used for spectral verification or calibration of acquired TASI data. The accuracy of the spectral shift determined by the heated black body is significantly improved compared to the ambient black body data.

The values of the final image data are given in radiometric units [$\mu W \cdot cm^{-2} \cdot sr^{-1} \cdot nm^{-1}$] multiplied by a scaling factor of 1000 to make better use of the unsigned integer range.

In addition to the ITRES-recommended procedure to interpolate bad pixels in TASI, a two-step correction is applied to remove noise. In the first step, stripe noise is corrected in the spectral domain. In the second step, stochastic noise in the data is removed by spatial interpolation [57].

4.3.2. Thermal Atmospheric Corrections

The removal of atmospheric effects from the thermal hyperspectral data is essential for the correct retrieval of surface temperature and spectral emissivity. Radiometric calibrations deliver image data containing radiation from the surface attenuated by the atmosphere plus radiation from the atmosphere along the line of sight. Thus, the measured radiance at the sensor level (L) is expressed by the following radiative transfer equation:

$$L = \tau \varepsilon \, B(T) + \tau (1 - \varepsilon) \, L_{\downarrow atm} + L_{\uparrow atm} \tag{1}$$

where τ is the atmospheric transmittance, ε is the surface's emissivity, $B(T)$ is the radiance of the surface at temperature T according to Planck's law, $L_{\downarrow atm}$ is the down-welling atmospheric radiance reflected by the surface ($1 - \varepsilon$), and $L_{\uparrow atm}$ is the atmospheric up-welling radiance. All elements in the equation are wavelength dependent.

In our pre-processing chain, the quantities $L_{\downarrow atm}$, $L_{\uparrow atm}$ and τ are modelled using the MODTRAN 5.3 radiative transfer model, which is parameterised using data from the ERA5 atmospheric near-real-time reanalysis provided by ECMWF [58]. ERA5 provides hourly estimates of a large number of atmospheric, land and oceanic climate variables on a 0.25° grid [59]. ERA5 data are spatially and temporally interpolated for each TASI flight line. Compensating for atmospheric transmittance and up-welling atmospheric radiance leads to land-leaving radiance:

$$L_{LL} = \varepsilon \, B(T) + (1 - \varepsilon) \, L_{\downarrow atm} \tag{2}$$

L_{LL} is the sum of the radiance emitted by the surface and the reflected radiance. Taking into account the down-welling atmospheric radiation $L_{\downarrow atm}$ is not possible without knowing the surface's emissivity. Eliminating the influence of down-welling atmospheric radiance is

part of the calculation of temperature *T* (kinetic) and emissivity *ε* of the surface, which is performed by the Temperature and Emissivity Separation algorithm (TES).

TES was developed by Gillespie et al. (1998) [60] and evaluated in several studies [61–64], and it is used to resolve the indeterminacy of surface temperature and emissivity [65]. It relies on the assumption that any natural surface emissivity spectrum includes a value close to unity within the LWIR spectral range [66]. TES consists of three modules: the Normalization Emissivity Module [60], the Ratio Component and the Maximum-Minimum Difference Module [67]. In our TASI pre-processing chain, the Normalization Emissivity Module has been improved by smoothing spectral radiance signatures [68]. The Maximum-Minimum Difference module estimates real emissivity and temperature based on a semi-empirical relationship between emissivity contrast and minimum spectral emissivity for common materials [69]. It is meaningful to set its parameters according to the target area [70], so it can be tuned for agriculture, urban or forest areas of interest. To improve the TES's accuracy, the noisiest bands can be excluded so that the final product has 22 bands. Typically, spectral bands 1–5 are removed due to noise induced by water vapour and bands 28–32 due to lower radiometric sensitivity.

The resulting images after the TASI atmospheric corrections are as follows:

- Land surface temperature (kinetic temperature) [K] (Figure 7b);
- Land surface emissivity [-];
- Land leaving radiance [W m^{-2} sr^{-1} m^{-1}];
- Broadband brightness temperature for emissivity = 1 [K].

4.4. Laser Scanning Data

The pre-processing of the laser scanning data consists of several steps, which are executed using software tools provided by the laser scanner manufacturer, RIEGL Laser Measurement System GmbH. In the first step, the flight trajectory recorded by AP60 IMU/GNSS unit at a frequency of 200 Hz is calculated. Up until the 2020 flight season (included), data from the POS AV 410 INU/GNSS unit were used. This step is executed in the POSPac MMS 8.7 software. In the second step, points are extracted from the acquired full waveform data using RiUNITE 1.0.3. software. RiUNITE also combines data acquired by the scanner and IMU/GNSS unit. The final point cloud is exported into LAZ 1.4 format using the RiPROCESS 1.9.2 software. Data are exported in the ETRS-89 (UTM) coordinate system. The point cloud also includes Riegl extra bytes, which provide important information from full waveform analysis, such as amplitude and pulse width for each point. The final products derived from the point cloud data are the digital terrain model, digital surface model and normalised digital surface model (Figure 7d), which are calculated using the LasTools 20221102 software package.

5. Conclusions

We have established a fully operational airborne research infrastructure for multi-sensor observations to support complex ecological research. Our Flying Laboratory of Imaging Systems (FLIS) allows the simultaneous acquisition of VNIR-SWIR hyperspectral (CASI-1500 and SASI-600), LWIR thermal (TASI-600) and laser scanning (Riegl LMS Q780) data. The aircraft is also certified for HyPlant—the airborne demonstrator of the future FLEX satellite—and PTR-TOF 6000 for volatile organic compound measurements. FLIS data pre-processing is largely based on software tools provided by sensor manufacturers. Improvements and developments have been made in the pre-processing of TASI hyperspectral data and the fusion of CASI and SASI hyperspectral data cubes, mainly over heterogeneous forested areas. The pre-processing chain is currently well established, and further improvements will focus mainly on the better geometric fusion of sensor data and the timely delivery of final products to users.

FLIS operates in the European research space and is part of the EUFAR (European Facility for Airborne Research) association. Currently, the FLIS data are not openly distributed, but most of the acquisitions in the Czech Republic can be viewed at [71] and can

be shared upon request for research purposes. The FLIS research infrastructure can be accessed either via EUFAR [72] or via open access to CzechGlobe's research facilities [73].

The niche for aircraft-based remote sensing is getting narrower due to the recent expansion of unmanned aerial systems and the increasing availability of various satellite data. However, high-fidelity multi-sensor data from airborne platforms are still valuable. Airborne research platforms such as FLIS help to explore data synergies, develop new methods for ecosystem research, provide an intermediate link in an up-scaling scheme between field and satellite data and, finally, support calibration/validation activities of satellite missions. Airborne platforms are still the only platforms that simultaneously operate optical, thermal, radar, laser and other sensors under the same illumination conditions and provide data at a very high spatial resolution, which will not be achieved from space in the near future.

Author Contributions: Conceptualization, J.H., L.H. and L.S.; modelling, R.J. and D.K.; data visualisation, L.S., R.J. and J.H.; data curation, D.K., J.N., T.F., L.F., T.H., M.P., F.Z., K.P. and J.H.; writing—original draft preparation, J.H. and L.S. All authors made significant contributions to the review and editing of the draft. All authors have read and agreed to the published version of the manuscript.

Data Availability Statement: Data are available upon request.

Conflicts of Interest: The authors declare no conflict of interest. The funders had no role in the development of the manuscript.

Appendix A

The anisotropic reflectance behaviour of vegetation was simulated for a virtual 3D spruce forest stand using the Discreet Anisotropic Radiative Transfer (DART) model version v1096 [74,75]. These simulations support and demonstrate how to minimise the BRDF effect when the flight plan is implemented in the actual solar principal plane. The virtual forest scene consists of 25 trees, each 15 m tall (Figure A1), with a tree LAI of 12 $m^2 \cdot m^{-2}$, reconstructed from terrestrial laser scanning data as described by Janoutová et al. (2021) [76]. The optical properties of the individual objects in the scene were set according to the field measurements described in Homolová et al. (2017) [77]. The size of the simulated scene was 10 × 10 m with a spatial resolution of 0.5 m; the sun's zenith angle was 45° and the sun's azimuth was 150°. Figure A2 shows the anisotropic behaviour of forest reflectance as a function of viewing geometry. Significant differences in reflectance as the viewing geometry changes can be seen in the solar principal plane. In contrast, minimal changes in reflectance occur in the direction perpendicular to the solar principal plane. The above-mentioned results can be advantageously applied to hyperspectral push-broom scanners that scan data in single lines. The only significant change in view angle is in the direction of the across-track. The most balanced reflectance values are therefore obtained when the flight plan is adjusted to the current position of the sun and the azimuth of the flight lines is very close to the current sun azimuth (i.e., the scan lines are perpendicular to the solar principal plane). Figure A3 shows how much a flight plan direction can deviate from the actual solar principal plane (sun azimuth). The lower graphs in Figure A3 show the minimal change in reflectance within the field of view of the FLIS hyperspectral sensors (from −20° to +20°) for planes oriented in a direction perpendicular to the solar principal plane or planes deviating up to 10°.
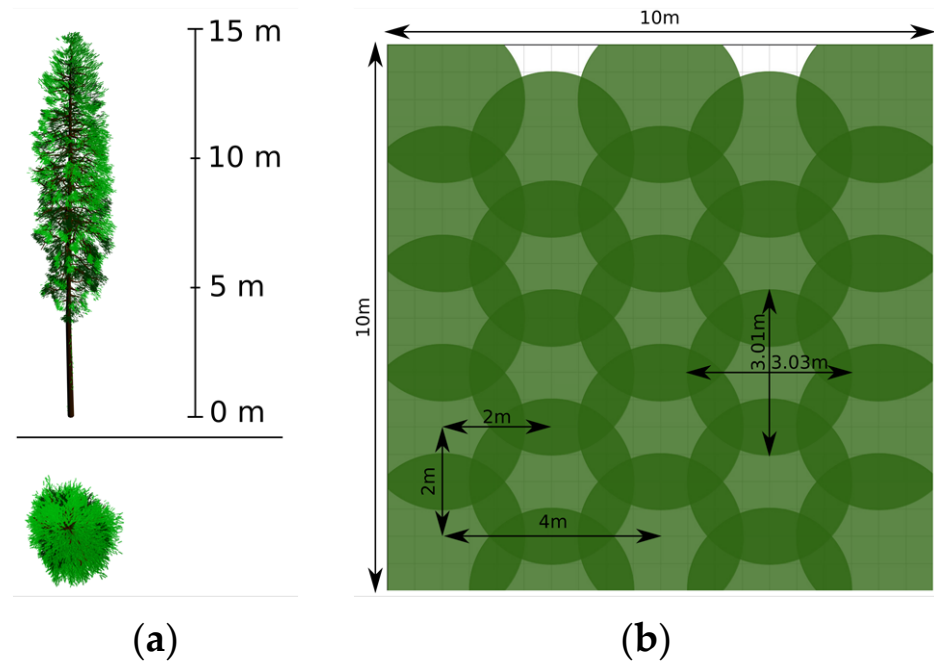
Figure A1. (**a**) 3D representation of the single spruce tree (side and nadir views); (**b**) schematic representation of the virtual forest scene used for radiative transfer simulations in the Discrete Anisotropic Radiative Transfer (DART) model.
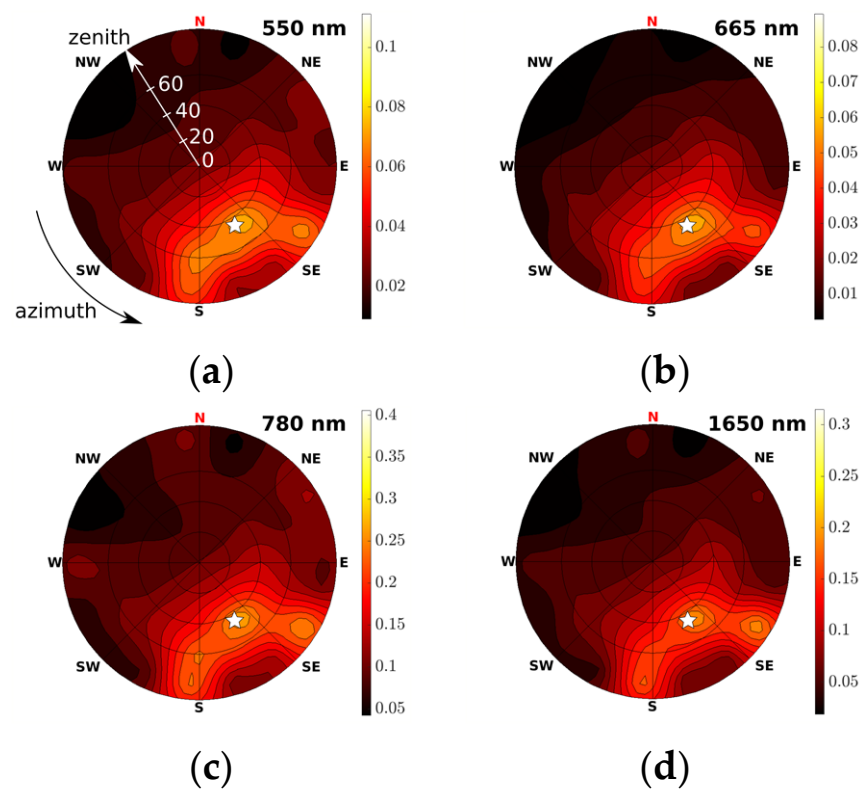
Figure A2. Simulation of the angular behaviour of the reflectance of a simulated Norway spruce forest at (**a**) 550 nm, (**b**) 665 nm, (**c**) 780 nm and (**d**) 1650 nm for the hemisphere. The white asterisk indicates the position of the sun at 45° zenith and 150° azimuth (0° zenith corresponds to the centre, 0° azimuth corresponds to the north). Simulations were performed using the Discrete Anisotropic Radiative Transfer (DART) model.
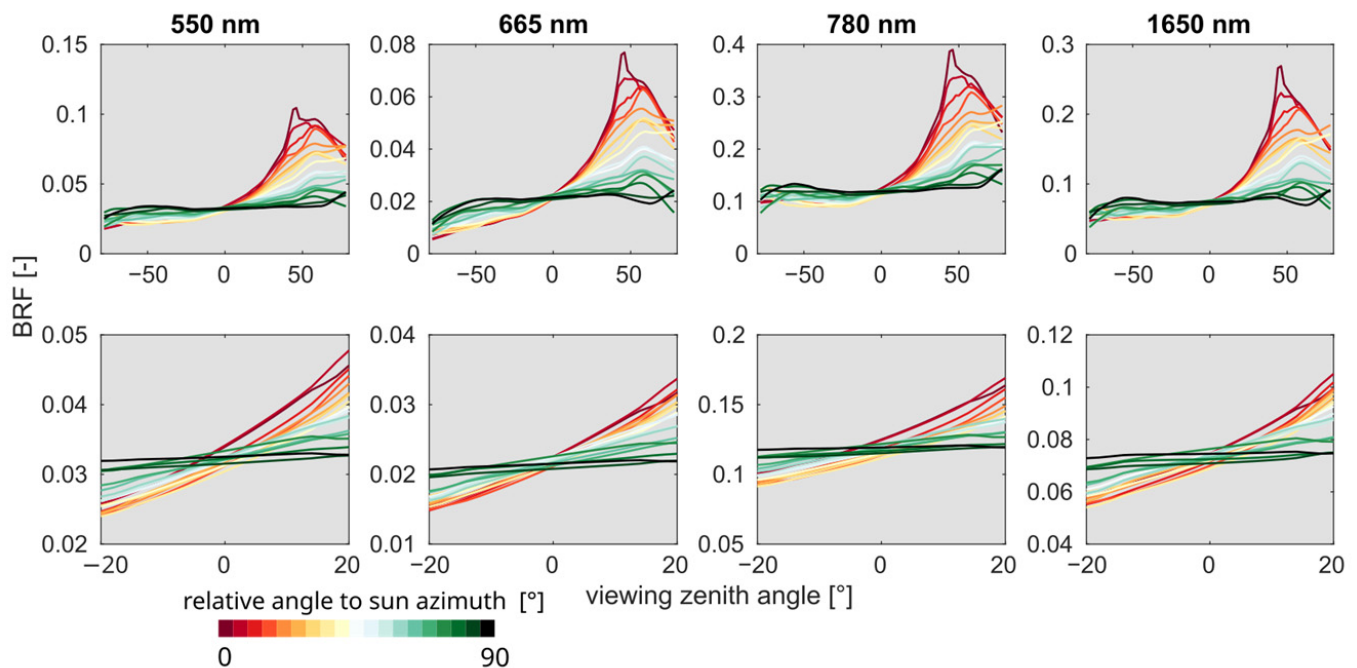
T

Figure A3. Simulated spectral reflectance Bidirectional Reflectance Factor (BRF), as in Figure A2, but plotted for individual planes. The upper graphs show reflectance for the full range of viewing zenith angles across the hemisphere (from $-90°$ to $+90°$). The lower graphs show reflectance within the field of view of the Flying Laboratory of Imaging Systems (FLIS) hyperspectral sensors (from $-20°$ to $+20°$). The colours show the variation of the plane orientation relative to the sun azimuth angle in $5°$ steps (dark red—solar principal plane, dark green—plane perpendicular to solar principal plane).

References

1. Pettorelli, N.; Laurance, W.F.; O'Brien, T.G.; Wegmann, M.; Nagendra, H.; Turner, W. Satellite Remote Sensing for Applied Ecologists: Opportunities and Challenges. *J. Appl. Ecol.* **2014**, *51*, 839–848. [CrossRef]
2. Ustin, S.L.; Middleton, E.M. Current and Near-Term Advances in Earth Observation for Ecological Applications. *Ecol. Process.* **2021**, *10*, 1. [CrossRef] [PubMed]
3. Xiao, J.; Chevallier, F.; Gomez, C.; Guanter, L.; Hicke, J.A.; Huete, A.R.; Ichii, K.; Ni, W.; Pang, Y.; Rahman, A.F.; et al. Remote Sensing of the Terrestrial Carbon Cycle: A Review of Advances over 50 Years. *Remote Sens. Environ.* **2019**, *233*, 111383. [CrossRef]
4. Farley, S.S.; Dawson, A.; Goring, S.J.; Williams, J.W. Situating Ecology as a Big-Data Science: Current Advances, Challenges, and Solutions. *BioScience* **2018**, *68*, 563–576. [CrossRef]
5. Fisher, R.A.; Koven, C.D.; Anderegg, W.R.L.; Christoffersen, B.O.; Dietze, M.C.; Farrior, C.E.; Holm, J.A.; Hurtt, G.C.; Knox, R.G.; Lawrence, P.J.; et al. Vegetation Demographics in Earth System Models: A Review of Progress and Priorities. *Glob. Chang. Biol.* **2018**, *24*, 35–54. [CrossRef]
6. Raffa, K.F.; Aukema, B.H.; Bentz, B.J.; Carroll, A.L.; Hicke, J.A.; Turner, M.G.; Romme, W.H. Cross-Scale Drivers of Natural Disturbances Prone to Anthropogenic Amplification: The Dynamics of Bark Beetle Eruptions. *BioScience* **2008**, *58*, 501–517. [CrossRef]
7. Berger, K.; Machwitz, M.; Kycko, M.; Kefauver, S.C.; Van Wittenberghe, S.; Gerhards, M.; Verrelst, J.; Atzberger, C.; Van Der Tol, C.; Damm, A.; et al. Multi-Sensor Spectral Synergies for Crop Stress Detection and Monitoring in the Optical Domain: A Review. *Remote Sens. Environ.* **2022**, *280*, 113198. [CrossRef]
8. Eitel, J.U.H.; Höfle, B.; Vierling, L.A.; Abellán, A.; Asner, G.P.; Deems, J.S.; Glennie, C.L.; Joerg, P.C.; LeWinter, A.L.; Magney, T.S.; et al. Beyond 3-D: The New Spectrum of Lidar Applications for Earth and Ecological Sciences. *Remote Sens. Environ.* **2016**, *186*, 372–392. [CrossRef]
9. Kamoske, A.G.; Dahlin, K.M.; Read, Q.D.; Record, S.; Stark, S.C.; Serbin, S.P.; Zarnetske, P.L.; Dornelas, M. Towards Mapping Biodiversity from above: Can Fusing Lidar and Hyperspectral Remote Sensing Predict Taxonomic, Functional, and Phylogenetic Tree Diversity in Temperate Forests? *Glob. Ecol. Biogeogr.* **2022**, *31*, 1440–1460. [CrossRef]
10. Lausch, A.; Borg, E.; Bumberger, J.; Dietrich, P.; Heurich, M.; Huth, A.; Jung, A.; Klenke, R.; Knapp, S.; Mollenhauer, H.; et al. Understanding Forest Health with Remote Sensing, Part III: Requirements for a Scalable Multi-Source Forest Health Monitoring Network Based on Data Science Approaches. *Remote Sens.* **2018**, *10*, 1120. [CrossRef]

11. Senf, C. Seeing the System from Above: The Use and Potential of Remote Sensing for Studying Ecosystem Dynamics. *Ecosystems* **2022**, *25*, 1719–1737. [CrossRef]

12. Hansen, M.C.; Potapov, P.V.; Moore, R.; Hancher, M.; Turubanova, S.A.; Tyukavina, A.; Thau, D.; Stehman, S.V.; Goetz, S.J.; Loveland, T.R.; et al. High-Resolution Global Maps of 21st-Century Forest Cover Change. *Science* **2013**, *342*, 850–853. [CrossRef] [PubMed]

13. White, M.A.; de BEURS, K.M.; Didan, K.; Inouye, D.W.; Richardson, A.D.; Jensen, O.P.; O'Keefe, J.; Zhang, G.; Nemani, R.R.; van Leeuwen, W.J.D.; et al. Intercomparison, Interpretation, and Assessment of Spring Phenology in North America Estimated from Remote Sensing for 1982–2006. *Glob. Chang. Biol.* **2009**, *15*, 2335–2359. [CrossRef]

14. Jung, M.; Reichstein, M.; Ciais, P.; Seneviratne, S.I.; Sheffield, J.; Goulden, M.L.; Bonan, G.; Cescatti, A.; Chen, J.; de Jeu, R.; et al. Recent Decline in the Global Land Evapotranspiration Trend Due to Limited Moisture Supply. *Nature* **2010**, *467*, 951–954. [CrossRef]

15. Verrelst, J.; Rivera-Caicedo, J.P.; Reyes-Muñoz, P.; Morata, M.; Amin, E.; Tagliabue, G.; Panigada, C.; Hank, T.; Berger, K. Mapping Landscape Canopy Nitrogen Content from Space Using PRISMA Data. *ISPRS J. Photogramm. Remote Sens.* **2021**, *178*, 382–395. [CrossRef]

16. Bachmann, M.; Alonso, K.; Carmona, E.; Gerasch, B.; Habermeyer, M.; Holzwarth, S.; Krawczyk, H.; Langheinrich, M.; Marshall, D.; Pato, M.; et al. Analysis-Ready Data from Hyperspectral Sensors—The Design of the EnMAP CARD4L-SR Data Product. *Remote Sens.* **2021**, *13*, 4536. [CrossRef]

17. Curnick, D.J.; Davies, A.J.; Duncan, C.; Freeman, R.; Jacoby, D.M.P.; Shelley, H.T.E.; Rossi, C.; Wearn, O.R.; Williamson, M.J.; Pettorelli, N. SmallSats: A New Technological Frontier in Ecology and Conservation? *Remote Sens. Ecol. Conserv.* **2022**, *8*, 139–150. [CrossRef]

18. Colomina, I.; Molina, P. Unmanned Aerial Systems for Photogrammetry and Remote Sensing: A Review. *ISPRS J. Photogramm. Remote Sens.* **2014**, *92*, 79–97. [CrossRef]

19. Dainelli, R.; Toscano, P.; Di Gennaro, S.F.; Matese, A. Recent Advances in Unmanned Aerial Vehicle Forest Remote Sensing—A Systematic Review. Part I: A General Framework. *Forests* **2021**, *12*, 327. [CrossRef]

20. Dainelli, R.; Toscano, P.; Di Gennaro, S.F.; Matese, A. Recent Advances in Unmanned Aerial Vehicles Forest Remote Sensing—A Systematic Review. Part II: Research Applications. *Forests* **2021**, *12*, 397. [CrossRef]

21. Pavelka, K.; Raeva, P.; Pavelka, K. Evaluating the Performance of Airborne and Ground Sensors for Applications in Precision Agriculture: Enhancing the Postprocessing State-of-the-Art Algorithm. *Sensors* **2022**, *22*, 7693. [CrossRef] [PubMed]

22. Pavelka, K.; Šedina, J.; Pavelka, K. Knud Rasmussen Glacier Status Analysis Based on Historical Data and Moving Detection Using RPAS. *Appl. Sci.* **2021**, *11*, 754. [CrossRef]

23. Torresan, C.; Berton, A.; Carotenuto, F.; Di Gennaro, S.F.; Gioli, B.; Matese, A.; Miglietta, F.; Vagnoli, C.; Zaldei, A.; Wallace, L. Forestry Applications of UAVs in Europe: A Review. *Int. J. Remote Sens.* **2017**, *38*, 2427–2447. [CrossRef]

24. Chadwick, K.; Asner, G. Organismic-Scale Remote Sensing of Canopy Foliar Traits in Lowland Tropical Forests. *Remote Sens.* **2016**, *8*, 87. [CrossRef]

25. Cogliati, S.; Sarti, F.; Chiarantini, L.; Cosi, M.; Lorusso, R.; Lopinto, E.; Miglietta, F.; Genesio, L.; Guanter, L.; Damm, A.; et al. The PRISMA Imaging Spectroscopy Mission: Overview and First Performance Analysis. *Remote Sens. Environ.* **2021**, *262*, 112499. [CrossRef]

26. Cooper, S.; Okujeni, A.; Pflugmacher, D.; Van Der Linden, S.; Hostert, P. Combining Simulated Hyperspectral EnMAP and Landsat Time Series for Forest Aboveground Biomass Mapping. *Int. J. Appl. Earth Obs. Geoinf.* **2021**, *98*, 102307. [CrossRef]

27. Chlus, A.; Townsend, P.A. Characterizing Seasonal Variation in Foliar Biochemistry with Airborne Imaging Spectroscopy. *Remote Sens. Environ.* **2022**, *275*, 113023. [CrossRef]

28. Novotný, J.; Navrátilová, B.; Janoutová, R.; Oulehle, F.; Homolová, L. Influence of Site-Specific Conditions on Estimation of Forest above Ground Biomass from Airborne Laser Scanning. *Forests* **2020**, *11*, 268. [CrossRef]

29. Chadwick, K.D.; Brodrick, P.G.; Grant, K.; Goulden, T.; Henderson, A.; Falco, N.; Wainwright, H.; Williams, K.H.; Bill, M.; Breckheimer, I.; et al. Integrating Airborne Remote Sensing and Field Campaigns for Ecology and Earth System Science. *Methods Ecol. Evol.* **2020**, *11*, 1492–1508. [CrossRef]

30. Forzieri, G.; Tanteri, L.; Moser, G.; Catani, F. Mapping Natural and Urban Environments Using Airborne Multi-Sensor ADS40–MIVIS–LiDAR Synergies. *Int. J. Appl. Earth Obs. Geoinf.* **2013**, *23*, 313–323. [CrossRef]

31. Urban, J.; Pikl, M.; Zemek, F.; Novotný, J. Using Google Street View Photographs to Assess Long-Term Outdoor Thermal Perception and Thermal Comfort in the Urban Environment during Heatwaves. *Front. Environ. Sci.* **2022**, *10*, 878341. [CrossRef]

32. Asner, G.P. Carnegie Airborne Observatory: In-Flight Fusion of Hyperspectral Imaging and Waveform Light Detection and Ranging for Three-Dimensional Studies of Ecosystems. *J. Appl. Remote Sens.* **2007**, *1*, 013536. [CrossRef]

33. Asner, G.P.; Knapp, D.E.; Boardman, J.; Green, R.O.; Kennedy-Bowdoin, T.; Eastwood, M.; Martin, R.E.; Anderson, C.; Field, C.B. Carnegie Airborne Observatory-2: Increasing Science Data Dimensionality via High-Fidelity Multi-Sensor Fusion. *Remote Sens. Environ.* **2012**, *124*, 454–465. [CrossRef]

34. Kampe, T.U. NEON: The First Continental-Scale Ecological Observatory with Airborne Remote Sensing of Vegetation Canopy Biochemistry and Structure. *J. Appl. Remote Sens.* **2010**, *4*, 043510. [CrossRef]

35. Cook, B.; Corp, L.; Nelson, R.; Middleton, E.; Morton, D.; McCorkel, J.; Masek, J.; Ranson, K.; Ly, V.; Montesano, P. NASA Goddard's LiDAR, Hyperspectral and Thermal (G-LiHT) Airborne Imager. *Remote Sens.* **2013**, *5*, 4045–4066. [CrossRef]
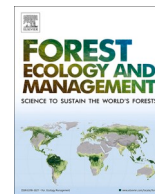
36. ARES | Airborne Research of the Earth System. Available online: https://ares-observatory.ch/ (accessed on 7 June 2023).
37. NEODAAS-Airborne. Available online: https://nerc-arf-dan.pml.ac.uk/ (accessed on 7 June 2023).
38. FLIS—Department of Airborne Activities. Available online: https://olc.czechglobe.cz/en/flis-2/ (accessed on 8 June 2023).
39. Hanuš, J.; Fabiánek, T.; Fajmon, L. Potential of Airborne Imaging Spectroscopy at CzechGlobe. *ISPRS Int. Arch. Photogramm. Remote Sens. Spat. Inf. Sci.* **2016**, *XLI-B1*, 15–17. [CrossRef]
40. Riegl. *Airborne Laser Scanner LMS-Q780 General Description and Data Interface (Manual)*; Riegl: Horn, Austria, 2014.
41. CzechGlobe | Virtual Tour. Available online: http://czechglobe.pano3d.eu (accessed on 8 June 2023).
42. Rascher, U.; Alonso, L.; Burkart, A.; Cilia, C.; Cogliati, S.; Colombo, R.; Damm, A.; Drusch, M.; Guanter, L.; Hanus, J.; et al. Sun-Induced Fluorescence—A New Probe of Photosynthesis: First Maps from the Imaging Spectrometer *HyPlant*. *Glob. Chang. Biol.* **2015**, *21*, 4673–4684. [CrossRef]
43. Siegmann, B.; Alonso, L.; Celesti, M.; Cogliati, S.; Colombo, R.; Damm, A.; Douglas, S.; Guanter, L.; Hanuš, J.; Kataja, K.; et al. The High-Performance Airborne Imaging Spectrometer HyPlant—From Raw Images to Top-of-Canopy Reflectance and Fluorescence Products: Introduction of an Automatized Processing Chain. *Remote Sens.* **2019**, *11*, 2760. [CrossRef]
44. FLEX—Earth Online. Available online: https://earth.esa.int/eogateway/missions/flex (accessed on 23 March 2023).
45. Launching the Revolutionary PTR-TOF 6000 X2 Trace VOC Analyzer | IONICON. Available online: https://www.ionicon.com/blog/2017/launching-the-revolutionary-ptr-tof-6000-x2-trace-voc-analyzer (accessed on 17 May 2023).
46. Dashora, A.; Lohani, B.; Deb, K. Two-Step Procedure of Optimisation for Flight Planning Problem for Airborne LiDAR Data Acquisition. *Int. J. Math. Model. Numer. Optim.* **2013**, *4*, 323. [CrossRef]
47. Richter, R.; Schläpfer, D. *Atmospheric/Topographic Correction for Airborne Imagery (ATCOR-4 User Guide) 2021*; ReSe Applications LLC: Langeggweg, Switzerland, 2021.
48. Itres. *Standard Processing and Data QA Manual*; Itres: Calgary, AB, Canada, 2013.
49. Richter, R.; Schläpfer, D. Geo-Atmospheric Processing of Airborne Imaging Spectrometry Data. Part 2: Atmospheric/Topographic Correction. *Int. J. Remote Sens.* **2002**, *23*, 2631–2649. [CrossRef]
50. Schläpfer, D.; Richter, R. Geo-Atmospheric Processing of Airborne Imaging Spectrometry Data. Part 1: Parametric Orthorectification. *Int. J. Remote Sens.* **2002**, *23*, 2609–2630. [CrossRef]
51. Inamdar, D.; Kalacska, M.; Darko, P.O.; Arroyo-Mora, J.P.; Leblanc, G. Spatial Response Resampling (SR2): Accounting for the Spatial Point Spread Function in Hyperspectral Image Resampling. *MethodsX* **2023**, *10*, 101998. [CrossRef] [PubMed]
52. Yang, H.; Zhang, L.; Ong, C.; Rodger, A.; Liu, J.; Sun, X.; Zhang, H.; Jian, X.; Tong, Q. Improved Aerosol Optical Thickness, Columnar Water Vapor, and Surface Reflectance Retrieval from Combined CASI and SASI Airborne Hyperspectral Sensors. *Remote Sens.* **2017**, *9*, 217. [CrossRef]
53. Berk, A.; Anderson, G.P.; Bernstein, L.S.; Acharya, P.K.; Dothe, H.; Matthew, M.W.; Adler-Golden, S.M.; Chetwynd, J.H., Jr.; Richtsmeier, S.C.; Pukall, B.; et al. MODTRAN4 radiative transfer modeling for atmospheric correction. In Proceedings of the 1999 SPIE's International Symposium on Optical Science Engineering, and Instrumentation, Denver, CO, USA, 18–23 July 1999; p. 348. [CrossRef]
54. Guanter, L.; Gómez-Chova, L.; Moreno, J. Coupled Retrieval of Aerosol Optical Thickness, Columnar Water Vapor and Surface Reflectance Maps from ENVISAT/MERIS Data over Land. *Remote Sens. Environ.* **2008**, *112*, 2898–2913. [CrossRef]
55. Green, R.O.; Conel, J.E.; Margolis, J.; Chovit, C.; Faust, J. In-Flight Calibration and Validation of the Airborne Visible/Infrared Imaging Spectrometer (AVIRIS). 1996. Available online: https://hdl.handle.net/2014/25023 (accessed on 20 May 2023).
56. Secker, J.; Staenz, K.; Gauthier, R.P.; Budkewitsch, P. Vicarious Calibration of Airborne Hyperspectral Sensors in Operational Environments. *Remote Sens. Environ.* **2001**, *76*, 81–92. [CrossRef]
57. He, W.; Yao, Q.; Li, C.; Yokoya, N.; Zhao, Q. Non-Local Meets Global: An Integrated Paradigm for Hyperspectral Denoising. In Proceedings of the 2019 IEEE/CVF Conference on Computer Vision and Pattern Recognition (CVPR), Long Beach, CA, USA, 15–20 June 2019; pp. 6861–6870.
58. Copernicus | Climate Data Store. Available online: https://cds.climate.copernicus.eu/#!/home (accessed on 8 June 2023).
59. Guillory, A. ERA5. Available online: https://www.ecmwf.int/en/forecasts/datasets/reanalysis-datasets/era5 (accessed on 23 March 2023).
60. Gillespie, A.; Rokugawa, S.; Matsunaga, T.; Cothern, J.S.; Hook, S.; Kahle, A.B. A Temperature and Emissivity Separation Algorithm for Advanced Spaceborne Thermal Emission and Reflection Radiometer (ASTER) Images. *IEEE Trans. Geosci. Remote Sens.* **1998**, *36*, 1113–1126. [CrossRef]
61. Cheng, J.; Liang, S.; Wang, J.; Li, X. A Stepwise Refining Algorithm of Temperature and Emissivity Separation for Hyperspectral Thermal Infrared Data. *IEEE Trans. Geosci. Remote Sens.* **2010**, *48*, 1588–1597. [CrossRef]
62. Kealy, P.S.; Hook, S.J. Separating Temperature and Emissivity in Thermal Infrared Multispectral Scanner Data: Implications for Recovering Land Surface Temperatures. *IEEE Trans. Geosci. Remote Sens.* **1993**, *31*, 1155–1164. [CrossRef]
63. Sobrino, J.A.; Jimenez-Munoz, J.C.; Soria, G.; Romaguera, M.; Guanter, L.; Moreno, J.; Plaza, A.; Martinez, P. Land Surface Emissivity Retrieval From Different VNIR and TIR Sensors. *IEEE Trans. Geosci. Remote Sens.* **2008**, *46*, 316–327. [CrossRef]
64. Vermote, E.F.; Tanre, D.; Deuze, J.L.; Herman, M.; Morcette, J.-J. Second Simulation of the Satellite Signal in the Solar Spectrum, 6S: An Overview. *IEEE Trans. Geosci. Remote Sens.* **1997**, *35*, 675–686. [CrossRef]
65. Pérez-Planells, L.; Valor, E.; Coll, C.; Niclòs, R. Comparison and Evaluation of the TES and ANEM Algorithms for Land Surface Temperature and Emissivity Separation over the Area of Valencia, Spain. *Remote Sens.* **2017**, *9*, 1251. [CrossRef]

66. Payan, V.; Royer, A. Analysis of Temperature Emissivity Separation (TES) Algorithm Applicability and Sensitivity. *Int. J. Remote Sens.* **2004**, *25*, 15–37. [CrossRef]

67. Matsunaga, T. A Temperature-Emissivity Separation Method Using an Empirical Relationship between the Mean, the Maximum, and the Minimum of the Thermal Infrared Emissivity Spectrum. *J. Remote Sens. Soc. Jpn.* **1994**, *14*, 230–241.

68. Pivovarnik, M. New Approaches in Airborne Thermal Image Processing for Landscape Assessment. Ph.D. Thesis, Brno University of Technology, Brno, Czech Republic, 2017.

69. Sabol, D.E., Jr.; Gillespie, A.R.; Abbott, E.; Yamada, G. Field Validation of the ASTER Temperature–Emissivity Separation Algorithm. *Remote Sens. Environ.* **2009**, *113*, 2328–2344. [CrossRef]

70. Michel, A.; Granero-Belinchon, C.; Cassante, C.; Boitard, P.; Briottet, X.; Adeline, K.R.M.; Poutier, L.; Sobrino, J.A. A New Material-Oriented TES for Land Surface Temperature and SUHI Retrieval in Urban Areas: Case Study over Madrid in the Framework of the Future TRISHNA Mission. *Remote Sens.* **2021**, *13*, 5139. [CrossRef]

71. Mapserver CzechGlobe. Available online: https://mapserver.czechglobe.cz/en/map (accessed on 8 June 2023).

72. EUFAR—The EUropean Facility for Airborne Research. Available online: http://eufar.net/ (accessed on 8 June 2023).

73. Open Access to CzeCOS Research Infrastructure Hosted byGlobal Change Research Institute CAS. Available online: https://www.czechglobe.cz/en/open-access-en/czecos-en/ (accessed on 8 June 2023).

74. Gastellu-Etchegorry, J.-P.; Lauret, N.; Yin, T.; Landier, L.; Kallel, A.; Malenovsky, Z.; Bitar, A.A.; Aval, J.; Benhmida, S.; Qi, J.; et al. DART: Recent Advances in Remote Sensing Data Modeling With Atmosphere, Polarization, and Chlorophyll Fluorescence. *IEEE J. Sel. Top. Appl. Earth Obs. Remote Sens.* **2017**, *10*, 2640–2649. [CrossRef]

75. Malenovský, Z.; Regaieg, O.; Yin, T.; Lauret, N.; Guilleux, J.; Chavanon, E.; Duran, N.; Janoutová, R.; Delavois, A.; Meynier, J.; et al. Discrete Anisotropic Radiative Transfer Modelling of Solar-Induced Chlorophyll Fluorescence: Structural Impacts in Geometrically Explicit Vegetation Canopies. *Remote Sens. Environ.* **2021**, *263*, 112564. [CrossRef]

76. Janoutová, R.; Homolová, L.; Novotný, J.; Navrátilová, B.; Pikl, M.; Malenovský, Z. Detailed Reconstruction of Trees from Terrestrial Laser Scans for Remote Sensing and Radiative Transfer Modelling Applications. *Silico Plants* **2021**, *3*, diab026. [CrossRef]

77. Homolová, L.; Janoutová, R.; Lukeš, P.; Hanuš, J.; Novotný, J.; Brovkina, O.; Loayza Fernandez, R.R. In Situ Data Supporting Remote Sensing Estimation of Spruce Forest Parameters at the Ecosystem Station Bílý Kříž. *Beskydy* **2018**, *10*, 75–86. [CrossRef]

Appendix 2

Article 2

Comparison of field survey and remote sensing techniques for detection of bark beetle-infested trees

Vojtěch Bárta [a,*], Jan Hanuš [a], Lumír Dobrovolný [b], Lucie Homolová [a]

[a] *Global Change Research Institute of the Czech Academy of Sciences, Department of Remote Sensing, Bělidla 986/4a, 603 00 Brno, Czech Republic*
[b] *Mendel University in Brno – University Forest Enterprise, 613 00 Brno, Czech Republic*

ARTICLE INFO

ABSTRACT

Detection in the early phase of bark beetle infestation is a vital task for proactive management strategies, as practiced in most Central European forests, to minimize economic losses due to bark beetle infestation and to mitigate their further spreading. For this work, remote sensing methods are coming to be in great demand as an objective approach to enable monitoring bark beetle infestation even at individual tree level.

This case study monitored bark beetle (*Ips typographus*) activity at local level in Norway spruce forest in the Czech Republic. The main aim of this study was to compare the remote sensing methods against classical field survey conducted by forest workers in detecting newly infested trees.

To compare these two methods, an extensive field and aerial campaign was conducted in the southern part of the Czech Republic during 2020. Bark beetle infestation was monitored by traditional methods (i.e. field survey) on a weekly basis from mid-March to mid-September. During the same period, aerial scans were performed once per month (seven in total) using a CASI-1500 hyperspectral sensor (visible and near-infrared, 400–1000 nm) with spatial resolution of 0.5 m. This work mapped transition from healthy up to red attack of 75 Norway spruce trees that were infested during the same week. The same number of healthy trees were added to the data set for hyperspectral data analysis. Both groups were analysed by vegetation indices, with emphasis on effect caused in the canopy by bark beetles.

The success rate for bark beetle detection is always associated with acquisition time. In order to define the optimal time for data acquisition, we employed a phenology model for *I. typographus* (RITY 2.0) to take into consideration bark beetle development.

The results of the experiment showed that classic field survey detected infested trees earlier than did analysis using remote sensing data from the visible and near-infrared region. The difference was 23 days for the most successful indices (i.e. REIP, PRI, and $ANCB_{650-720}$) in our test. Nevertheless, both methods detected the infested trees within 6 weeks after infestation, which is the recommended period for taking measures to prevent bark beetles from spreading further, and thus hyperspectral imagery can be used as a valid information source for bark beetle detection.

1. Introduction

The bark beetle *Ips typographus (L.)* is an important biotic agent presenting a threat to Eurasian forests. An outbreak of its population caused severe damage to Norway spruce forests (*Picea abies* (L.) H. karst.) in the countries of Central Europe during the period 2015–2019 (Ogris et al., 2019). At that time, the volume of salvage felling has been increasing every year. In the Czech Republic, for instance, the annual volume of spruce salvage felling due to insect damage never exceeded 3 million m^3 in the period 2006–2015, since then it is steadily increasing

to about 22 million m^3 in 2019 (CZSO, 2020; Fernandez-Carrillo et al., 2020). Other European countries also recorded abnormally high rates of salvage felling.

Mass diebacks in European countries are linked to long-term drought and above-average temperatures, which favour the expansion of bark beetles. Bark beetle development is directly affected by phloem temperature (which is related, but not necessarily the same as ambient air temperature) (Rouault et al., 2006). In addition, water stress increases the chance that bark beetles will successfully attack a tree (Rouault et al., 2006). Owing to climate changes, many forest stands will be

---

Location of interest
Trees with no infestation symptoms until September 15th
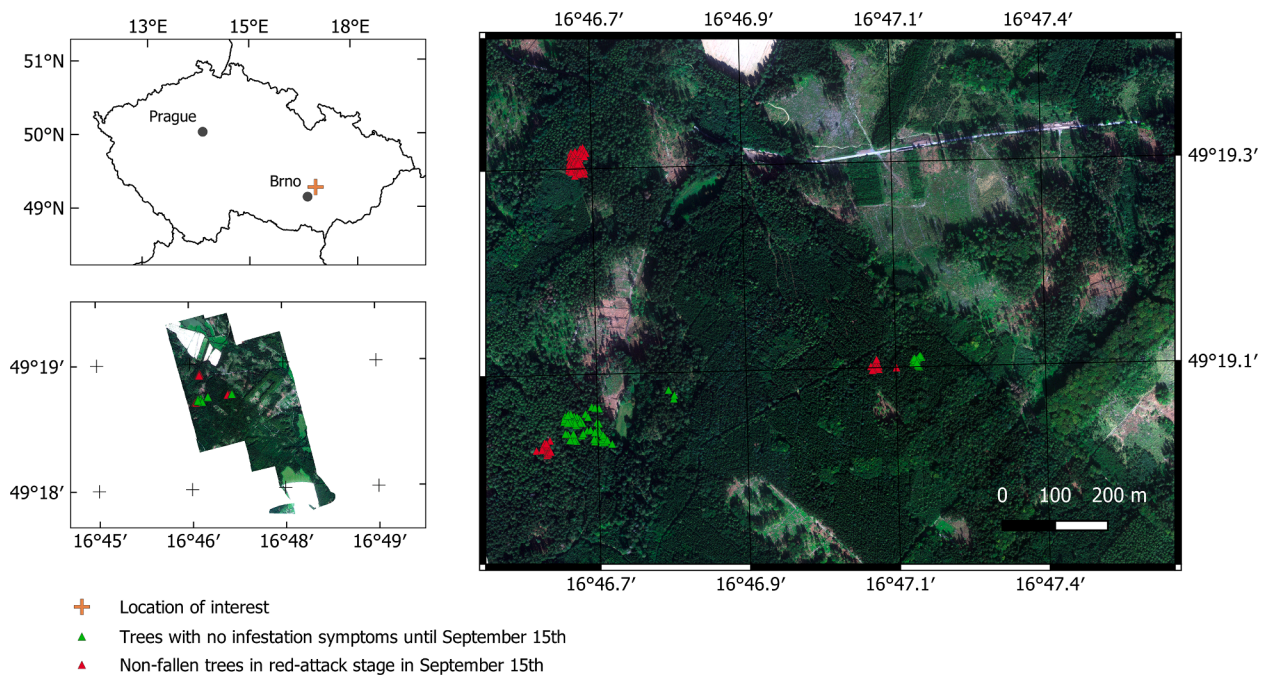Non-fallen trees in red-attack stage in September 15th

Fig. 1. The study area.

threatened more often by drought in future (Jakoby et al., 2019).

To deal with greater voltinism (number of annual broods) as a consequence of rising temperature, the gathering of multiple outputs from different sources (like remote sensing, field survey, and phenology modelling) is necessary for forest managers to prevent massive outbreaks and mitigate economic losses in the years to come.

The infested trees in a managed forest are traditionally located during field survey, when forest workers look for holes in the bark or frass (fine sawdust-like powder) at the bottoms of trees. Such surveys are able to identify trees in early attack stage (known as "green attack", to use remote sensing nomenclature), but the method is laborious and hardly applicable to large areas (Abdullah et al., 2018, 2019a). Alternatively, remote sensing presents an effective tool for large-scale monitoring using satellite, airborne, or unmanned aerial vehicle (UAV) data. Remote sensing nomenclature divides bark beetle-induced mortality in conifers into three stages: green-attack, red-attack, and grey-attack (Wulder et al., 2006). These were named for the foliage colour accompanying each specific stage. In the first of these, green-attack, a tree has been attacked successfully and breeding is underway, but the needles remain green without any visible changes. The other two stages, red- and grey-attack, refer to a dead tree with intense changes in its canopy and that already has been abandoned by the beetles. Therefore, only the green-attack stage is relevant for proactive management measures to process infested trees before a new (filial or sister) bark beetle generation is established.

Senf et al. (2017) reviewed remote sensing-based methods for bark beetle disturbance mapping and concluded that 20% of studies used very high spatial resolution data, whereas 10% of studies used hyperspectral data. Multiple bark beetle-induced mortality classes (red, green-attack, healthy, etc.) based upon airborne hyperspectral data in high spatial resolution (7 and 5 m; 7 and 4 m, respectively) were examined by Fassnacht et al. (2014) and Lausch et al. (2013). The use of coarse, medium, or high spatial resolution data from multispectral systems have preeminent position and are mainly intended for monitoring large-scale disturbance, at least on the level of groups of trees. For proactive management measures, it is essential to identify small, isolated outbreaks that could be missed in coarse and medium spatial resolution imagery (Dash et al., 2017). Increasing numbers of studies using UAV-

mounted, low-cost, red-greenblue (RGB), multispectral, or hyperspectral sensors have been appearing in recent years. These sensors provide high spatial resolution data (ground sample distance, GSD < 1 m) able to support individual tree-level approaches.

For example, Klouček et al. (2019) used low-cost and modified near-infrared sensors for detecting different stages of infested trees at individual-tree level. Näsi et al. (2018) compared UAV and airborne hyperspectral data sets (GSD = 10–12 cm and 50 cm) to evaluate bark beetle damage and found that the UAV's finer resolution provided better results. Zhang et al. (2018) used UAV-based hyperspectral imaging (GSD = 56 cm) to identify the degree of damage caused by Chinese pine caterpillar (*Dendrolimus tabulaeformis)*.

Despite recent deployment of hyperspectral/multispectral sensors on UAV platforms for mapping infestation at single-tree level, there are a few studies only that combine both high spatial and temporal resolution data (acquisition more than five times a year). One of the pioneering studies assessing forest health from time-series of multispectral imagery (10 acquisitions per year) was published by Dash et al. (2017). Those authors simulated disease outbreak in mature Monterey Pine (*Pinus radiata)* stands to develop methods for monitoring physiological stress from the early stages.

A similar approach had not yet been applied for monitoring outbreak of bark beetle *I. typographus*, even though the identification of infested trees is critical for maintaining healthy and highly productive forests. To fill this gap, this study monitored a natural bark beetle outbreak in Norway spruce stands while incorporating not merely remote sensing data but also other information from field survey, pheromone traps, and a bark beetle phenology model. Comparison of these information sources could help to determine the limits in practice of these methods for bark beetle detection.

2. Material and methods

2.1. Common practice of bark beetle monitoring

The location of infested trees in managed forest within the Czech Republic is today still based upon field survey, a method that is quite subjective, laborious, time-consuming, and, therefore, unsuitable for a

vast area. An infested tree is identified according to one or more specific traits that accompany bark beetle attack, such as frass (light-brown sawdust-like powder) on the bark in the basal part (Abdullah et al., 2018; Jeger et al., 2017), as shown in **Appendix A,** Fig. A1(a), thereby revealing bark beetle presence from an early infestation stage (i.e. the so-called green-attack stage). Another sign is entrance holes made by the beetles and occurring in the lower parts of the stem in the late infestation stage (CABI, 2021), as shown in **Appendix** Fig. A1(b). As the infestation progresses, the needle colour in conifers becomes lighter and needles often fall to the ground. The bark from the higher parts of the trunk flakes off while the needles at the top of the tree still may be green, as shown in **Appendix** Fig. A1(c). Bark shedding continues throughout the red-attack stage, which is when a tree no longer has any green needles, and the process ends in the grey-attack stage, at which point the tree is dead.

2.2. Study area

The study area was situated in the southern part of the Czech Republic in mixed, productive forests (Fig. 1). The selected forest stands are composed in 38% of coniferous trees (19% spruce, 8% pine, 8% larch and 3% other species) and 62% of broadleaves (33% beech, 15% oak, 8% hornbeam and 6% other species), with altitude ranging from 200 to 570 m, mean annual temperature 7.5 °C, and mean annual rainfall 610 mm (Fernandez-Carrillo et al., 2020). We primarily focused on Norway spruce forest stands in age classes 30–40 years and 90–100 years, which are prevalent forest age classes within the study area. Trends from past seasons and knowledge of local forest manages helped us to locate approximately 3 km^2 of spruce dominated forests where the probability of infestation would be highest in the 2020 season.

2.3. Monitoring of bark beetle activity and selection of trees

The Norway spruces inside the area of interest were monitored by forest workers on a weekly basis. The field survey started on 3 March and ended on 6 August 2020. The key issue was to record the time and place of the first filial generation infestation, and further to observe beetles' spreading to other areas in the forest stands. Similar to a study by Abdullah et al. (2018), identification of an infested tree was based upon spotting characteristic traits after bark beetles' successful attack, such as dry dust at the bottom of the tree or on the trunk (more detailed description in **Appendix A**). Infested trees were searched during the entire growing season, we focused only on those trees that were evidently infested during 2020, but were not cut until after the last airborne data acquisition (i.e., until after 15 September 2020). At the end we selected 75 infested spruce trees inside the forest stand (not on the stand edges) in two age categories, with 15 samples from age class 30–40 years and 60 from age class 90–100 years. Coordinates of the individual trees were recorded by a GPS, (for the first time using a less accurate Garmin, Oregon 650, only until after the trees were cut, Topcon, HiPer Pro device with centimetre accuracy was used to measured precise tree location in the centre of a tree stump) for efficient localization in hyperspectral image. An equal number of healthy trees from the same age classes were selected in the vicinity of those that were infested in order to prevent errors arising from differences in illumination and while taking into account forest stand condition (Fig. 1). Forest structure was also considered during the sample selection, with trees on steep slopes or trees surrounded by different tree species being excluded from the analysis to minimize misclassification.

Additionally, pheromone traps were also used to gather information about bark beetle activity in-situ. The traps were located at two places, being within a 1 km distance from the farthest group of infested trees that were monitored for this study and reached the red-attack stage at the end of the growing season (i.e. red triangles on Fig. 1). The data obtained from these traps were used to check bark beetle generation development based upon modelling (more information in 2.6.).

Table 1
Hyperspectral data acquisitions in 2020.

Flight no.	Time	Day of year (DOY)
1	2 April	93
2	23 April	114
3	18 May	139
4	13 June	165
5	10 July	192
6	12 August	225
7	15 September	259

Table 2
Tested spectral vegetation indices used for early detection.

Index	Formula	Reference
Piecewise index PI B(710 + 738–522)	$PI = R_{710} + R_{738} - R_{522}$	(Zhang et al., 2018)
Greenness GI	$GI = \dfrac{GREEN}{RED}$	(Klouček et al., 2019; le Maire et al., 2004)
NDVI GREEN/NIR	$NDVI\ GREEN/NIR = \dfrac{NIR - GREEN}{NIR + GREEN}$	(Gitelson and Merzlyak, 1997)
Red-edge inflection point	$REIP = 705 +$ $35\left(\dfrac{\left(\dfrac{R_{665} + R_{783}}{2}\right) - R_{705}}{R_{740} - R_{705}}\right)$	(Herrmann et al., 2011)
Normalized difference photochemical reflectance index PRI	$PRI = \dfrac{R_{528} - R_{567}}{R_{528} + R_{567}}$	(Zarco-Tejada et al., 2001)
ANCB index CR (650–720)[a]	$ANCB_{650-720} =$ $\dfrac{1}{2}\sum_{i=1}^{n-1}(\lambda_{i+1} - \lambda_i)(R_{CR(\lambda_{i+1})} + R_{CR(\lambda_i)})\bullet\dfrac{1}{BD_{680}}$	(Malenovský et al., 2013)

[a] Where $ANCB_{650-720}$ is designated as the area under the continuum removed (CR) reflectance between 650 nm and 720 nm and normalized by the CR band depth at 680 nm (BD_{680}), where $R_{CR(\lambda_{i+1})}$ and $R_{CR(\lambda_i)}$ are values of CR reflectance at the j and $j + 1$ bands, λ_j and λ_{j+1} are wavelengths of the j and $j + 1$ bands, and n refers to number of bands, in this case $n = 6$ (Malenovský et al., 2013).
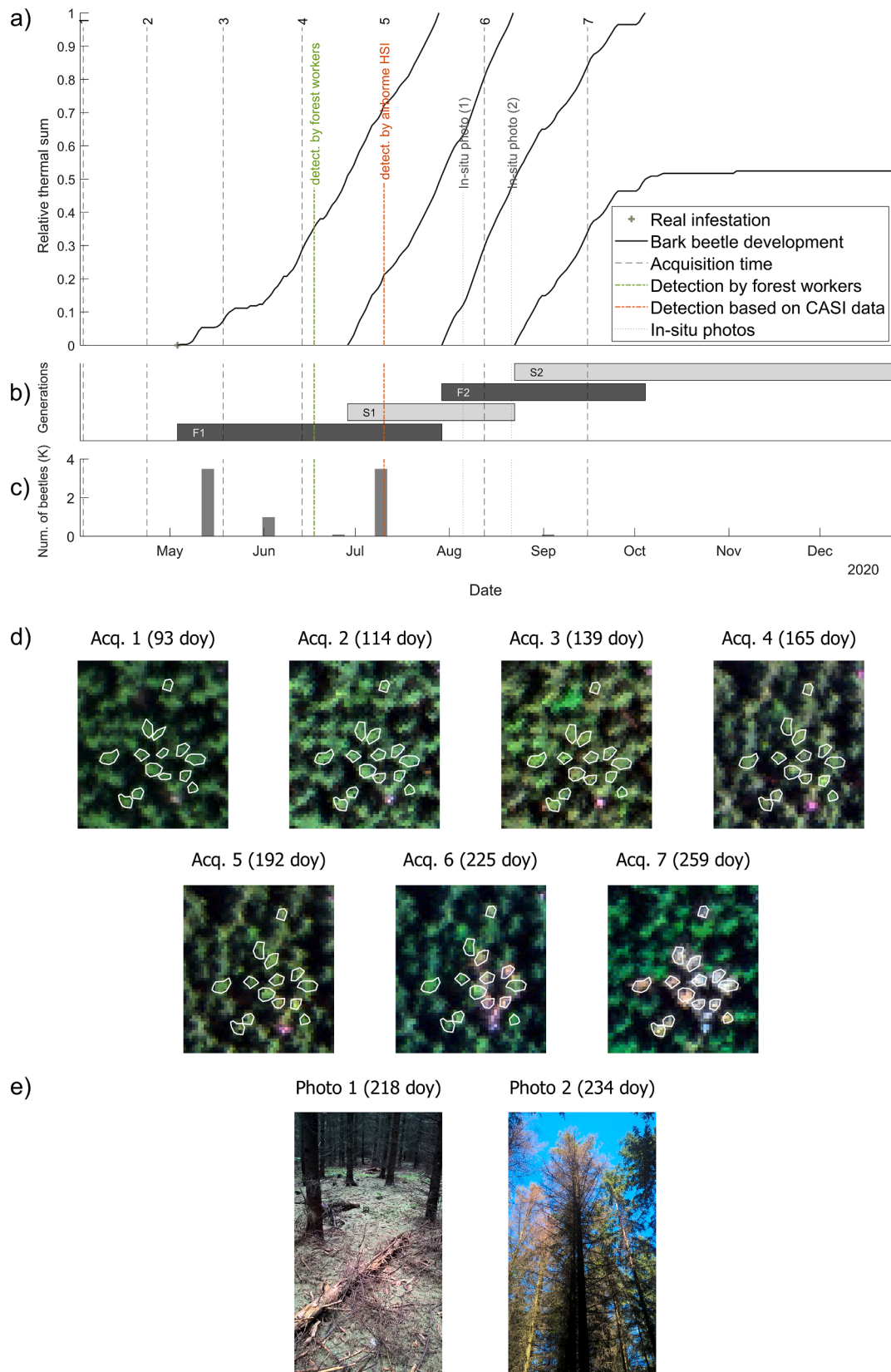
2.4. Remote sensing data

The Flying Laboratory of Imaging Systems (FLIS), operated by Global Change Research Institute of the Czech Academy of Sciences, was used to acquire airborne hyperspectral images (Hanuš et al., 2016). FLIS equipped with a CASI 1500 hyperspectral spectroradiometer operates at 500 m altitude, which allows capturing images in spatial resolution of 0.5 m within wavelength range 380–1050 nm in 48 spectral channels with full width at half maximum (FWHM) 14.25 nm.

Airborne campaigns were carried out seven times during 2020 (Table 1), with about one month gap between data acquisition (the exact acquisition dates were driven by suitable, sunny and cloud-free weather conditions).

The hyperspectral imagery covered area 1.5 × 1.5 km approximately, the final mosaic was comprised of 2 or 3 lines for each term. The direction of flight lines was planned individually for each term according to actual sun azimuth to minimize bidirectional reflectance distribution function (BRDF) effect on the image data.

The acquired data were pre-processed by a standard processing chain to a mosaic of atmospherically corrected surface reflectance as described in (Hanuš et al., 2016; http://olc.czechglobe.cz/en/processing/casi-sasi -data-processing/).

Fig. 2. Combining of simulated bark beetle development, remote sensing hyperspectral data, and field survey information to map a decay process in the course of time. The section (a) refers to bark beetle development on the side since the first (fallen and uprooting) trees were infested (i.e. since 3 May 2020). The number of generations is presented in the section (b), it seems that the two filial and two sister generations were established. The figure of catches from pheromone traps are shown in section (c). The RGB images form each data acquisition time are shown in section (d), the figure is completed by in-situ photo captured during field surveys in section (e).
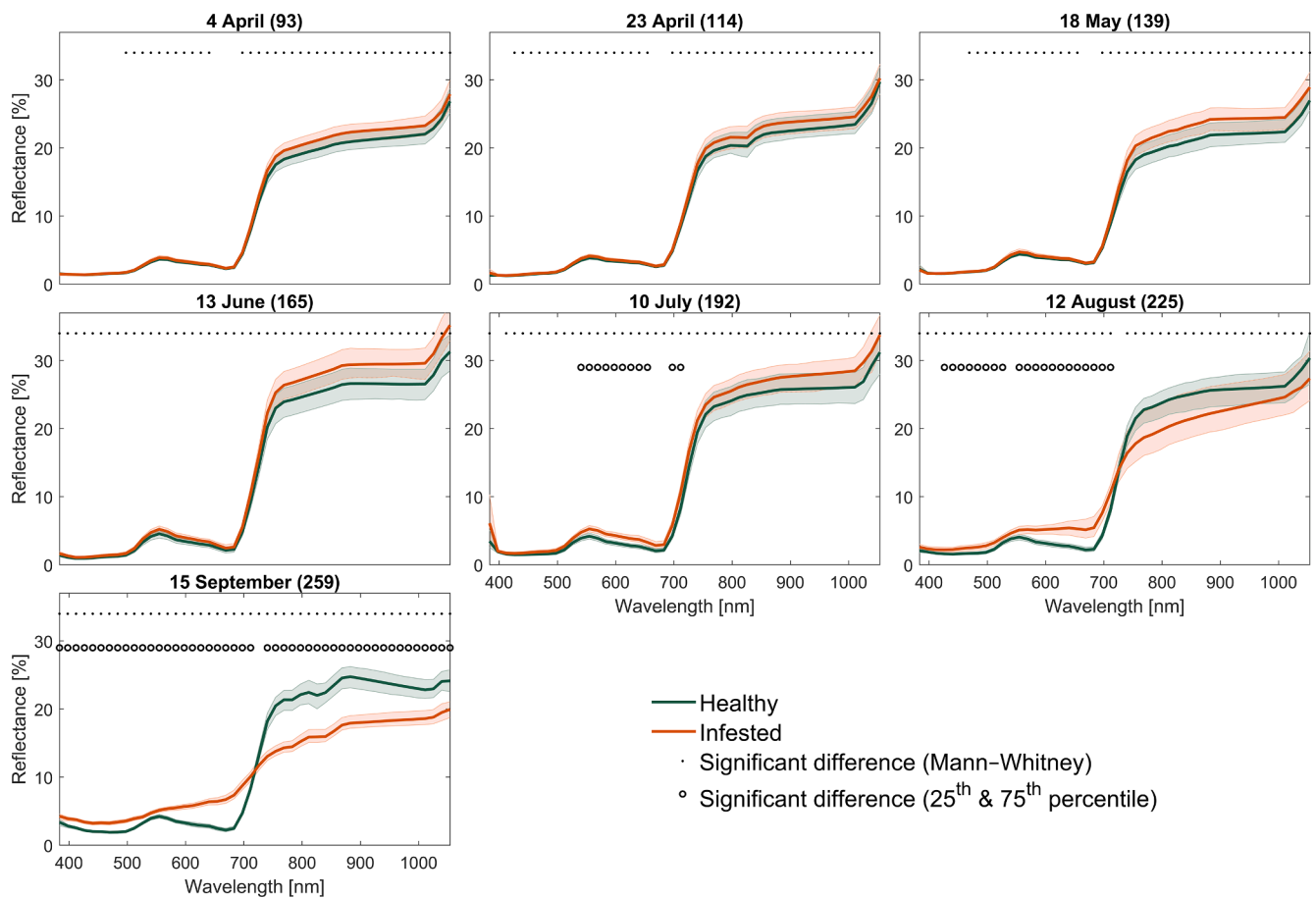
Fig. 3. Spectral signature of healthy and infested groups for each airborne image acquisition. Solid lines represent mean spectral values. Shaded areas indicate 25th and 75th percentiles. The mean spectral values for each group were calculated from the mean spectral values of trees within the group. Significant differences between groups are identified by two methods, Mann-Witney (dots), 25th and 75th percentile (circles).

2.5. Analysis of spectral indices

First, our sample trees were identified on hyperspectral images from all acquisition using their GPS coordinates. Only the sunlit parts of a tree crown were manually selected in order to exclude the shadowed pixels (a single tree crown includes 28 pixels on average). Subsequently, 50% of the brightest pixels at 550 nm in each tree crown were picked out, and the mean spectral value for each individual tree was then calculated. This approach of analysing a single spectral feature for each individual tree rather than analysing each pixel within tree crown separately has been employed in similar studies evaluating bark beetle damage (Näsi et al., 2015, 2018).

Average tree crown reflectance was then used to compute vegetation indices.

We predominantly selected indices considered as most effective according to current studies dealing with bark beetle detection via hyperspectral/multispectral imagery, most of them having already been employed to detect in particular *I. typographus* (Fassnacht et al., 2014; Klouček et al., 2019; Näsi et al., 2018). An exceptions was an index that had been used in case of defoliating pests (e.g. D. tabulaeformis in the study by Zhang et al., (2018)) and one that is sensitive to changes in foliar pigment, which can be considered as plant reaction to a stress factor (Malenovský et al., 2013). The indices are detailed in Table 2.

To separate the healthy and infested groups two statistical approaches were employed. Firstly, the difference was tested using Mann-Witney *U* test at the 5% significant level using Statistics and Machine Learning Toolbox in MATLAB (R2016b). Secondly, the criterion from

the study by Dash et al., (2017) was implemented, where those parts having no intersection of the 25th and 75th percentiles between 'Infested' and 'Healthy' groups was considered as the region with significant changes.

2.6. Phenology model of bark beetles' development

The phenology model RITY-2 (Ogris, 2020; Ogris et al., 2019), which is based on daily temperatures records allows for modelling and monitoring of bark beetle development in a daily step. The model predicts the onset spring swarming, onset of infestation by filial or sister generations, final number of generations and seasonal development of *I. typographus*, To quantify the bark beetle development more precisely, degrees-days (dd) units are used, which refer to sum of temperature that exceed specific threshold. Ogris et al., 2019 refers that the total development of *I. typographus* requires a thermal sum of 557 dd (more detail in **Appendix B**), then the 9.3 %, 37%, 10.4 % and 43.3% of thermal sum is needed for egg, larva, pupal and maturation feeding, respectively. This detailed information could help to plan defence measures like deployment of pheromone traps, sanitary cuts or suitable timing for aerial surveys.

The RITY-2 had originally been developed and validated for Central European conditions in Slovenia, predicting the onset of spring swarming, onset of infestation and onset of emergency of filial beetles with a mean error of 2.4, 4.7 and 0.5 days, respectively (Ogris, 2020; Ogris et al., 2019). Some changes must be made to adapt this model to conditions in the Czech Republic, we shifted the date for calculation of
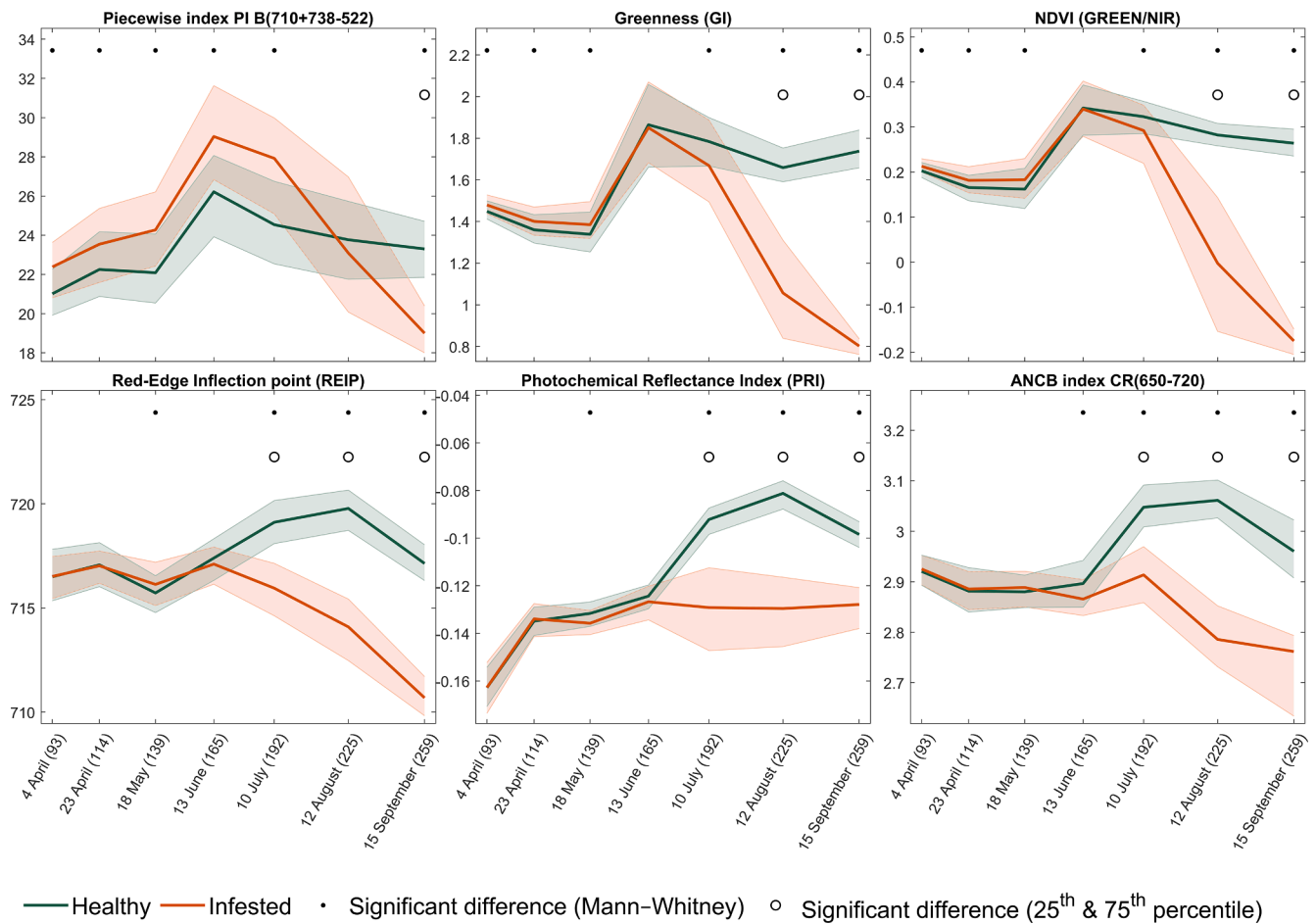
Fig. 4. Spectral indices depict separability of 'Healthy' and bark beetle 'Infested' groups. Solid lines refer to mean index values. Shaded areas depict 25th and 75th percentiles of index. The time of significant differences between groups are identified by two methods Mann-Witney test (dots) and 25th and 75th percentile (circles).

cumulative temperatures from 7 March to 1 April in conformity with another phenology model validated in the conditions of the Czech Republic (Berec et al., 2013). We used interpolated air temperature data from a regional climate model administrated by the Czech Hydrometeorological Institute providing an hourly averaged air temperature between April and December 2020. More information about model application can be found in **Appendix B**.

3. Results

3.1. Bark beetle development at the site

According to the RITY-2 model, the infestation by first filial generation started on 29 April 2020, but it was actually observed in the field later (3 May 2020). Those field observations, however, found infested uprooted trees in sun exposed places on the recent forest edges, but not yet on trees inside the monitored stand. Those trees were infested around 17 June 2020.

The bark beetle development was then simulated from 3 May 2020 forward, presenting the beetles' maximum development at the locality (Fig. 2a). On the basis of cumulative sum of effective temperature, it seems that two filial and two sister generations (Fig. 2b) were established. Captures in pheromone traps confirmed the time of first infestation and forming of the first sister generation, where thousands of beetles were caught (Fig. 2c). Owing to low frequency of captures during summer, we could not verify the timing of other generations' establishment. Fortunately, the captures in pheromone traps are of useful but

of minor importance in relation to our intention of spruce forest dieback mapping.

Fig. 2 combines airborne image acquisitions (1–7) with field survey data and phenology model. In Table 3, some events capture in Fig. 2 are translated to exact values of dates, DOYs and dd since the beginning of infestation. Some events are also related to capabilities of spectral indices to differentiate infested trees from healthy one, which is described in section 3.3 in details. The 1st and 2nd acquisitions were carried out before onset of infestation at the locality. The 3rd and 4th acquisitions were carried out after the onset of infestation at the sunlit, open forest edges of the locality but before the infestation of monitored trees inside the forest stands (which occurred on 17 June). The 5th acquisition presents the first acquisition after infestation of monitored trees and was carried out 23 days (205 dd) after infestation was detected by the field survey. This was also the first time that the hyperspectral indices distinguished the healthy and infested groups (Fig. 4). The progress of infestation was monitored on a weekly basis in the field. Strong defoliation of still–green needles from lower parts of trees was recorded 49 days (439 dd) after infestation (Fig. 2e **photo 1.**) Note the green colour on the ground caused by green needles loss. The fallen tree at centre is not related to the ongoing bark beetle infestation). The 6th data acquisition was made 56 days (536 dd) after first infestation. Defoliation is at this point becoming apparent in the orthogonal projection from a vertical plane (above an object) (RGB image in Fig. 2d). The constantly advancing defoliation has resulted in a situation where only a few branches on the top remained undefoliated. The **photo 2** in Fig. 2e was taken 65 days (637 dd) after infestation. Finally, the 7th

Table 3
Summarizing indices performance and other effects following bark beetle infestation.

Event	Date (in 2020)	Day of year (DOY)	Number of days since beginning of infestation	Degree-days (dd) since beginning of infestation
Infestation detected on standing trees by forest workers	17 June	169	0	0
Acquisition 5, Infestation detected by REIP, PRI, and ANCB$_{650-720}$	10 July	192	23	205
In-situ photo (1), defoliation of green needles started	5 August	218	49	439
Acquisition 6, Infestation detected by Greenness (GI) and NDVI (Green/ NIR)	12 August	225	56	536
In-situ photo (2), defoliation almost complete, with only top of tree still green	21 August	234	65	637
Acquisition 7, Infestation detected by Piecewise index (PI) B(710 + 738–522)	15 September	259	90	840

acquisition captured the tree in the red-attack stage, and effects of defoliation are more apparent from RGB image (above an object) Fig. 2d.

3.2. Spectral reflectance

Seven sets of airborne hyperspectral data were acquired to map the transition across the stages healthy, green-attack, and red-attack. Mean spectral values (and 25th and 75th percentiles) for healthy and infested tree categories computed for each image acquisition are shown in Fig. 3. The group of infested trees showed since the first image acquisition a slightly higher reflectance across the spectrum than did the healthy trees. This was most evident in near infrared and green peak regions. The spectral reflectance decreased in the near infrared region through time as the infestation progressed (at 6th acquisition, DOY 225). At the same time, reflectance in red to red-edge regions increased compared with healthy coniferous. This change precedes a coming red-attack stage. It seems that the area of chlorophyll absorption in the red region (maximum absorption of chlorophyll *a* and *b* at 662 nm and 642 nm, respectively) is the part in the spectrum most impacted. Separability of healthy and infested group per wavelength was tested by two statistical approaches. Statistical Man-Witney *U* test identified that the two groups are different in nearly all bands since the first acquisition. The other approach based on intersection of 25th-75th percentiles showed, that two groups could be differentiated in the red bands at the 5th acquisition (DOY 192) at earliest. There also are apparent artefacts in water absorption bands (around 825.7 nm) associated with an atmospheric correction process, especially evident at the final acquisition from 15 September (292 DOY) (Fig. 3).

3.3. Spectral indices

Separability between healthy and infested tree class for individual spectral indices is shown in Fig. 4. Based upon the results (Fig. 4), we can see that Man-Witney *U* test show significant differences between healthy and infested trees in nearly all acquisitions teams. The second criterion based on the intersection of 25th-75th percentiles showed differences between two groups for later acquisitions. Based on this second, stricter criterion PI has a lower sensitivity for detecting coniferous infestation, for the first time decoupling the two groups at last image acquisition, i.e. 90 days after infestation was found by forest workers. Another two indices, Greenness (GI) and NDVI (Green/NIR), have frequently been used in studies employing low-cost RGB cameras or multispectral sensors. They are more promising as infestation indicators, as they were able to discern the two groups for the first time at 6th acquisition, i.e. 56 days after infestation. The other three indices (i.e. REIP, PRI and ANCB$_{650-720}$), intended for hyperspectral data, provided the best results, discerning the groups for the first time at 5th acquisitions, i.e. 23 days after infestation. This is also summarized in Table 3.

4. Discussion

The objective of this study was to acquire a hyperspectral time-series mapping forest decay at individual-tree level in order to determine the sequence and timing of symptoms. The remote sensing data were combined with information from the field survey and *I. typographus* phenology model to reflect conditions during the 2020 growing season. Our results indicate that the wavelengths related to chlorophyll absorption were impacted first. The wavelengths in the near infrared region were affected next, with delay of several weeks. Other studies, too, have highlighted the chlorophyll absorption and near reflectance regions (Campbell et al., 2004; Lausch et al., 2013) or added to this the shortwave infrared (SWIR; Abdullah et al., 2019b; Bárta et al., 2021). There is no doubt that trees approaching red-attack stage are easy to recognize based upon spectral signature. Classification of healthy versus dead trees (i.e. trees at red-attack stage) achieved more than 90% accuracy in a majority of previous studies (Klouček et al., 2019; Näsi et al., 2018), while classification of healthy and newly infested trees before visual changes (i.e. trees under green-attack stage) achieved lower accuracy of 78% and 64%, respectively (Klouček et al., 2019; Lausch et al., 2013). Classification accuracy also has been affected by spatial resolution of the imagery, with higher spatial resolution data providing higher classification accuracy (Lausch et al., 2013; Näsi et al., 2018). Dash et al. (2017) suggested the optimal spatial resolution of imagery for monitoring forest health to be in the range of 1 m. In this study, we used spatial resolution of 0.5 m based upon previous experience showing that doing so allows us to monitor trees within younger age classes (i.e. 30–40 years) at individual-tree level. The detection of infested trees within pre-visual symptoms in the green-attack stage is difficult, because the advance from green-attack stage to red-attack stage occurs very quickly. Abdullah et al., (2019b) reported that for Norway spruce trees the first two phases, green-attack and red-attack, usually occur within 1 to 6 months after the initial attack. Our results showed that the red-attack stage came 90 days (840 dd) after initial infestation. Undoubtedly, the speed of forest dieback is related to thermal conditions, number of attacking beetles, and tree vigour. Hence, the time of transition between stages may vary tree to tree at the same location, as shown in Fig. 2. The trees in green-attack (i.e. 5th and 6th data acquisition) stage were first distinguished from healthy ones 23 days after being infested by indices REIP, PRI, and ANCB$_{650-720}$. The other tested indices were able to discern the two groups from 56 days (GI and NDVI [Green/NIR]) and 90 days (PI) after infestation. To explain the delay, we consider that the traditional indices calculated as ratios of NIR/VIS primarily take into consideration canopy structural changes, but they do not reflect the subtle changes in chlorophyll content (Zarco-Tejada et al., 2001). The biochemical changes of canopy induced by bark beetles' presence

definitely precede such structural changes as needles loss in the last phases of infestation. Because the indices use bands from green peak and red-edge, they were able to discern healthy and infested group earlier. In addition, spectral indices using short-wave infrared or thermal regions might be potentially useful to detect infestation even earlier than indices based solely on VIS/NIR region. Another reason why spectral indices detected infested trees later than our field survey is that frequency of field surveys was once per week, while airborne data were acquired once per month. We can assume that higher frequency of remote sensing observations could detect infested trees earlier. This hypothesis, however, would need to be thoroughly tested in a dedicated experiment, which will likely require UAV data that allow more flexible operation than aerial data.

Other obstacle in early detection of green-attack from remote sensing is that patterns of defoliation and foliar colour changes vary between trees, however, those changes often begin from the bottom and work their way upward to the treetop (as observed in this study and our earlier study of Bárta et al., (2021)). For example, in our study we could observe green treetops even 65 days after initial infestation, even as the lower parts of tree crowns were completely defoliated (see Fig. 2e, **Photo 2**). Unfortunately, the defoliated branches in the lower parts of tree are covered by green tree top during the data acquisition from the vertical plane (above the object). That makes identification in the early phases of infestation more complicated. Also, traditional field survey methods to find infested trees are dependent upon bark beetle development. The field survey is conducted more often after onset of spring swarming. The field survey presents a subjective but still reliable method for finding newly infested trees. Nevertheless, it has considerable limits, besides being time consuming and unsuitable for large areas, its success depends upon the weather. Frass on the bark is a typical, earliest trait accompanying bark beetle presence. It is easy to find during fine weather, but it may disappear after rain or heavy wind (CABI, 2021). For this reason, there is a need to focus on more robust traits for detection, and preferably ones that do not disappear over time. These are biochemical and structure related changes, but the rate of those changes after a „successful" attack of bark beetles is dependent on many different factors and should be further investigated. Significant decrease of foliar chlorophyll and nitrogen content 15–30 days from early infestation stage was reported by Abdullah et al., (2018), but Cheng et al., (2010) reported no difference in chlorophyll content, and variable differences in water content between healthy and infested trees.

Early detection is a complex problem, because it combines the dynamics of bark beetle life cycles, site conditions and vitality of trees with weather (temperature and precipitation) development on site. A complex problem requires a complex solution. We believe that a combination of forest vitality assessment through time series of multispectral satellite images (e.g., Bárta et al., 2021), with bark beetle development models to take into account daily temperature development (like RITY2 introduced here), with field observations could help to better concentrate the efforts for timing for airborne remote sensing campaigns. Only airborne (or UAV) images can currently allow for individual tree detection, which is the spatial scale desired by forest managers. Such a monitoring system will require also an automated classification approach (based on e.g. machine learning) to identify infested trees in

green and red-attack stages.

5. Conclusion

This study monitored the development of symptoms of bark beetle infestation in Norway spruce forest stands using outputs from field survey, aerial survey, and a phenology model of bark beetle development. The main objective of this study was to compare the most common method used for finding newly infested trees (i.e. field survey) with a remote sensing-based method. We conclude that detection based upon remote sensing was delayed by 23 days (205 dd) vis-à-vis infestation detected during the field survey. This is partly due to the irregularity of airborne acquisitions that were conducted roughly once per month. It also seems that the chlorophyll absorption in the red (maximum absorption of chlorophyll *a* and b at 662 nm and 642 nm, respectively) and red-edge region is the most impacted part of the spectrum. Therefore, vegetation indices related to this part of the spectrum (e.g. REIP and $ANCB_{650-720}$) and PRI were able to detect infestation earlier than were indices working with near infrared spectral information. Indices like GI and NDVI (Green/NIR) detected bark beetle presence even later, after 56 days (536 dd) from the time of being infested.

For planning of proactive forest management measures, the gap of 23 days can still be regarded as acceptable because sanitary cuts are planned within 6 weeks after infestation (i.e. the minimum time required for a new generation to be established in the local climatic conditions of the Czech Republic [Zahradník and Knížek, 2016).

A possible way to improve early detection would be to explore information also from SWIR and/or thermal regions. Airborne detection will always face difficulties with the proper timing of flights. Thus, the combination of local field surveys and phenology models can help to determine the most suitable timing for airborne sensing, and that will be helpful especially in monitoring larger areas.

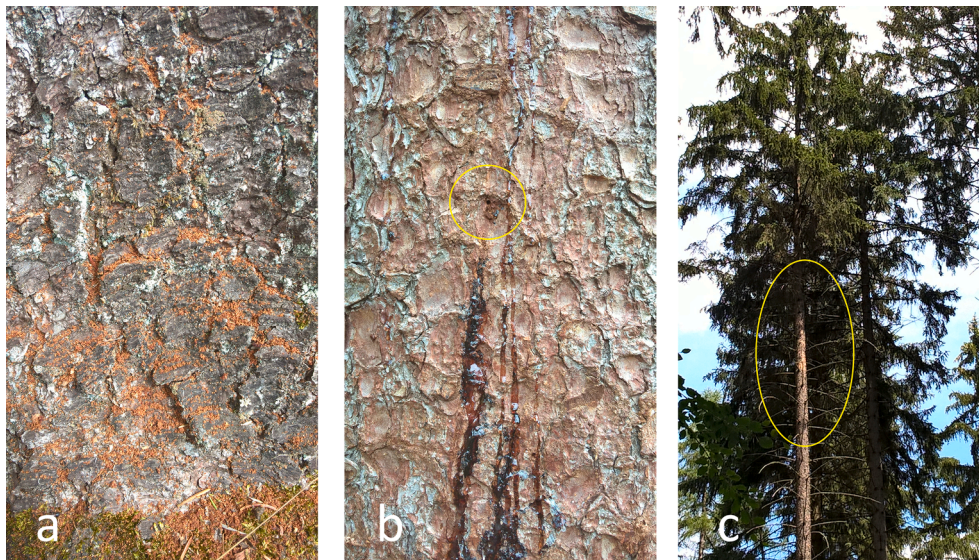### Declaration of Competing Interest

The authors declare that they have no known competing financial interests or personal relationships that could have appeared to influence the work reported in this paper.

Appendix A

Fig. A1. Symptoms of infestation. a) Frass (light-brown sawdust-like powder), b) entrance holes produced by the beetles in the lower parts of the stem, c) bark from the higher parts of the trunk is flaked off.

Appendix B

Bark beetle development is driven by temperature and day length. Air temperature must be further transformed into bark temperature (BT) such that it creates a certain temperature inside the bark (Baier et al., 2007; Ogris et al., 2019; Wermelinger, 2004).

We used (Eq. (1)) for transformation from air temperature to BT, specifically calculating *BTmean* in the RITY model (Ogris et al., 2019):

$$BTmean(x_i) = -0.48 + 1.03 \cdot T(x_i) \tag{1}$$

where T is the average air temperature at specific time x_i.

The beetles' development rate is limited also by lower ($DB_L = 8.3\,°C$) and higher ($DB_H = 38.9\,°C$) development thresholds. Beyond these limits, the development does not proceed:

$$\text{If } BT(x_i) \leq DT_L \text{ or } BT(x_i) \geq DT_U \, T_{eff}(x_i) = 0 \tag{2}$$

The effective bark temperature (BT_{eff}) between DB_L and the optimum threshold (T_O) was calculated with a linear function (Ogris, 2020):

$$\text{If } BT(x_i) > DT_L \text{ or } BT(x_i) \leq T_O \, T_{eff}(x_i) = BT(x_i) - 8.3 \tag{3}$$

A non-linear equation was used between T_O and DB_H:
If $BT(x_i) > T_O$ or $BT(x_i)(T_O - DT_L). < DT_U$

$$T_{eff}(x_i) = \times \left(e^{\alpha + T} - e^{\left(\alpha \times T_{max} - \frac{T_{max} - T}{\beta} \right)} - \gamma \right), \tag{4}$$

where $\alpha = 0.02876507$; $\beta = 3.5922336$; $\gamma = 1.24657367$; $T_{max} = 40.9958913$.

In any case, the thermal sum T_{eff} of 557 degree-days (dd) is required for complete development of *I. typographus* (Baier et al., 2007). Calculating the day of year for the onset of swarming ($YD_{swarming}$) based upon the threshold for flying activity and on cumulative daily maximum air temperatures (T_{max}) above DT_L since 1 April, the onset of swarming ($YD_{swarming}$) occurs:

$$YD_{swarming} \text{ if } T_{max} > 14.5\,°C \text{ and } \sum (T_{max} - 8.3) \geq 53.0 \, dd \tag{5}$$

In a similar way, the onset of infestation ($YD_{infestation}$) was calculated from 1 April onwards:

$$YD_{infestation} \text{ if } T_{max} > 14.5\,°C \text{ and } \sum (T_{max} - 8.3) \geq 155.6 \, dd, \tag{6}$$

where T_{max} is a daily maximum air temperature. In the original RITY model, the cumulative daily temperature needed for swarming or infestation was calculated from 7 March (Ogris, 2020). Because the RITY model was calibrated in the conditions of Slovenia, we used 1 April as the beginning for calculation of cumulative temperatures, as used in a similar phenology model (PHENIPS) validated for conditions in the Czech Republic (Berec et al., 2013).

The development of the first filial generation ($T_{sum_{F1}}$) was calculated as the sum of effective bark temperature normalized by the thermal sum required for complete development (i.e. 557 dd):
if $YD \geq YD_{infestation}$

$$T_{sum_{F1}} = \frac{\sum T_{eff}}{557} \tag{7}$$

If $T_{sum_{F1}} = 1$, the first filial generation is fully developed.

The re-emergence time is also estimated from the cumulative thermal sum for complete development, and 50% of the thermal sum for complete development (i.e. 278.5 dd) is needed for re-emergence and establishing the first sister generation (YD_{S1}) and upcoming jth generation (Baier et al., 2007; Ogris, 2020; Ogris et al., 2019):

If $YD \geq YD_{sisterbrood}$

$$YD_{S1} \text{ if } T_{sum_{F1}} > 0.5 \text{ and } T_{max} > 14.5 \text{ }^\circ C \text{ and daylength} \geq 14.5 \text{ h} \tag{8}$$

$$T_{sum_{S1}} = \frac{\sum T_{eff}}{557}$$

and,

$$YD_{Sj} \text{ if } T_{sum_{F1}} > j - 0.5 \text{ and } T_{max} > 14.5 \text{ }^\circ C \text{ and daylength} \geq 14.5 \text{ h} \tag{9}$$

$$T_{sum_{Sj}} = \frac{\sum T_{eff}}{557}$$

Onset of the second filial generation (YD_{F2}) is calculated similarly:

$$YD_{F2} \text{ if } T_{sum_{F1}} > 1 \text{ and } T_{max} > 14.5 \text{ }^\circ C \text{ and daylength} \geq 14.5 \text{ h} \tag{10}$$

$$T_{sum_{F2}} = \frac{\sum T_{eff}}{557}$$

Appendix C. Supplementary data

Supplementary data to this article can be found online at https://doi.org/10.1016/j.foreco.2021.119984.

References

Abdullah, H., Darvishzadeh, R., Skidmore, A.K., Groen, T.A., Heurich, M., 2018. European spruce bark beetle (Ips typographus, L.) green attack affects foliar reflectance and biochemical properties. Int. J. Appl. Earth Obs. Geoinf. 64, 199–209. https://doi.org/10.1016/j.jag.2017.09.009.

Abdullah, H., Skidmore, A.K., Darvishzadeh, R., Heurich, M., Pettorelli, N., Disney, M., 2019a. Sentinel-2 accurately maps green-attack stage of European spruce bark beetle (Ips typographus, L.) compared with Landsat-8. Remote Sens. Ecol. Conserv. 5 (1), 87–106. https://doi.org/10.1002/rse2.93.

Abdullah, H., Skidmore, A.K., Darvishzadeh, R., Heurich, M., 2019b. Timing of red-edge and shortwave infrared reflectance critical for early stress detection induced by bark beetle (Ips typographus, L.) attack. Int. J. Appl. Earth Obs. Geoinf. 82, 101900. https://doi.org/10.1016/j.jag.2019.101900.

Baier, P., Pennerstorfer, J., Schopf, A., 2007. PHENIPS—A comprehensive phenology model of Ips typographus (L.) (Col., Scolytinae) as a tool for hazard rating of bark beetle infestation. For. Ecol. Manage. 249 (3), 171–186. https://doi.org/10.1016/j.foreco.2007.05.020.

Bárta, V., Lukeš, P., Homolová, L., 2021. Early detection of bark beetle infestation in Norway spruce forests of Central Europe using Sentinel-2. Int. J. Appl. Earth Obs. Geoinf. 100, 102335. https://doi.org/10.1016/j.jag.2021.102335.

Berec, L., Doležal, P., Hais, M., 2013. Population dynamics of Ips typographus in the Bohemian Forest (Czech Republic): Validation of the phenology model PHENIPS and impacts of climate change. For. Ecol. Manage. 292, 1–9. https://doi.org/10.1016/j.foreco.2012.12.018.

CABI Invasive Species Compendium, 2021. Datasheet report for Ips typographus (eight-toothed bark beetle). https://www.cabi.org/isc/datasheet/28843 (Accessed: 17 July 2021).

Campbell, P.K.E., Rock, B.N., Martin, M.E., Neefus, C.D., Irons, J.R., Middleton, E.M., Albrechtova, J., 2004. Detection of initial damage in Norway spruce canopies using hyperspectral airborne data. Int. J. Remote Sens. 25 (24), 5557–5584. https://doi.org/10.1080/01431160410001726058.

Cheng, T., Rivard, B., Sánchez-Azofeifa, G.A., Feng, J., Calvo-Polanco, M., 2010. Continuous wavelet analysis for the detection of green attack damage due to mountain pine beetle infestation. Remote Sens. Environ. 114 (4), 899–910. https://doi.org/10.1016/j.rse.2009.12.005.

CZSO, 2020. Salvage felling, 100004212k211.xlsx (czso.cz), (Accessed 29 October, 2021).

Dash, J.P., Watt, M.S., Pearse, G.D., Heaphy, M., Dungey, H.S., 2017. Assessing very high resolution UAV imagery for monitoring forest health during a simulated disease outbreak. ISPRS J. Photogramm. Remote Sens. 131, 1–14. https://doi.org/10.1016/j.isprsjprs.2017.07.007.

Fassnacht, F.E., Latifi, H., Ghosh, A., Joshi, P.K., Koch, B., 2014. Assessing the potential of hyperspectral imagery to map bark beetle-induced tree mortality. Remote Sens. Environ. 140, 533–548. https://doi.org/10.1016/j.rse.2013.09.014.

Fernandez-Carrillo, A., Patočka, Z., Dobrovolný, L., Franco-Nieto, A., Revilla-Romero, B., 2020. Monitoring Bark Beetle Forest Damage in Central Europe. A Remote Sensing Approach Validated with Field Data. Remote Sensing 12 (21), 3634. https://doi.org/10.3390/rs12213634.

Gitelson, A.A., Merzlyak, M.N., 1997. Remote estimation of chlorophyll content in higher plant leaves. Int. J. Remote Sens. 18 (12), 2691–2697. https://doi.org/10.1080/014311697217558.

Hanuš, J., Fabiánek, T., Fajmon, L., 2016. *Potential of airborne imaging spectroscopy at CzechGlobe. 2016-January*, 15–17. Scopus. https://doi.org/10.5194/isprsarchives-XLI-B1-15-2016.

Herrmann, I., Pimstein, A., Karnieli, A., Cohen, Y., Alchanatis, V., Bonfil, D.J., 2011. LAI assessment of wheat and potato crops by VENμS and Sentinel-2 bands. Remote Sens. Environ. 115 (8), 2141–2151. https://doi.org/10.1016/j.rse.2011.04.018.

Jakoby, O., Lischke, H., Wermelinger, B., 2019. Climate change alters elevational phenology patterns of the European spruce bark beetle (Ips typographus). Glob. Change Biol. 25 (12), 4048–4063. https://doi.org/10.1111/gcb.14766.

Jeger, M., Bragard, C., Caffier, D., Candresse, T., Chatzivassiliou, E., Dehnen-Schmutz, K., Gilioli, G., Jaques Miret, J.A., MacLeod, A., Navajas Navarro, M., Niere, B., Parnell, S., Potting, R., Rafoss, T., Rossi, V., Urek, G., Van Bruggen, A., Van der Werf, W., West, J., Winter, S., Kertész, V., Aukhojee, M., Grégoire, J.-C., 2017. Pest categorisation of Ips typographus. EFSA J. 15 (7) https://doi.org/10.2903/j.efsa.2017.4881.

Klouček, T., Komárek, J., Surový, P., Hrach, K., Janata, P., Vašíček, B., 2019. The Use of UAV Mounted Sensors for Precise Detection of Bark Beetle Infestation. Remote Sensing 11 (13), 1561. https://doi.org/10.3390/rs11131561.

Lausch, A., Heurich, M., Gordalla, D., Dobner, H.-J., Gwillym-Margianto, S., Salbach, C., 2013. Forecasting potential bark beetle outbreaks based on spruce forest vitality using hyperspectral remote-sensing techniques at different scales. For. Ecol. Manage. 308, 76–89. https://doi.org/10.1016/j.foreco.2013.07.043.

le Maire, G., François, C., Dufrêne, E., 2004. Towards universal broad leaf chlorophyll indices using PROSPECT simulated database and hyperspectral reflectance measurements. Remote Sens. Environ. 89 (1), 1–28. https://doi.org/10.1016/j.rse.2003.09.004.

Malenovský, Z., Homolová, L., Zurita-Milla, R., Lukeš, P., Kaplan, V., Hanuš, J., Gastellu-Etchegorry, J.-P., Schaepman, M.E., 2013. Retrieval of spruce leaf chlorophyll content from airborne image data using continuum removal and radiative transfer. Remote Sens. Environ. 131, 85–102. https://doi.org/10.1016/j.rse.2012.12.015.

Näsi, R., Honkavaara, E., Blomqvist, M., Lyytikäinen-Saarenmaa, P., Hakala, T., Viljanen, N., Kantola, T., Holopainen, M., 2018. Remote sensing of bark beetle damage in urban forests at individual tree level using a novel hyperspectral camera from UAV and aircraft. Urban For. Urban Greening 30, 72–83. https://doi.org/10.1016/j.ufug.2018.01.010.

Näsi, R., Honkavaara, E., Lyytikäinen-Saarenmaa, P., Blomqvist, M., Litkey, P., Hakala, T., Viljanen, N., Kantola, T., Tanhuanpää, T., Holopainen, M., 2015. Using UAV-Based Photogrammetry and Hyperspectral Imaging for Mapping Bark Beetle Damage at Tree-Level. Remote Sensing 7 (11), 15467–15493. https://doi.org/10.3390/rs71115467.

Ogris, N., 2020. Calculation procedure for RITY—A phenology model of Ips typographus. MethodsX 7, 100845. https://doi.org/10.1016/j.mex.2020.100845.

Ogris, N., Ferlan, M., Hauptman, T., Pavlin, R., Kavčič, A., Jurc, M., de Groot, M., 2019. RITY – a phenology model of Ips typographus as a tool for optimization of its monitoring. Ecol. Model. 410, 108775. https://doi.org/10.1016/j.ecolmodel.2019.108775.

Rouault, G., Candau, J.-N., Lieutier, F., Nageleisen, L.-M., Martin, J.-C., Warzée, N., 2006. Effects of drought and heat on forest insect populations in relation to the 2003 drought in Western Europe. Ann. Forest Sci. 63 (6), 613–624. https://doi.org/10.1051/forest:2006044.

Senf, C., Seidl, R., Hostert, P., 2017. Remote sensing of forest insect disturbances: current state and future directions. Int. J. Appl. Earth Obs. Geoinf. 60, 49–60. https://doi.org/10.1016/j.jag.2017.04.004.

Wermelinger, B., 2004. Ecology and management of the spruce bark beetle Ips typographus—A review of recent research. For. Ecol. Manage. 202 (1), 67–82. https://doi.org/10.1016/j.foreco.2004.07.018.

Wulder, M.A., Dymond, C.C., White, J.C., Leckie, D.G., Carroll, A.L., 2006. Surveying mountain pine beetle damage of forests: A review of remote sensing opportunities. For. Ecol. Manage. 221 (1–3), 27–41. https://doi.org/10.1016/j.foreco.2005.09.021.

, 2016Zahradník and Knížek, 2016. Lesní ochranná služba -Lýkožrouti na smrku a sucho. 2016 LOS-letak SM-a-sucho.pdf (vulhm.cz) (Accessed: 17 Julе 2021).

Zarco-Tejada, P.J., Miller, J.R., Noland, T.L., Mohammed, G.H., Sampson, P.H., 2001. Scaling-up and model inversion methods with narrowband optical indices for chlorophyll content estimation in closed forest canopies with hyperspectral data. IEEE Trans. Geosci. Remote Sens. 39 (7), 1491–1507. https://doi.org/10.1109/36.934080.

Zhang, N., Zhang, X., Yang, G., Zhu, C., Huo, L., Feng, H., 2018. Assessment of defoliation during the Dendrolimus tabulaeformis Tsai et Liu disaster outbreak using UAV-based hyperspectral images. Remote Sens. Environ. 217, 323–339. https://doi.org/10.1016/j.rse.2018.08.024.

Appendix 3

Article 3

The use of hyperspectral remote sensing for mapping the age composition of forest stands

O. Skoupý[1], L. Zejdová[1], J. Hanuš[2]

[1]*Department of Geoinformation Technologies, Faculty of Forestry and Wood Technology, Mendel University in Brno, Brno, Czech Republic*

[2]*Global Change Research Centre AS CR, Brno, Czech Republic*

ABSTRACT: The paper deals with the issue of mapping the age composition of stand groups using hyperspectral imagery acquired by the AISA Eagle VNIR sensor in the Bílý Kříž locality in the Moravian-Silesian Beskids Mts. An object-oriented approach was employed through segmentation and subsequent classification by means of Nearest Neighbour (NN) algorithm in the environment of eCognition Developer 8 and artificial neural network (ANN) classification provided by ENVI 4.7 software. Because of the dominant occurrence of Norway spruce (*Picea abies* [L.] Karst.) monocultures in the studied locality the work focuses primarily on the distinguishability of two selected age classes of Norway spruce (10–20 years and 70–80 years). It studies possibilities of a more detailed age estimation of stand groups aged from 10 to 80 years based on the classification into the boundary classes, which shows similarity to dithering based on random algorithm. Comparison with the outline map of the Forest Management Plan shows a correlation ($r^2 = 0.83$) between the spectral characteristics of Norway spruce stands and their age composition.

Keywords: age classification; forestry; hyperspectral; object oriented; segmentation; spruce

At present remote sensing of the Earth is one of the most rapidly developing methods dealing with the mapping of the Earth's surface. Its advantage consists in the rapid acquisition and subsequent processing of data, which facilitates a nearly instant creation of up-to-date maps of extensive areas. With advance of time and with the progressing specialization of use, remote sensing of the Earth and aerial photogrammetry proceed towards increased resolution – both spatial and spectral (Elachi, van Zyl 2006). Thus, another technical branch of remote sensing has been emerging in the last three decennia, which is referred to as aerial and satellite spectrometry (Goetz 2009). It is coming to existence was motivated by the presumption of an improved identification of particular spectral attributes of individual materials through the more detailed sensing and mapping of the spectral reflectance curve (Wulder et al. 2003). This expectation was supported by results of geological applications mapping the mineral composition (Van Der Meer, 1994) and in the case of forestry by the ascertainment of the specific spectral features of canopy chemistry (Zagolski et al. 1996; Martin, Aber 1997).

At present, the centre of research into the employment of imaging spectrometry focused on forestry consists in ecological applications (Rautiainen et al. 2010). The research relies primarily on the physical approach and on quantitative analyses (Malenovský et al. 2009; Lukeš et al. 2010), which make it possible to explore the condition of studied stands through the contents of substances on the basis of radiative transfer models. Regard-

ing the exigency of the quantitative approach, the practical broader applicability of hyperspectral aerial images is currently confined rather to qualitative analyses, namely to the classification of the species composition of forest stands based on the empirical approach, particularly through comparing signatures of individual pixels of the image with libraries proposed by Clark (2003). With respect to the problematic calibration of data and absence of distinct spectral attributes of individual woody plants, the most reliable source of libraries for the application of this procedure in forestry can be seen in training sets obtained from the *in situ* measurements.

This paper will focus on the practical applicability of imaging spectrometry for quantitative analyses and will suggest an effective and easy-to-replicate methodology, which makes use of tools commonly available in the field of aerial imagery processing. In particular, it will deal with the classification of the species and age composition of forest stands, and in the case of Norway spruce also with the quantification of age value based on the mutual proportion of classified objects occurring in the studied territory with considering the classification as random dithering. Thus acquired data may be in principle subsequently applied a reverse procedure (Discepoli, Gerace 2004) and more detailed age values can be retroactively interpolated. On the grounds of empirical approach, the work aims to demonstrate dependence between the species and age compositions of stands and their spectral characteristics.

Hyperspectral remote sensing and the species and age classification of forest stands

The first attempt at an identification of tree species based on leaf contents of nitrogen and lignin was that by Wessman et al. (1988). A more recent practical application of the hyperspectral approach, in this case for mapping the species composition of coniferous tree species, was by Gong et al. (1997). Pu (2009) studied the mapping of forest stands species composition also for the broadleaved tree species. In his works, the author makes use namely of linear discriminant analysis (LDA) and neural network analysis (NNA) in which he achieves the accuracy of classification above 80%. Distinguishability of tree species even within the same genus was demonstrated van Aardt and Wynne (2007), who discerned individual *Pinus* species with a relatively high reliability.

The increasing resolution of hyperspectral data in the last decade has led to efforts for the implementation of an object-oriented approach and mapping at the level of crowns. In their work concerning the classification of rainforest species composition with using 30 spectral bands and the object-oriented approach, Clark et al. (2005) reached the total accuracy of 86%. The classification of objects representing the crowns of individual trees must be preceded by image masking and segmentation. Among researchers dealing with the issue are e.g. Brandtberg and Walter (1998), Culvenor (2002) or Bunting and Lucas (2006).

Buddenbaum et al. (2005) studied the age composition classification of coniferous stands in the western part of Germany for which they used a combination of spectral and textural characteristics. Applying hyperspectral data only, they achieved the 66% accuracy of classification using Spectral angle mapper (SAM) and Maximum likelihood (MLE) classifiers.

The question of quantifying the stand age value is disputable especially with regard to the fact that the most of the vegetation cover spectral response is provided by foliage, which is logically younger than the age of individual trees. Their age is difficult to ascertain even by non-invasive ground methods (Franklin 2001). The direct correlation between the stand age and the spectral response established by remote sensing approximates the classical "nonsense" correlation (De Wulf et al. 1990). Cohen et al. (1995) found out a dissimilar spectral response of broad age classes, which however resulted rather from different structure that showed in different illumination, absorption and shadows corresponding to different size and density of trees (Gemmell 1995). In very young and homogeneous stands, we can find a strong dependence between age and reflectance scanned by Landscat TM (Fiorella, Ripple 1993). Considering a higher spatial and spectral resolution of data in this work, which makes it possible to eliminate to a certain extent most of the above-mentioned factors by means of masking and object-oriented approach, we get closer to answering the question whether it is possible to determine the age of stands on the basis of the reflectance of individual tree crowns, in this case the age of spruce stands covered by the available imagery. One way or another, it is necessary to bear in mind that the non-invasive direct measurement of the age value is impossible; what we can measure are manifestations that are its consequence (Cohen et al. 1995) and may be unique for each locality like for example the history of stress.

MATERIAL AND METHODS

The basic material used was an archive aerial hyperspectral image acquired in 2006 in the Bílý Kříž locality in the Moravian-Silesian Beskids. Data covering an area of ca 2 km² were taken by the AISA Eagle sensor at a resolution of 0.4 m on 14 September 2006 – altogether 65 bands within a spectral range of ca 400–1,000 nm. Geometric and atmospheric corrections of the images have been performed by experts from the Institute of System Biology and Ecology ASCR.

The locality lies within approx. coordinates 18°54'E, 49°50'N at an altitude of 750–950 m a.s.l. The mean annual air temperature is 5.5°C and the mean annual precipitation amount ranges from 1,000 to 1,400 mm. Snow cover persists at the highest elevations for 160 days in the year.

The area is characterized by pure stands of Norway spruce (*Picea abies* [L.] Karst.) with admixed broadleaves; most often represented is European beech (*Fagus sylvatica*), less abundant is goat willow (*Salix caprea*), silver birch (*Betula pendula*) and individually occurring is also the silver fir (*Abies alba*) (Urban et al. 2007).

Ground measurements by the GPS apparatus consisting of the instrument Model Trimble Geo-Explorer Geo XT with the Trimble Tornado antenna were made in the locality on 22 September 2010. The ground campaign served to collect data by means of points and polygons for the determination of training sets. The collection of data covered continuous even-aged Norway spruce stands and solitary broadleaves. The time lag between the acquisition of hyperspectral image and the ground measurement has been taken into consideration when estimating stand ages during the field measurement, where four years were automatically subtracted from estimated ages.

Groundwork for the evaluation of age class classification accuracy was chosen to be an outline map of the Forest Management Plan (FMP) 2008 available on the WMS server operated by the Forest Management Institute (ÚHÚL Brandýs nad Labem). Vectorization of lines was followed by the creation of a polygonal map featuring the layout of stand groups in the studied locality with the values of their age classes.

Software used includes namely the ENVI 4.7 programme for masking and classification by means of artificial neural networks, eCognition Developer 8 for segmentation and classification by means of Nearest Neighbour algorithm and ArcGis 10 for the preparation of the FMP out-line map, necessary modifications of layers and visualization.

Masking of non-vegetation pixels

Based on the high resolution of the obtained images, we proceeded to the object-oriented approach and to the supervised classification. The first step in data processing was a reduction of the number of bands and masking out of noise pixels. Regarding the low image signal/noise ratio, six bands in the shortest wavelengths (392–435 nm) where the spectral response of the vegetation was weakest had to be eliminated from the classification and the selection for the classification included only the pixels whose reflectance curve was not distorted by noise. These were chiefly the pixels that were automatically assigned pre-adjusted values in the visible range of electromagnetic spectrum (0.25% reflectance in the area of blue and red bands, 0.50% reflectance in the area of green bands).

The subsequent image segmentation into the crown level of individual trees refrains from the traditional procedure (Brandtberg 1998) using the image smoothing in the first step. Instead of the elimination of noise pixels and reduction of data volume the procedure used was based on the following hypothesis:

Considering the character of vegetation cover insolation, the purest signal with the highest reflectance values can be expected on the tops of tree crowns. Thus, each individual represents a local maximum, which is surrounded by pixels of lower reflectance (non-insolated and shaded parts of crowns) and often also by a mixed signal (canopy gaps where the foliage of two or more individuals reaches into one pixel). If an adequate threshold value of minimum reflectance is established and all pixels not reaching the value in selected bands are masked out, it is possible to create an image that will contain only clusters of pixels representing crown tops of individual trees.

Supposed benefits of this approach are as follows: material reduction in the volume of processed data and masking out most of mixed pixels. Classification is made only on pixels with the strongest and cleanest signal. Another benefit is markedly simplified and advanced segmentation.

Because only the pixels on insolated crown parts directly enter the classification, the problem of different results on insolated and non-insolated slopes is largely resolved in spite of the fact that the crowns of trees on the reverse slopes will be rep-

resented by smaller clusters in the image than the crowns of similarly grown-up trees on the forward slopes. The threshold value should therefore be chosen also in dependence on the elevation angle of the sun at the time of sensing and on the maximum gradient of slopes with the opposite exposure.

Based on the assessment of multiple results, the threshold value for masking was selected to be 1% over bands from 444 nm to 498 nm. Each pixel that did not reach the value in any of the bands was masked out.

The following step was the application of another mask to reduce the volume of processed data. This time, it was on the basis of a vegetation index in order to eliminate all non-vegetation pixels that would not be used in the classification focused on the species and age composition of stands. The Normalized Difference Vegetation Index (NDVI) was selected. The threshold value was chosen to be 0.8, at which a maximum of pixels not belonging to forest areas (except for grass stands and shrubs) was eliminated with no simultaneous essential loss of data in the stands. The resulting raster delimited the individual crowns satisfactorily (the ideal state of isolated pixel clusters was achieved especially in Norway spruce stands over 70 years – see Fig. 1) without the tree tops on the reverse slopes having been masked out. More continuous clusters of pixels representing multiple crowns were formed chiefly on insolated slopes, in younger stands, in groups of individual broadleaves with a continuous canopy and particularly in marginal individuals.
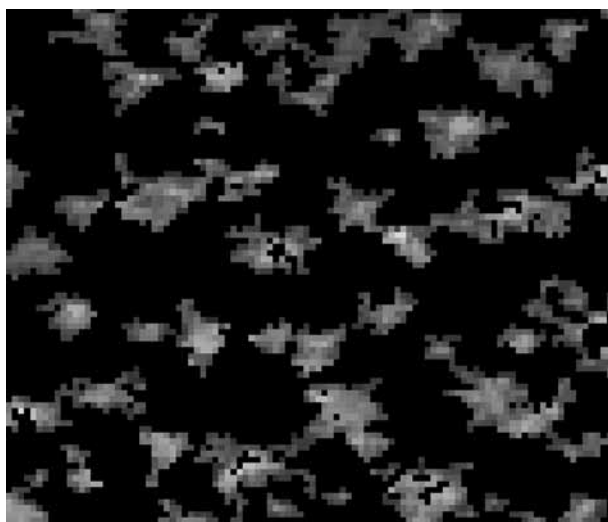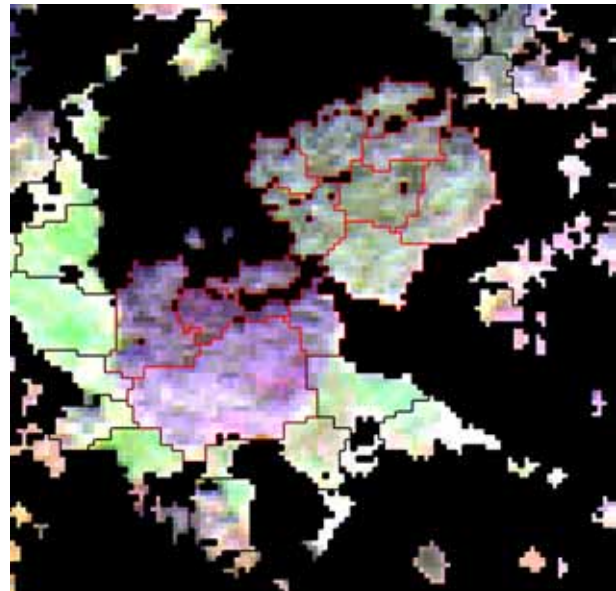

Fig. 2. Example of the segmentation result on two broadleaved trees that have also been selected as control sets for Class BS

Image segmentation into the level of individual crowns

After masking out pixels non-utilizable for the classification, we proceeded to the image segmentation. We selected multilevel (multiresolution) segmentation on the basis of one layer (444 nm) that showed the best prerequisites for successful segmentation even in the case of linked clusters representing individual tree tops (most contrasted transitions) between individual crowns. The scale parameter (Baatz et al. 2004) was adjusted at 20. Parameters for shape and compactness were adjusted on the basis of a presumption that within a great amount of weakly associated pixel clusters representing the individual tree crowns, the crowns themselves will be plotted exactly as the largest possible compact pixel clusters in the image with minimum regard of spectral characteristics. This is why the compactness parameter ensuring the roundness of resulting shapes was assigned the maximal value possible (1.0) and the shape parameter which determines how much the shape characteristics will be favoured over spectral properties was set up at 0.8. The resulting objects meet the required results to a maximum possible extent. As to bulky crowns, namely in broadleaved trees (classified as BS), one crown is often covered by several objects (see Fig. 2). Nevertheless, a general rule applies that the accuracy of segmentation increases with the increasing age of the stands, i.e. with more open canopy and lower interconnection of individ-
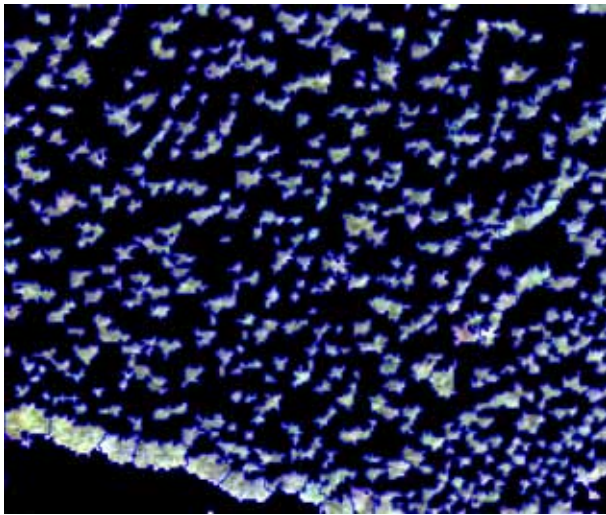

Fig. 1. Results of masking out unused pixels on the basis of reflectance and NDVI in a Norway spruce stand aged 70 to 80 years

Fig. 3. Example of the segmentation result in a Norway spruce stand aged 20–30 years

Fig. 4. Segmented image, individual pixels are assigned the average reflectance values of the respective objects

ual clusters, and the result approximates an ideal condition when the number of clusters roughly corresponds to the number of individuals. An example of the segmentation result in a stand aged 20–30 years is presented in Fig. 3.

The following step was the elimination of inadequately small-sized objects in which mean reflectance values for individual bands were calculated from a low amount of pixels, and which could therefore be loaded with error that had a potential to negatively affect the resulting classification especially in cases when such objects were parts of training sets. For these reasons, all objects represented by less than 5 pixels (0.8 m^2) were excluded from further processing. The segmented image was exported in the raster format and the table of attributes for each object contained the mean values of objects in individual bands. This vector set was used to create 59 raster layers, which were sequenced to give a new hyperspectral image. An advantage of the new image is that it represents a combination of the object-oriented and per-pixel approach to classification when all pixels belonging to one object are always going to be allocated to the same class. Part of the segmented image where each pixel of an object is assigned its respective mean value can be seen in Fig. 4.

Segmented image classification using the NN algorithm

The test classification whose basic parameters (training and testing sets) were subsequently used also in the classification by means of neural net-
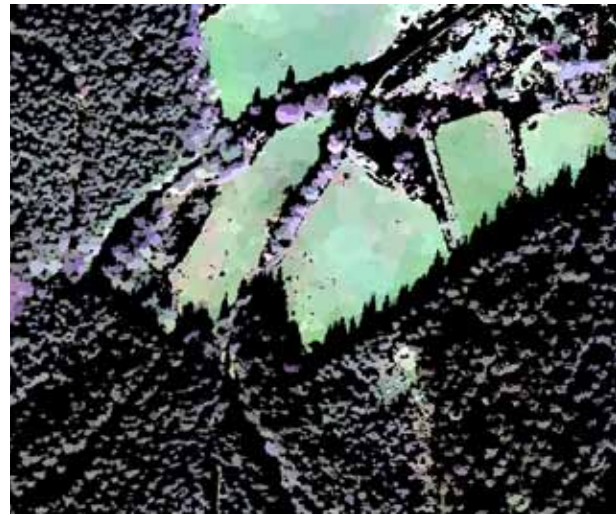
works in the ENVI 4.7 environment was conducted in the environment of eCognition Developer 8 software. Regarding the low representation of broadleaved species in the stands and their diversity, it was impossible to obtain a sufficient amount of training and control sets for individual species so that the result would be statistically significant. This is why all broadleaved trees were classified into one class BS (broadleaved species). Other two classes include Norway spruce stands of two age classes (in our case, age classes denote decennial intervals of stand age): second age class (10 to
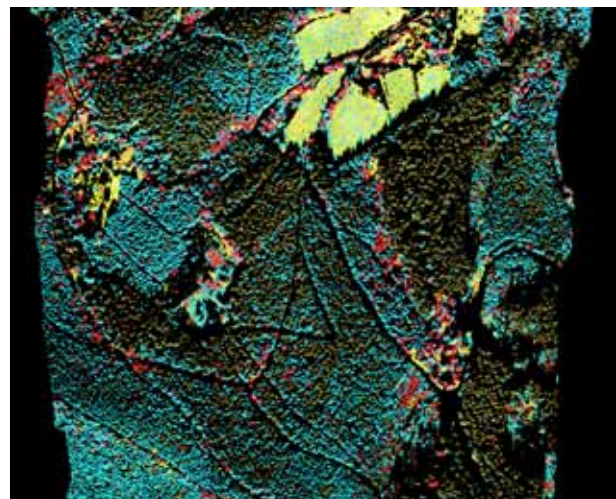

Fig. 5. Results of the NN classification in the programme eCognition Developer 8 on a part of the studied area. Cyan and brown are objects classified in SSY and SSO classes. See the gradual change in the proportion of SSY and SSO objects occurring in the locality in dependence on the age of spruce stands. Red and yellow are objects in classes BS and OS, respectively

20 years) and eighth age class (70–80 years). For these two classes we chose working names SSY (young spruce stand) and SSO (old spruce stand). Other conifers in the locality were neglected due to their very scarce occurrence. All other surfaces not belonging to forest stands (namely permanent grass stands) were classified in the last class OS (other surfaces). The reason for specifying two classes of spruce stands was our effort to find out whether the age class of the given group of stands can be estimated on the basis of the mutual ratio of SSY and SSO objects occurring on individual plots. With respect to the similarity of spectral reflectance curves in the spruce stands of different age classes, we expected that with the increasing age, the proportion between the number of objects classified in SSY and SSO classes would be gradually changing from young stands with the dominant SSY class to old stands with the dominant SSO class.

Training sets for the SSY and SSO classes were determined on the basis of *in situ* surveyed polygons delimiting continuous even-aged spruce stands without admixed broadleaves. Within a surveyed polygon, all objects were selected that were included in the training set of a particular class. Training sets of Class BS consist of individual broadleaved trees surveyed by the GPS point measurement. Using these coordinates, single objects representing the respective crowns were collected in the image and were subsequently denoted as training sets. With respect to their distinguishability by eye, training sets of Class OS were determined only by comparison with the orthophotomap. A similar method was used to select the objects of the control sets. When the training sets had been determined, it was possible to proceed to the proper classification based on the nearest neighbour algorithm. The classification was calculated from mean reflectance values of individual objects in all 59 bands in the range from 444 to 982 nm. Classification accuracy was evaluated through the calculation of error matrix based on the agreement of the object classification with the control sets. An example of the classification results can be seen in Fig. 5.

Image classification using the artificial neural networks (ANN)

As an alternative comparison method of classification we chose the application of an artificial neural network (ANN) in the ENVI 4.7 programme. The reason for its implementation was expected greater flexibility than in other offered classifiers

considering the fact that the classification was not targeted at the recognition of particular spectral attributes. Training and control sets used in this method were identical to those in the classification using the NN algorithm.

The classification was carried out by applying a layered feed-forward perceptron artificial neural network. Several network trainings were performed in search of optimal parameters. The best results were reached when the sigmoidal (logistic) activation function of neurons with the threshold value (Training Threshold Contribution) was selected to be 0.9, the training momentum was adjusted at 0.9, the training rate was set up as 0.05 and the total number of iterations was adjusted at 500 (RSI 2004). With these values, the network error (RMS error) gradually converged to 0.13.

Quantification of age values

The tool selected for the evaluation of achieved accuracy in the classification of the age classes of spruce stands was a comparison with data in the FMP 2008 outline map from which a map of age classes for individual groups of stands was created.

The accuracy of determination of the age composition of spruce stands was checked on the basis of a normalized index. A prerequisite for the establishment of the index is an attempt at the additional quantification of the variable of age based on a qualitative analysis. The result of classification shows characteristics similar to dithering based on the random algorithm as described in Velho et al. (2009), which is in this case seeded largely by noise in the image data and by the error of the classification itself. Thus, in the case of assumed unambiguous distinguishability of young and old spruce stands, the classification into the two classes would lose the characteristic of thresholding and the original values above which the classification into the limit classes was made can be retroactively estimated based on the law of large numbers. The prerequisite is however a sufficient number of objects on the surveyed surface, in our case extensive groups of stands.

In order to compare the age index with actual values, a vector map was created of age classes acquired from the FMP outline map. It was subsequently converted into the raster format (at a resolution of 0.4 m, corresponding to the resolution of the classified data) and a table was generated using the Combine tool, which recorded the number of pixels allocated to the respective classes occurring
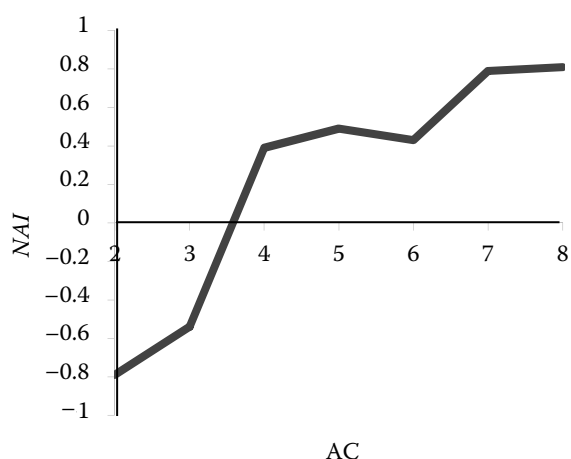
Fig. 6. Relation between the value of Normalized Age Index (*NAI*) obtained from the classification and the age class designation (AC) obtained from the FMP outline map

on all plots falling in a certain age class (according to the FMP outline map).

Subsequently, a calculation was made of normalized indices for age classes (AC) 2–8 from the following equation:

$$NAI_n = \frac{A_n - B_n}{A_n + B_n}$$

where:

NAI_n – the index calculated for groups of stands classified in the nth age class,

A_n – the total number of pixels classified as SSO on all plots mensurated as class *n*,

B_n – the analogical value for all pixels classified as SSY.

The obtained indices were edited in tabular form and converted into graphs. Based on the table, a correlation coefficient was calculated between the mensurated age of the groups of stands obtained from the FMP map and the value gained from the *NAI* index calculation. The final step to visualize the estimated age of the individual groups of stands consisted in the creation of a map where *NAI* was calculated for each group of stands based on the proportion of areas classified in SSY and SSO classes. Age class (AC) values of individual groups of stands were estimated from the obtained *NAI* on the basis of linear regression.

RESULTS

Based on the comparison of classification results with the control sets, aggregate classification accuracies were established for the NN (0.88) and ANN (0.92) classifiers – see Tables 1 and 2. It was shown that as compared with the control sets and after the error matrix calculation, the method of classification provided more accurate results using ANN in the ENVI 4.7 software compared to the NN classification in the eCognition Developer 8 environment. However, both methods of classification introduced a relatively high omission error of BS class. At the same time it was demonstrated that older Norway spruce individuals were classified in the SSY class more frequently than younger individuals in the SSO class. The correlation coefficient between the area-weighted average of normalized

Table 1. Error matrix of classification by the NN method (units are objects)

User class\Sample	BS	SSY	SSO	OS	Sum
BS	60	28	7	8	103
SSY	4	767	70	6	847
SSO	1	119	711	0	831
OS	2	7	1	351	361
Unclassified	0	0	0	4	4
Sum	67	921	789	369	2,146
Producer	0.90	0.83	0.90	0.95	
User	0.58	0.91	0.86	0.97	
Overall Accuracy	0.88				
KIA	0.82				

BS – broadleaved species, SSY – young spruce stand, SSO – old spruce stand, OS – other surfaces, KIA – Kappa index of agreement

Table 2. Error matrix of classification by the ANN method (units are pixels)

User class\Sample	BS	SSY	SSO	OS	Sum
BS	9,295	2,093	342	1,587	13,317
SSY	448	52,792	1,819	318	55,377
SSO	60	2,103	31,888	0	34,051
OS	0	504	0	66,712	67,216
Unclassified	0	0	0	197	197
Sum	9,803	57,492	34,049	68,814	170,158
Producer	94.82	91.82	93.65	96.95	
User	69.80	95.33	93.65	99.25	
Overall Accuracy	0.92				
KIA	0.94				

BS – broadleaved species, SSY – young spruce stand, SSO – old spruce stand, OS – other surfaces, KIA – Kappa index of agreement

Table 3. Area-weighted average and dispersion of calculated *NAI* values for stands of the same age class (AC) according to the FMP outline map

AC	*NAI*	Dispersion
2	−0.79	0.06
3	−0.54	0.29
4	0.39	0.03
5	0.49	0.04
6	0.43	0.07
7	0.79	0.02
8	0.81	0.01

age index values calculated for all plots of the given age class (AC) and the values from the FMP outline map is 0.91 ($r^2 = 0.83$). The highest variance in calculated *NAI* occurs at the 3rd age class (20–30 years) and equals 0.29. The relation between *NAI* values calculated from the classification results by ANN and age classes obtained from the FMP outline map is illustrated in Fig 6, numerical values along with dispersion in *NAI* calculation for the respective age classes can be found in Table 3. If a simple linear dependence between age and spectral response is presumed, the area-weighted average of deviations between the stand age class value and the stand age class estimated from *NAI* equals 0.98. The highest deviations occur at intermediate age classes, where the age value is systematically underestimated (the maximal weighted average of deviations occurs in the 4th age class and equals 2.18, i.e. 21.8 years). The AC values estimated from the calculated *NAI* and AC values harvested from the FMP outline map can be compared in Fig. 7.
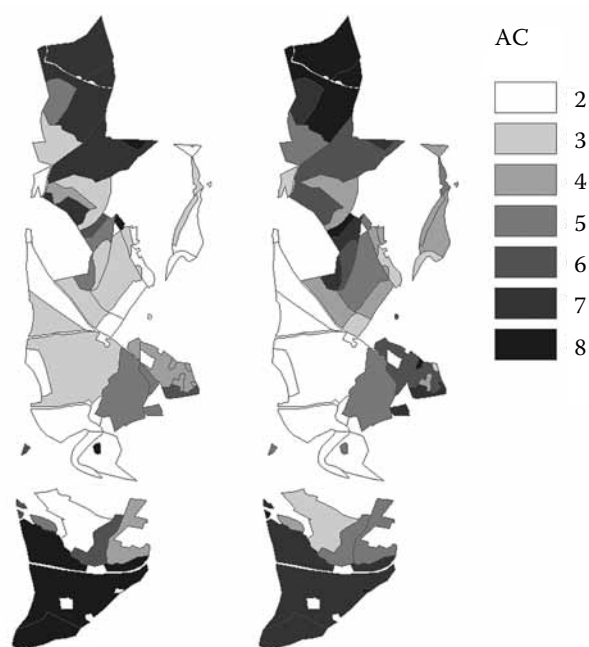

Fig. 7. Comparison of AC values obtained from the FMP outline map (left) with AC values estimated using *NAI* (right)

DISCUSSION

The two employed methods of classification demonstrated that the age of spruce stands can be distinguished on the basis of spectral characteristics. The result may be partly due to different spectral characteristics of crowns and partly due to some other factors such as the decreasing visibility of unshaded undergrowth with the increasing age (Franklin 2001). The comparison of results suggests that ANN can be recommended as a more suitable classifier than NN even though the data conversion is laborious because the compatibility

between the employed types of software is low. This can possibly be avoided for example by the use of the ENVI Feature Extraction Module instead of the eCognition. Acquiring and testing the module for the segmentation purposes may be suggested as a subject for future work. The relatively large omission error in the case of BS class in both classifications was likely to have resulted from the uneven interspersion of broadleaved species particularly into the young spruce stands and their inclusion in training and control sets. Taking into account the distribution of SSY and SSO objects on the plots of intermediate age classes, ANN approximates thresholding more than NN, which corresponds to its higher accuracy provided that the age of stands, i.e. concomitant phenomena accompanying the ageing of stands, can be discerned (Franklin 2001).

The result of the classification by means of artificial neural networks suggests that the gradient of the change in stand spectral characteristics decreases with the increasing age of the stands with the greatest changes being observed to occur ca between the 3rd and 4th age class. Looking at Fig. 1 we can see that in plots mensurated in the sixth age class, this trend is disturbed, most probably due to the low amount of data and because of non-homogeneous species and age composition of stands on the concerned plots. Individual groups of stands of the third age class exhibit the greatest dispersion of the calculated *NAI*, which corresponds to the assumed nonlinear dependence between the age and spectral reflectance with the most significant changes occurring between 30 to 40 years of age. Therefore, in the case of 3rd age class groups of stands the highest deviations occur between the assumed AC estimated from *NAI* based on the simple linear regression and AC obtained from the FMP outline map. The errors relate mainly to one particular locality in which a possible FMP data error or a gross mistake of the enumeration officer can be considered with respect to stand characteristics that rather correspond to older age classes. The information in the FMP outline map itself may not correspond to actual age; the groups of stands may be reclassified into other AC according to their actual condition. At the same time, it is necessary to take into account that one age class represents a relatively wide interval of 10 years and the difference in ages as well as in the spectral response of individuals classified in the same class may thus be considerably higher than the difference in ages of individuals classified in neighbouring AC. Another factor that could be a source of errors is the two years gap between the FMP mapping and image acquisition, namely the stress history. However, due to a relatively small test-ing area and no extreme weather events occurring at the site during the relatively short period, this factor was not considered significant.

The assumption of linear dependence when estimating the age values of individual stands is not of course ideal and imposes a significant error on the estimation of results. If there is any systematic dependence between stand age and its spectral response, it should be possible to determine a function for the more accurate estimation of stand ages. However, this cannot be done for this single case on the basis of one hyperspectral image. Finding any universally applicable function would be a result of numerous applications of this methodology in various conditions. Of course, there is always a possibility to estimate the function for each particular case if the ground measurement defines training sets for each age class, but this would lead to increasing demands on the methodology thus compromising its effectiveness.

In spite of relatively optimistic results, namely when considering the dispersion in calculated *NAI*, the applicability of the methodology needs to be verified on another set of data from a different locality. Based on those data, a map will be created of the age of groups of stands that will be subsequently compared with the corresponding stand map. A successful creation of the map of age classes of the groups of stands calls for the development of a reverse tool such as image segmentation at a smaller scale where potential groups of stands can be delimited by detected breaklines and then assigned the age values calculated from the *NAI*. The applicability of this method increases with the increasing amount of distinct, mainly straight lines in the landscape matrix. Another employable tool is a convolution filter for the calculation of *NAI*, through which the age value is estimated for individual pixels of the resulting map separately. This method could be used in the case of stands with smoother transitions between larger groups of stands.

It should be noted that with respect to the low spectral diversity of neighbouring age classes, the proposed methodology cannot be used to determine the age of particular individuals. It can be employed for mapping the age composition of stands consisting of even-aged groups of stands or for estimating the average age of uneven-aged stands.

CONCLUSION

Our research implementing the object-oriented approach and site-specific supervised classification

demonstrated a high rate of correlation between the spectral characteristics of stand reflectance and stand age class in the Norway spruce groups of stands aged 10–80 years. Accuracies achieved by the Nearest Neighbour algorithm and by the use of the artificial neural networks in classifying individual Norway spruce specimens into two classes representing Age Class 2 and Age Class 8 were 86% and 96%, respectively. With the inclusion of the two remaining classes (broadleaved species and other surfaces), the classification accuracy was 88% (NN) and 92% (ANN).

The proposed methodology of object-oriented approach can be applied in the analysis of the species and age composition of forest stands under condition of the increasing availability of high-quality hyperspectral imagery of submeter resolution. Also the wider applicability of the methodology should be tested in other than pure Norway spruce stands, especially when considering the difficulties with segmentation of broadleaf stands. Even when considering just Norway spruce stands, the methodology still calls for further testing in different conditions where its validity could be confirmed. In such a case, the presumed generally applicable function of dependence of the spectral response on stand age could be then approximated to provide more accurate results.

Regarding the problematic data pre-processing and calibration, the supervised classification continues to be a method yielding the most reliable results in using imaging spectrometry for forest applications, which usually compensate for the necessity of optimizing the methodology for particular cases and ground measurement of the training sets.

References

Baatz M., Benz U., Dehghani S., Heynen M., Höltje A. (2004): eCognition Elements 4.0 User Guide. München, Definiens Imaging: 71.

Brandtberg T., Walter F. (1998): Automated delineation of individual tree crowns in high spatial resolution aerial images by multiple-scale analysis. Machine Vision and Applications, *11*: 64–73.

Buddenbaum H., Schlerf M., Hill J. (2005): Classification of coniferous tree species and age classes using hyperspectral data and geostatistical methods. International Journal of Remote Sensing, *26*: 5453–5465.

Bunting P., Lucas R. (2006): The delineation of tree crowns in Australian mixed species forests using hyperspectral Compact Airborne Spectrographic Imager (CASI) data. Remote Sensing of Environment, *101*: 230–248.

Clark R.N., Swayze G.A., Livo K.E., Kokaly R.F., Sutley S.J., Dalton J.B., McDougal R.R., Gent C.A. (2003): Imaging spectroscopy: Earth and planetary remote sensing with the USGS Tetracorder and expert systems. Journal of Geophysical Research, *108*: 1–44.

Clark M.L., Roberts D.A., Clark D.B. (2005): Hyperspectral discrimination of tropical rain forest tree species at leaf to crown scales. Remote sensing of environment, *96*: 378–398.

Cohen, W.B., Spies T.A., Fiorella M. (1995): Estimating the age and structure of forests in a multiownership landscape of western Oregon, USA. International Journal of Remote Sensing, *16*: 721–746.

Culvenor D.S. (2002): TIDA An algorithm for the delineation of tree crowns in high spatial resolution remotely sensed imagery. Computers & Geosciences, *28*: 33–44.

Discepoli M., Gerace I. (2004): Inverse dithering through IMAP estimation. In: Lagana A., Gavrilova M.L., Kumar V., Mun Y., Tan J.K, Gervasi O. (eds): Proceedings, part IV of the Computational Science and Its Applications – ICCSA 2004. Assisi, 14.–17. May 2004. London, Springer: 379–388.

De Wulf R.R., Gossens R.E., De Roover B.P., Borry F.C. (1991): Extraction of forest stand parameters from panchromatic and multispectral SPOT-1 data. International Journal of Remote Sensing, *11*: 1571–1588.

Elachi C., van Zyl J. (2006): Introduction to the Physics and Techniques of Remote Sensing. 2nd Ed. Hoboken, Wiley-Interscience: 552.

Fiorella M., Ripple W. J. (1993): Determining the successional stage of temperate coniferous forest with landsat satellite data. Photogrammetric Engineering & Remote Sensing, *59*: 239–246.

Franklin S.E. (2001): Remote Sensing for Sustainable Forest Management. Boca Raton, Lewis: 407.

Gemmell F.M. (1995): Effects of forest cover, terrain and scale on timber volume estimation with thematic mapper data in a rocky mountain site. Remote Sensing of Environment, *51*: 291–305.

Goetz A.F.H. (2009): Three decades of hyperspectral remote sensing of the Earth: A personal view. Remote Sensing of Environment, *113*(Supplement 1): 5–16.

Gong P., Pu R., Yu B. (1997): Conifer species recognition: An exploratory analysis of in situ hyperspectral data. Remote Sensing of Environment, *62*: 189–200.

Lukeš P., Malenovský Z., Kaplan V., Hanuš J., Homolová L. (2010): Estimation of Norway spruce leaf chlorophyll content from CHRIS/PROBA satellite image data. In: Lacoste-Francis H. (ed.): Proceedings of the Hyperspectral workshop 2010. Frascati, 17.–19. March 2010. Noordwijk, ESA ESRIN: 1–4.

Malenovský Z., Lukeš P., Kaplan V., Hanuš J., Homolová L. (2009): Multi-scale aproaches retrieving norway spruce leaf chlorophyll content from high spatial resolution air-/space borne spectral image data. In: Pro-

ceedings of the Workshop on the Retrieval of Geophysical Variables Using High Spatial Resolution Optical Imagery. Noordwijk, 14.–15. October 2009. Noordwijk, ESA/ESTEC: rozsah stran.

Martin M., Aber J. (1997): High spectral resolution remote sensing of forest canopy lignin, nitrogen, and ecosystem processes. Ecological Applications, 7: 431–443.

Pu R. (2009): Broadleaf species recognition with in situ hyperspectral data. International Journal of Remote Sensing, 30: 2759–2779.

Rautiainen M., Heiskanen J., Eklundh L., Mottus M., Lukeš P., Stenberg P. (2010): Ecological applications of physically based remote sensing methods. Scandinavian Journal of Forest Research. 25: 325–339.

RSI (2004): ENVI User's Guide, ENVI 4.1 September 2004 Edition. Boulder, Research Systems, Inc.: 1150

Urban O., Janouš D., Acosta M., Czerný R., Marková I., Navrátil M., Pavelka M., Pokorný R., Šprtová M., Zhang R., Špunda V., Grace J., Marek M.V. (2007): Ecophysiological controls over the net ecosystem exchange of mountain spruce stand. Comparison of the response in direct vs. diffuse solar radiation. Global Change Biology 13: 157–168.

Aardt J.A.N. Van, Wynne R.H. (2007): Examining pine spectral separability using hyperspectral data from an airborne sensor: An extension of field-based results. International Journal of Remote Sensing, 28: 431–436.

Meer F. Van der (1994): Extraction of mineral absorption features from high-spectral resolution data using non-parametric geostatistical techniques. International Journal of Remote Sensing, 15: 2193–2214.

Velho L., Frery A.C., Gomes J. (2009): Image Processing for Computer Graphics and Vision. 2nd Ed. London, Springer-Verlag: 462.

Wessman C.A., Aber J.D., Petersen D.L., Melillo J.M. (1988): Remote-sensing of canopy chemistry and nitrogen cycling in temperate forest ecosystems. Nature, 335: 154–156.

Wulder M.A., Franklin S.E. (2003): Remote Sensing of Forest Environments: Concepts and Case Studies. Boston, Kluwer Academic Publishers: 519.

Zagolski F.P., Pinel V., Romier J., Alcayde D., Fontanari J., Gastellu-Etchegorry J. P., Giordano G., Marty G., Mougin E., Joffre R. (1996): Forest canopy chemistry with high spectral resolution remote sensing. International Journal of Remote Sensing, 17: 1107–1128.

Corresponding author:
Ing. Ondřej Skoupý, Mendel University in Brno, Faculty of Forestry and Wood Technology,
Department of Geoinformation Technologies, Zemědělská 3, 613 00 Brno, Czech Republic
e-mail: xskoupy1@node.mendelu.cz

Appendix 4

Article 4

CrossMark

ORIGINAL PAPER

Spectral reflectance is a reliable water-quality estimator for small, highly turbid wetlands

Hana Vinciková · **Jan Hanuš** · **Libor Pechar**

Abstract Spectral reflectance from water surfaces was measured in small (0.01–5 km^2), turbid, eutrophic fishponds and mesotrophic quarry lakes in the Třeboň basin (South Bohemia, Czech Republic). A spectral scanner for direct field measurements from water surfaces and a hyperspectral airborne scanner were both used. The quarry lakes and fishponds differed in their spectral signature, which reflected the extent of their eutrophication. Their chlorophyll-a (chl-a) concentrations ranged from 2 to 455 µg/l^{-1}. Various algorithms were tested to best fit the relationships between reflectance patterns and the water-quality parameters used—concentration of chl-a and the total amount of suspended solids. The reflectance ratios at 714 and 650 nm gave the best estimates for chl-a concentrations, and simple reflectance at near infrared wavelengths, especially at 806 nm, gave the best predictive values for total suspended solid

evaluation ($r^2 = 0.89$). Field surface reflectance and airborne sensing measurements were well correlated; however, airborne reflectance data showed higher variability ($r^2 = 0.93$ and 0.86, respectively). The results support the validity of reflectance measurements, both field and airborne, as a rapid tool for evaluating water quality in many turbid and greatly disturbed, small water bodies.

Keywords Remote sensing · Water quality · Hyperspectral reflectance · Turbid inland waters · Chlorophyll · TSS

H. Vinciková (✉) · L. Pechar
Laboratory of Applied Ecology, Department of Landscape Management, Faculty of Agriculture, University of South Bohemia in České Budějovice, Studentská 13, 37005 České Budějovice, Czech Republic
e-mail: hanavincikova@seznam.cz

J. Hanuš
Global Change Research Centre AS CR, v.v.i., Bělidla 986/4a, 603 00 Brno, Czech Republic

L. Pechar
ENKI o.p.s., Dukelská 145, 379 01 Třeboň, Czech Republic

Introduction

The landcover of the Czech Republic contains a large number of water bodies: mostly man-made, small and shallow, turbid, eutrophic or hypertrophic. There is no possibility to monitor all of these water bodies by means of standard methods such as water sampling and analyses or spectral ground-based measurements. However, the water bodies play an important role in the landscape, so knowledge of their quality and its dynamics is of high interest.

Optically active water-quality parameters (WQPs) such as chlorophyll-a or total suspended solid concentrations (hereafter, chl-a and TSS, respectively) can be measured by means of high spectral resolution sensors (airborne or satellite). These remote sensing (RS) methods promise to be suitable for estimating

WQPs in turbid waters over a large area several times a year; including *chl-a* (Sokoletsky et al. 2011; Yacobi et al. 2011; Shi et al. 2013), prediction of phytoplankton species (Randolph et al. 2008) and their biomass (Abd-Elrahman et al. 2011), and/or TSS (Doxaran et al. 2005; Sterckx et al. 2007; Ouillon et al. 2008). Moreover, the spatial diversity within an individual water body can be evaluated and a time series can be obtained (Sudduth et al. 2005).

Productive inland waters are optically more complex (Gurlin et al. 2011) than marine waters because they contain other optically active compounds besides phytoplankton in the water column such as inorganic particles and organic non-algal seston, modifying the spectral response (Yacobi et al. 2011) and making the interpretation of the resulting reflectance spectrum more difficult. In addition, the lake bottom reflectance may contribute to the radiance (Sokoletsky et al. 2011) in shallow waters.

Despite the fact that many reflectance spectral features of inland waters have been described (e.g. Zimba and Gitelson 2006) and many empirical algorithms have been derived, RS of inland waters remain a challenge because of the highly varied trophic states and differences in seston composition as well as different climatic conditions. These algorithms are nearly always site specific, due to changes in the biophysical water characteristics based on the location, and time of the year (Liu et al. 2003). Therefore, no wide application to any water type is feasible (Shi et al. 2013), and the algorithms often require re-parameterization and calibration (Yacobi et al. 2011). Some algorithms are promising for universal use, but they still require verification for other types of water. *Chl-a* in turbid productive waters seems to be accurately estimated by means of NIR-red algorithms (Gitelson 1992; Dekker 1993; Schalles et al. 2001; Yacobi et al. 2011; Moses et al. 2012).

Many researchers are developing a simple universally applicable algorithm of *chl-a* estimation using MERIS (Moses et al. 2012) or MODIS (Gurlin et al. 2011) data. These were primarily intended for ocean monitoring, but MERIS and/or MODIS have recently been used for inland and coastal waters (Gurlin et al. 2011; Yacobi et al. 2011; Moses et al. 2012). The two- or three-band NIR-red algorithms are routinely applied to estimate *chl-a* from near-real-time satellite data from turbid waters from around the globe without the need for case-specific algorithm re-parameterization. However,

chl-a concentrations in waters investigated through MERIS or MODIS are mainly low to moderate. Therefore, further tests are needed to validate the universal applicability of these algorithms for small, turbid, inland waters. Moreover, spatial resolution of the RS sensor is crucial because it is the key factor determined by the size of the objects investigated. The relatively coarse spatial resolution of MERIS/MODIS (300 and 250/500 m, respectively) does not allow for sensing of small water bodies. Chipman et al. (2009) and Olmanson et al. (2011) also mentioned that MODIS/MERIS data are only suitable for large lakes (>1.5/2 km^2).

Other multispectral satellites such as SPOT or Landsat provide spatial resolution in tens of metres, enabling small water bodies to be monitored by these satellites. Chipman et al. (2009) and Olmanson et al. (2011) showed that all water bodies of 0.04 km^2 and larger are suitable for monitoring with this moderate resolution. However, their radiometric resolution and signal-to-noise ratio are not designed for a very low signal emanating from these waters (Arst 2003).

Hyperspectral, airborne RS seems to be more useful for successful estimation of water quality of smaller, shallow, turbid waters (below 0.04 km^2) due to its higher spectral and very high spatial resolution. Igamberdiev et al. (2011) used this RS method, even for waters smaller than 0.01 km^2. Abd-Elrahman et al. (2011) described their experience with the use of mobile, ground-based hyperspectral sensor to estimate WQPs in freshwater aquaculture ponds approximately 0.002 km^2 in size and eutrophic or hypertrophic with *chl-a* from 0.8 to 494 µg/l.

This study was designed to identify characteristic patterns of water-surface reflectance spectra of small turbid waters, quarry lakes and fishponds, in the Třeboň basin. In these localities, suspended inorganic particles such as sand, clay, peat and organic debris from manuring of fishponds, together with a wide range of phytoplankton of different taxa (cyanobacteria, chlorococcal algae, diatoms), form a complicated optical environment. Ground-based and airborne sensing of advanced hyperspectral data of high spectral resolution were used to make assessments of concentrations of the major water-constituents (*chl-a* and TSS) and to choose the best algorithm to predict WQPs in these small productive waters. Measurements from hand-held devices and hyperspectral reflectance from an AISA instrument were compared

in order to establish whether measurements using airborne hyperspectral reflectance instrument for water-quality estimation throughout large areas correspond well with manual measurements and such an instrument can thus be used instead.

Fishpond regions in the Czech Republic as well as in Austria, Germany, Poland and France represent important component of European wetlands. Fulfilling the water-quality requirements and achieving a sustainable management of these aquatic ecosystems according to the Water Framework Directive (WFD 2000/60/EC) require the development of effective tools for the monitoring of different water bodies. Monitoring can help to predict natural processes in the environment and determine human impacts on ecosystems. Moreover, the knowledge of the amount of *chl-a* enables us estimate fishponds production, which can be important in terms both of protection against increase of eutrophication and optimization of fish management. Our study shows the simple application of the RS to the monitoring of a large number of small water bodies.

Data and methods

Study sites

Measurements were carried out during two summers (2008–2009) in the Třeboň basin, South Bohemia, Czech Republic (Fig. 1). Třeboň basin with area of 700 km^2 represents type of landscape where small water bodies and wetlands form about 15 % of area. Altogether 465 fishponds cover 7.5 km^2 (Jeník et al. 2002). The water area of the individual fishponds ranges from 0.01 to 5 km^2. Most of the fishponds are several 100 years old and look like small, shallow lakes. Fishponds are man-made water bodies formed by damming of shallow valleys, featuring flat bottoms with minimal slope towards the dam. Mean depth is around 1 m; maximum depth does not exceed 3 m by the outlet at the dam. Filling the fishponds with water and release of the water are easily controllable by the system of channels and ditches. Lužnice River, which is the main source of water for most of the Třeboň fishponds, is relatively rich in nutrients, although some fishponds are supplied with seepage water from their catchment. Fishponds fill with water in spring while inflow is stopped during summer when the theoretical
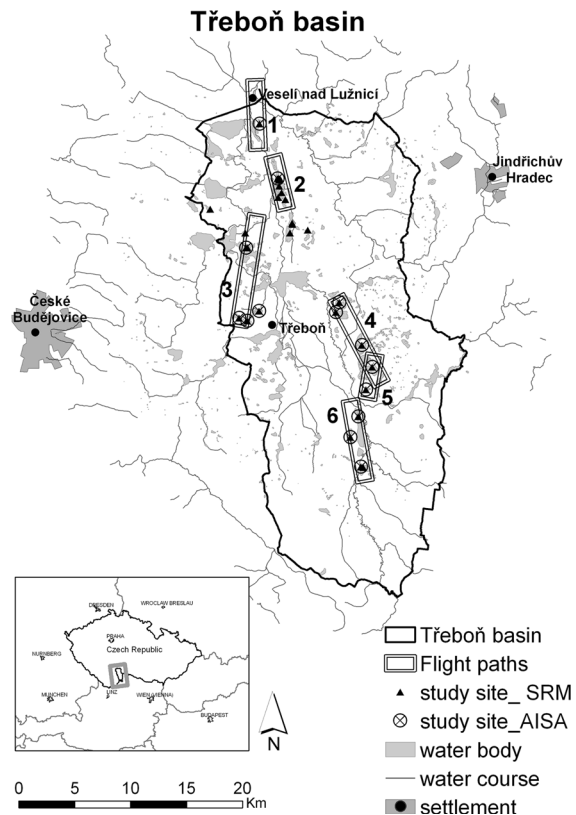
Fig. 1 Study area (48°48′49°11N, 14°38′15°00′E) located in South Bohemia, Czech Republic

resident time reaches more than 100 days. Fishponds are intentionally enriched with the aim of increasing the fish production, with common carp (*Cyprinus carpio L.*) the main cultivated fish species. Management is based on natural production processes, enhanced by additions like liming, fertilizing and direct fish feeding. Fish-production practices, together with influences from the catchment area, cause intensive eutrophication of the fishponds and shift basic water chemistry to more hydrogen carbonate type of water with Ca and Mg as principal cations (Pechar et al. 2002).

The flooded quarries are lake-like water bodies several decades old, with maximum depth ranging between 8 and 30 m, and areas are less than 0.5 km^2. Younger quarry lakes are used as source of raw water. Older water bodies serve for recreation, water sports and sport fishing. Chemical characteristics of waters of the quarry lakes reflect, to some extent, the original hydrochemical conditions of the Třeboň basin. Their

sulphate or sulphate–hydrogen carbonate type of waters can be explained by the influence of groundwater from quaternary and upper cretaceous sediments (Kroupa and Drbal 1990). Consequently, these sites have conserved their mesotrophic character, and their phytoplankton corresponds to the conditions the fishponds were in some 30–40 years ago.

Data collection on location

Sample collection

Water samples for laboratory analyses of WQPs and ground-based measurements of reflectance spectra of 28 fishponds and quarry lakes in the Třeboň basin were collected from July to September in 2008 and 2009. Fishponds localities were chosen according to flight lines of 36-km total length oriented from the south to the north of the entire Třeboň basin. Wide range of mezotrophic and hypertrophic fishponds was covered. The quarry lakes fitting into these lines were also included and examined, since they represent the oligotrophic–mezotrophic water type which occurred in this region before the period of fishpond eutrophication in the last century (Pechar et al. 2002).

Water samples were obtained by boat several tens of metres from fishpond dams or shorelines. Two litre samples were collected from the water surface and transported in polyethylene bottles to the laboratory within 4 h. Average depth of most of fishponds ranges between 0.7 and 0.9 m. Water column is usually well mixed, every night by convection, and during days, only a slight wind is enough to induce turbulent mixing. This sampling corresponds to the informative water layer which is accessible for reflectance reading. According to Arst (2003), in such types of turbid water, the informative layer is around 0.3 m.

Chl-a values were estimated by reading of absorbance with double beam UV–Vis spectrophotometer Heλios Alpha (Unicam, GB) at 664 nm after extraction with a mixture of 90 % acetone: methanol (Pechar 1987). TSS were determined as dry weight of seston captured on pre-weighed Whatman GF/C filters and dried to constant weight at 60 °C (Table 1).

Instrumentation

In situ reflectance was acquired using an AvaSpec2048-2 (Avantes BV, The Netherlands) spectroradiometer

(SRM data). AvaSpec is a dual-channel instrument acquiring data simultaneously in a spectral range of 200–1100 nm with a spectral resolution less than 1 nm. SRM spectra were obtained during cloud-free days with sunlight as the source of illumination. Measurements were taken roughly at midday—between 10 a.m. and 2 p.m. (CEST) ±4 h (Table 1) in order to minimize effects of the possible temporal changes in water environment and also to perform this measurement simultaneously or as close as possible to the AISA Eagle overflight.

Water-leaving radiance (L_w) and reference spectra of the calibrated Spectralon panel[1] (L_{ref}) measurements were performed simultaneously with two fibre optics ended by a collimating lens with field of view 8°. The 2-m-long fibres were mounted on a specially designed floater/pontoon holding the fibres in a vertical position (nadir view) over the water surface (approximately 20 cm above the surface) and away from the boat. Data were stored using Avasoft 5.1 Full software (Avantes BV, The Netherlands). The acquired data were imported into a spreadsheet (Excel 2007), and the hemispherical–conical reflectance factor (HCRF) (Schaepman-Strub et al. 2006) was calculated for each sample as the ratio of L_w/L_{ref} (Igamberdiev et al. 2011).

Raw data were normalized by its integral (over the spectrum in the range of 400–1010 nm) prior to clustering in order to preserve spectral shape information of the reflectance (Le et al. 2011) and align reflectance intensities on the same scale (for better comparison).

Algorithms from available literature have been tested for use for our terms and conditions. Simple but accurate algorithms were sought, which would enable evaluation of water quality based on various *chl-a* and TSS values. Correlations between the ground data and specific wavelengths of reflectance were calculated to estimate *chl-a* and TSS (using Statistica 9). The best results were achieved using (power) regression, thus the general relationship for water compound retrieval from a reflectance curve is given by the formula:

$$\text{OAS} = \sqrt[b]{\frac{R}{a}}, \tag{1}$$

---

[1] Diffuse PTFE material, reflects light with ca 98 % (http://www.avantes.com/Colorimetry/White-Reference-Tile/Detailed-product-flyer.html).

Table 1 List of localities measured by field spectroradiometer, data and time of reflectance acquisition and concentration of chlorophyll and total suspended solids

Optical class[a]	Locality	Date	Time (CEST)	TSS (mg/l)	Chl-a (µg/l)
1.	Cep I	29.7.2008	15:15	4.5	2
	Cep II	29.7.2008	14:00	2.3	2
	Tušť	29.7.2008	14:40	3.0	10
2.	Tušť	1.9.2009	14:30	5.8	17
	pískovny Veselí	29.7.2008	9:45	6.0	19
	Vizír	29.7.2008	15:55	5.9	25
	Verfle	29.7.2008	12:00	34.9	58
	Nový u Břilic	29.7.2008	12:30	39.5	89
	Staré Jezero	29.7.2008	16:15	18.9	81
	Břilický	29.7.2008	12:50	62.6	116
3.	Ženich	29.7.2008	18:05	44.4	257
	Velký Tisý	29.7.2008	11:10	41.8	270
	Nový Vdovec	29.7.2008	17:20	57.2	310
	Rod	29.7.2008	10:20	58.0	314
	Podsedek	29.7.2008	17:00	67.7	378
	Rod	3.8.2009	11:54	38.0	129
	Ostrý	5.8.2009	12:10	80.0	228
	Víra	6.8.2009	12:41	73.0	455
	Velký Tisý	6.8.2009	11:49	59.0	255
	Ptačí Blato	6.8.2009	13:28	39.3	134
	Klec	8.9.2009	11:08	67.0	249
	Dobrá Vůle	25.8.2009	12:11	37.1	170
	Klec	25.8.2009	10:50	28.7	131
	Potěšil	25.8.2009	9:58	62.0	301
	Rod	25.8.2009	13:00	66.7	315
	Služebný	25.8.2009	14:18	62.7	289
	Rod	8.9.2009	13:10	56.4	232
	Naděje	8.9.2009	12:35	46.7	222

[a] Derived from cluster analysis (see Results)

where OAS is the concentration of optically active substances (chl-a or TSS) in the water in µg/l or mg/l; R is the reflectance algorithm applied; and a and b are regression parameters.

The use of the chosen algorithm

The dataset obtained from the AISA reflectance measurements from 2010 was used to check the validity of the R_{714}/R_{650} and R_{806} algorithms.

Chl-a in µg.l^{-1} from the reflectance measurements was estimated according to the following equation:

$$\text{chl} - \text{a} = \sqrt[0.4135]{\frac{\frac{R_{714}}{R_{650}}}{0.214}}. \tag{2}$$

The estimation of the TSS [mg/l^{-1}] is based on an algorithm using NIR wavelengths. Calculations were obtained by the following equation:

$$\text{TSS} = \sqrt[0.9412]{\frac{R_{806}}{0.009}}. \tag{3}$$

Airborne hyperspectral images (AISA data)

Airborne measurements were acquired by a VNIR (visible and near infrared) airborne hyperspectral sensor AISA Eagle (Specim Ltd, Finland). The AISA Eagle System, mounted in a single-engine light aircraft, is a pushbroom imaging system with a spectral range from 400 to 1000 nm, the highest

achievable spectral resolution of 2.4 nm, and spatial resolution between 0.4 and 6.0 m. More detailed information concerning technical specifications is given by Hanuš et al. (2008).

The hyperspectral data were acquired between 09:40 and 10:30 a.m. (CEST) on 29 July 2008 together with the ground spectroradiometer measurement by AvaSpec to enable comparison between the two methods (SRM vs. AISA). The AvaSpec reflectance measurements were done on the same localities in flight lines in order to independently verify airborne dataset. Flight speed was 50 m/s, and the flight height of 1850 m yielded a pixel size of 3.0 × 3.0 m. Data were sensed in 260 bands with a 3.0-m spatial resolution; 50° field of view; and 3.5-nm spectral resolution. The same airborne measurements were conducted in 2010 in order to verify the acquired algorithm.

Simultaneously with the hyperspectral flights (under the same illumination conditions), supportive ground measurements for calibration and validation purposes were carried out. An ASD FieldSpec-3 spectroradiometer was used to measure the optical properties of reference targets. These targets represent spatially and radiometrically homogenous natural or artificial ground surface with behaviour of near-Lambertian reflector (e.g., bare soil, clay, concrete, etc.) present in the image (Brook and Ben Dor 2011). Just only bright targets (clay and beach volleyball court) were used for verification and vicarious calibration of AISA Eagle data.

Microtops II Sunphotometer measurements were used for the estimation of actual atmospheric conditions, aerosol optical thickness (AOT) and water vapour (WV). Pre-processing of AISA Eagle data acquired during the Třeboň 2008 flight campaign was performed in CaliGeo software (radiometric corrections), PARGE (ortho-georectification) and ATCOR-4 (atmospheric corrections). Hyperspectral image data were georeferenced into the UTM 33 N (WGS-84) coordinate system. Atmospheric corrections were performed in the ATCOR-4 software package (Richter 2007). ATCOR-4 is designed for atmospheric, topographic and BRDF corrections of airborne spectroscopy image data. Atmospheric corrections implemented in ATCOR-4 are based on the physical model of the atmosphere MODTRAN4 (Schläpfer and Odermatt 2006). Data acquired during the supportive ground campaign were utilized for vicarious

calibrations and validations of atmospherically corrected images. The known reflectances of one ground reference target and atmospheric parameters measured by sunphotometer (WV, AOT) were used for fine-tuning of the model according to ATCOR-4.

The remaining reference targets were used for validation of the corrected images.

The AISA reflectance curves were created using PCI Geomatica software (Geomatica Algorithm Reference 2003). Data were converted to ASCII format and loaded in a spreadsheet. Statistical analysis for this study was completed using Microsoft office Excel 2007 and Statistica 9.

Results

Spectral response of water bodies

In situ reflectance spectra captured by means of hand-held spectroradiometer ranged between 0 and up to 12 % for the whole electromagnetic spectrum (Fig. 2a).

In general, oligotrophic waters (quarry lakes mostly) were characterized by a distinct peak in the "green region" (around 560 nm). Values of green reflectance of our localities varied from 1 to 12 %.

Distinct peaks in green, red and NIR wavelengths were found in more productive fishpond waters. Values of reflectance were 1–6 % in the green region, 2–4 % around 650 nm and between 4 and 12 % at around 700 nm.

In general, increases of chl-a and TSS resulted in increased reflectance within the red-NIR region of the spectral curves as well as in a shift in the red-peak position. In this study, water bodies with a low chl-a showed peaks approximately around 680–705 nm, while a shift in the peak position up to 715 nm occurred with increasing chl-a (Fig. 2a).

Classification of water bodies

Different categories of the reflectance spectra of different water bodies were found according to spectral shape and chl-a. K-means cluster analysis showed three distinct spectral classes from the SRM data (Fig. 3; Table 1). The first class (Fig. 3a) contains waters of flooded quarry lakes (chl-a = 2–10 µg/l; TSS = 2–4.5 mg/l). The very low
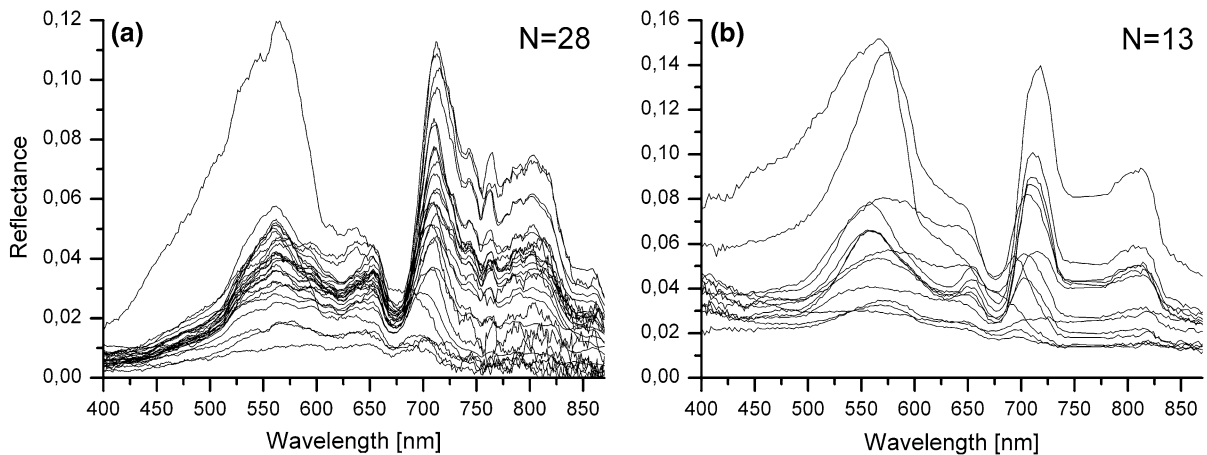
Fig. 2 The hyperspectral reflectance measured by **a** hand-held Spectroradiometer (2008) and **b** AISA (2008)
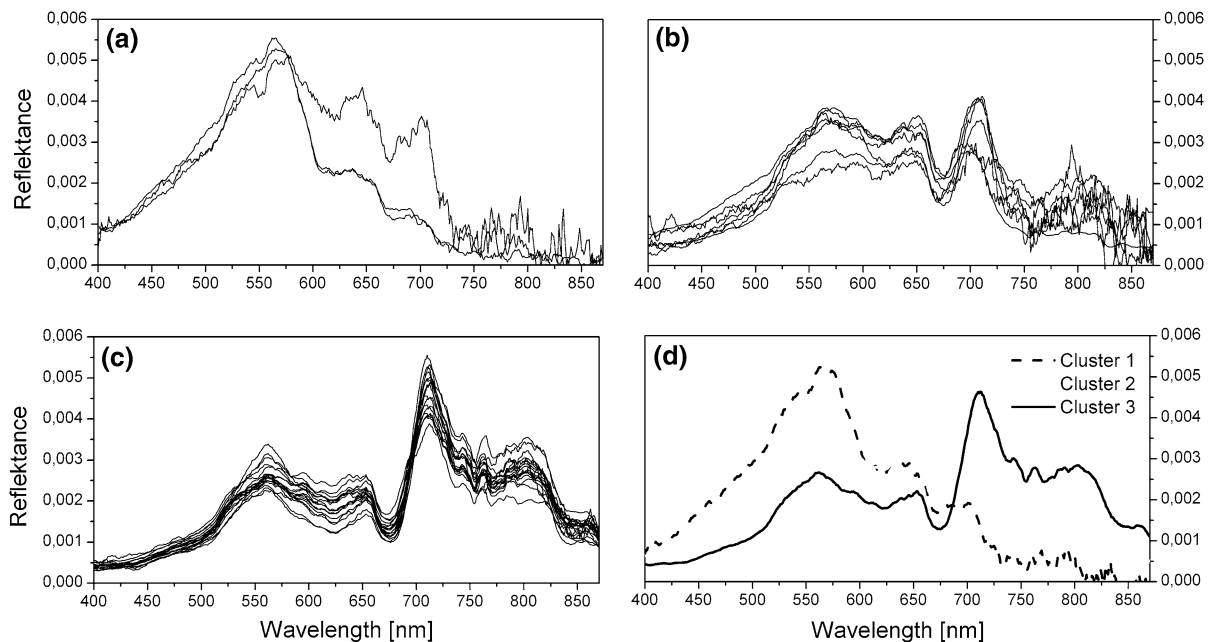
Fig. 3 Three cluster groups of the spectral reflectance measured with SRM: **a** cluster 1, **b** cluster 2, **c** cluster 3, and **d** the average reflectance spectrum obtained for each of the cluster groups

chl-a levels of about 2 µg/l were similar to that of oligotrophic waters, although the TSS of these mining localities reached up to 5 mg/l especially where they are still in use. Due to these conditions, the reflectance spectra showed maxima in the green region (at 565 nm), and there was a gradual decrease in the longer wavelengths (red and IR). The second class (Fig. 3b) consists of quarry lakes where extraction ceased several years ago (*chl-a* = around 18 µg/l;

TSS = around 6 mg/l) and fishponds with relatively low *chl-a* (25–116 µg/l) and TSS (6–62 mg/l) values. The reflectance spectra revealed a specific pattern of three characteristic peaks in the green (near 560 nm), red (near 650 nm) and NIR (near 700 nm) regions, respectively, and one significant through near 675 nm. All of these peaks are approximately equal in magnitude or the peaks near 700 nm are slightly higher. Water bodies with high *chl-a* levels ranging from 128

to 455 µg/l and a very high content of TSS (29–80 mg/l) were grouped within the third category. The spectra still showed three main peaks, as seen in the previous group, although two peaks in the visible (VIS) region were much lower while significantly higher reflectance values are found for the third peak near 700 nm (Fig. 3c). Two subclasses could be observed within the third group on the basis of subjective comparison. The first includes waters with lower *chl-a* levels where reflectance spectra show a plateau in the green and red wavelengths and the peak near 700 nm is only slightly higher in comparison. In the second subclass, representing highly eutrophicated waters, the green peak was more distinct and the peak near 700 nm was significantly higher than the two peaks in the VIS part of the spectrum.

Algorithms for simple but accurate estimation of WQPs

All statistical relationships between reflectance patterns and optically related water characteristics were significant at $p < 0.05$. Results of correlation analyses for the different algorithms are summarized in Table 2.

Chlorophyll estimation

The most significant relationships for the majority of the algorithms used in combination with both *chl-a* ($r^2 = 0.74$–0.96) and TSS ($r^2 = 0.68$–0.89) were found with power regression.

Many of the algorithms, whether they use only a simple wavelength or a band ratio between IR and VIS (green or red) wavelengths, gave comparable results ($r^2 > 0.9$) in predicting the *chl-a*. However, best results ($r^2 = 0.96$) were obtained with the single-band ratio using wavelengths of 714 and 650 nm, which were therefore chosen for further analysis (Table 2; Fig. 4).

Estimation of total suspended solids

There is little consensus in either the wavelengths used or in the form of the calculation of the relationships between TSS and remote-sensing reflectance. This is due to the diversity of the sediment types, especially in terms of particle size and colour, which absorb and scatter light differently. Although determination

coefficients between TSS and reflectance algorithms were on average lower than the coefficients for chlorophyll, acceptable results ($r^2 > 0.80$) for the estimation were still obtained (Table 2). The power model was again found the best predictor, giving the best algorithm using single reflectance values in the NIR region (R_{806}) ($r^2 = 0.89$).

The relationship between the band ratio algorithm using NIR and red (R_{806}/R_{670}) and TSS was well correlated ($r^2 = 0.86$). The band ratio at NIR and green wavelengths (R_{850}/R_{550}) was less significant ($r^2 = 0.54$). Determination coefficients ranged mostly between 0.80 and 0.84. Peak position and peak height gave equally good relationships ($r^2 = 0.84$) whereas peak area exhibited less significant predictions for TSS ($r^2 = 0.74$). Algorithms based on band differences were completely ineffective predictors: both regarding *chl-a* and TSS.

Airborne data (AISA)

Simultaneous SRM and AISA data obtained in 2008 showed very similar patterns, with AISA hyperspectral reflectance average higher values being achieved (Figs. 2b, 5). The instantaneous field of view of AISA system is 0.11 deg, and therefore, the measured HCRF could be assumed as hemispherical-directional reflectance factor (HDRF). The collimating lenses of the SRM used bring the geometry of the obtained reflectance closer to the AISA system although some inconsistency still remains for the measurement geometry between the two systems resulting in slightly different reflectance values (IFOV, tilt for across-the-track AISA view).

Visible similarities can be found between the differently obtained spectral curves ($r^2 = 0.85$) as seen in Fig. 5a, b. Individual spectra were assigned to the average reflectance spectra obtained for each cluster of the SRM measurement after normalization of the AISA data (unification of reflectance intensity onto the same scale).

Figure 5c compares maximum reflectance values measured around 700 nm by the two sensors for individual water bodies. The maximum value is readily used in algorithms for estimation of *chl-a* in inland waters. The correlation plot shows statistical similarity between the two methods, and both methods can be said to give comparable results.

Table 2 Coefficients of relationships between chlorophyll or total suspended solids and water surface reflectance measured by hand-held spectroradiometer

Algorithm	Source	Chl-a (r^2)		TSS (r^2)	
		Linear	Power	Linear	Power
Single band or wavelength					
Peak position near 700 nm	Gitelson (1992)	0.63	**0.91**	0.70	**0.84**
R_{red}/NIR $_{max}$	Zimba and Gitelson (2006)	0.73	0.74	0.62	0.75
$R_{699–705}$	Kallio et al. (2001)	0.69	0.76	0.65	0.77
$R_{705–714}$	Kallio et al. (2001)	0.74	0.81	0.65	0.81
$R_{698–716}$	Dekker (1993)	0.73	0.80	0.65	0.80
	Kallio et al. (2001)				
R_{806}	Arenz et al. (1996)	0.84	**0.88**	0.73	**0.89**
Single band ratio					
R_{440}/R_{550}	Gordon and Morel (1983)	0.29	0.33	–	**–**
R_{700}/R_{560}	Menken et al. (2006)	0.75	**0.91**	0.68	0.73
R_{700}/R_{670}	Menken et al. (2006)	0.76	**0.91**	0.61	0.75
R_{700}/R_{675}	Gitelson and Yacobi (2004)	0.76	**0.92**	0.62	0.80
R_{redmax}/R_{675}	Gitelson et al. (1993)	0.81	0.86	0.60	0.77
R_{710}/R_{675}	Schalles et al. (2001)	0.80	**0.92**	0.63	**0.83**
R_{806}/R_{571}	Arenz et al. (1996)	0.85	**0.93**	0.77	0.82
R_{806}/R_{670}	Menken et al. (2006); Arenz et al. (1996)	**0.93**	**0.93**	0.76	**0.86**
R_{714}/R_{650}	Zimba and Gitelson (2006)	0.86	**0.96**	0.68	0.82
R_{850}/R_{550}	Doxaran et al. (2005)	0.54	–	0.54	–
$(R_{699–705})/(R_{670–677})$	Kallio et al. (2001)	0.77	**0.91**	0.62	0.79
$(R_{699–714})/(R_{670–685})$	Dekker (1993)	0.78	**0.91**	0.61	0.81
Band difference					
$R_{833} - R_{1004}$	Sterckx et al. (2007)	0.75	–	0.64	–
$(R_{699–705}) - (R_{747–755})$	Kallio et al. (2001)	0.01	0.16	0.04	0.15
$[(R_{560}) - (R_{520})]/[(R_{560}) + (R_{520})]$	Gitelson et al. (1993)	0.20	0.21	0.18	0.22
3 Band model (reciprocal reflectance)					
$\left[R_{(650)}^{-1} - R_{(710)}^{-1} \right] \times R_{(740)}$	Zimba and Gitelson (2006)	**0.90**	–	0.68	–
Peak height	Gitelson (1992); Schalles et al. (2001)	0.77	0.87	0.60	**0.84**
Peak area		0.70	0.78	0.61	0.74

The use of the chosen algorithm

There is a close relationship between the laboratory-measured values of chl-a and the concentrations estimated (Fig. 6a, $r^2 = 0.91$) based on the algorithm R_{714}/R_{650} (Eq. 2).

This relationship is even more significant when cyanobacteria dominate the phytoplankton composition (Fig. 6b, $r^2 = 0.96$).

As regards the estimation of the total TSS (Fig. 6c) from reflectance data (Eq. 3), the correlation is weaker ($r^2 = 0.76$) than in the case of chl-a. The variability of TSS concentration increases during summer season. Also, its matrix, as well as its characteristics becomes more complex, which is probably the reason for the more complicated estimation.

Discussion

Spectral reflectance of water bodies

These measured reflectance values (1–12 %) correspond with other studies of inland waters with similar

composition (Menken et al. 2006; Arenz et al. 1996). Nevertheless, differences can be found mostly in the location of reflectance maxima in certain parts of the electromagnetic spectrum. The differences found in the obtained reflectance spectra can be attributed to the various contributing absorptions of phytoplankton and suspended sediments (Le et al. 2011).

Values of green reflectance of our localities with oligotrophic character vary from 1 to 12 %, while the literature shows that waters of similar composition and of similar spectral shape usually correspond to 1–2 %
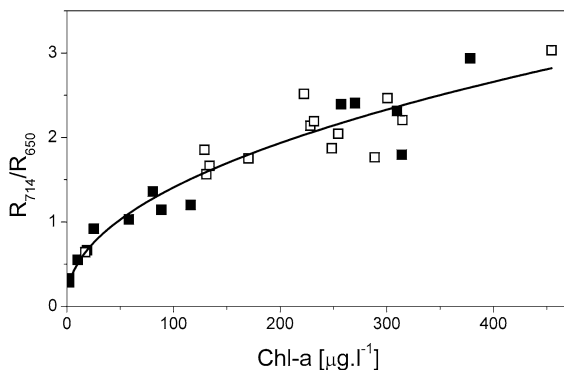
Fig. 4 The best algorithm for chlorophyll estimation for conditions at Třeboň basin (for spectroradiometer data). $y = 0.214x^{0.4135}$; $r^2 = 0.96$. *Black squares* represent measurements from 2008, *white squares* from 2009

(Ouillon et al. 2008) or 1–5 % (Arenz et al. 1996). The higher reflectance of our localities compared with the clear lakes discussed in the literature may be caused by the presence of a high amount of light-refracting mineral particles, giving rise to the low transparency. The methods of measurement and the conditions during measurement can also affect the magnitude of reflectance (Bhatti et al. 2009).

For lakes of similar composition as our productive fishponds, Menken et al. (2006) reported 0.4–0.6 % in the green region, while Arenz et al. (1996) showed similar reflectance values to those of our studies (up to 5 %). Igamberdiev et al. (2011) reported reflectance in small, shallow waters (kettle holes) to be up to 5 %. In the region at around 700 nm, the spectra appeared to be very similar to the data of Menken et al. (2006) who investigated lakes varying in water quality (*chl-a* 8–397 mg/m³) and achieved similar reflectance values (up to 10 %).

For turbid hypereutrophic waters, with *chl-a* ranging from 170 to 3000 mg/m³, Zimba and Gitelson (2006) reported very high green reflectance (up to 25 %), a higher peak around 700 nm (30 %) and very variable reflectance in the NIR region (2–18 %).

Increase in reflectance within the red-NIR region as well as a shift in the red peak position has been observed due to *chl-a* and TSS increase. Such a shift has been described, e.g. by Mittenzwey et al. (1992) or
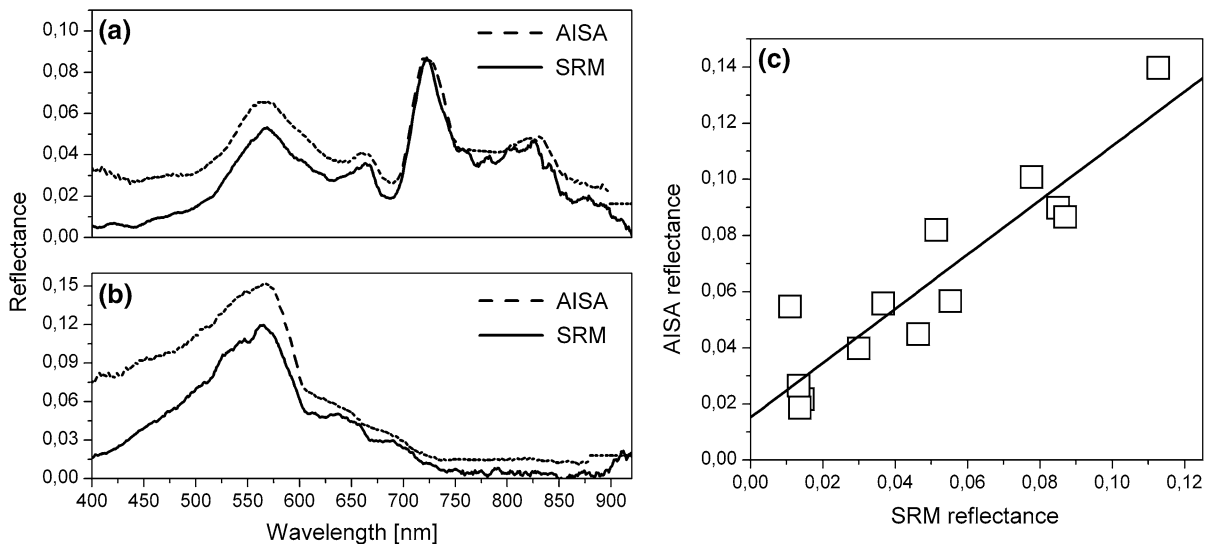
Fig. 5 Comparison of spectral signature of water from airborne measurement by AISA (*dashed line*) and field spectroradiometer measurement (*solid line*). **a** fishpond Ženich, **b** quarry lake Cep

II, **c** the relation between reflectance values of spectroradiometer (SRM) and AISA at reflectance maximum around 700 nm. $y = 0.976x + 0.0152$; $r^2 = 0.8488$

Fig. 6 a Measured *chl-a* versus *chl-a* estimated by means of R_{714}/R_{650} algorithm.
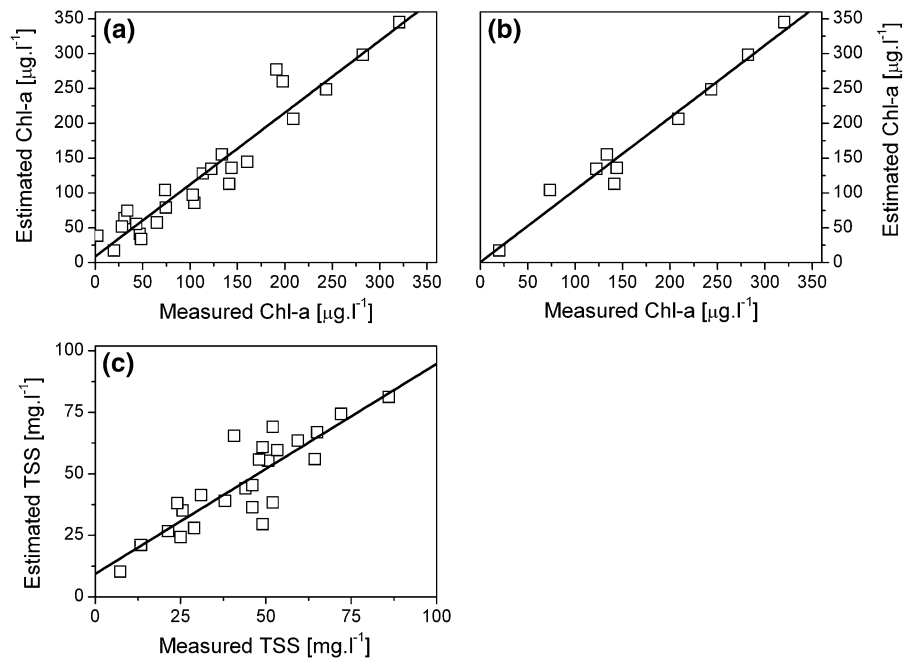$y = 1.0325x + 8.9396$; $r^2 = 0.919$; **b** Measured *chl-a* versus *chl-a* estimated by means of R_{714}/R_{650} algorithm on localities with predominance of cyanobacteria.
$y = 1.0372x + 0.8327$; $r^2 = 0.969$; **c** Total suspended solid concentrations calculated on the base of R_{806} algorithm versus laboratory-measured TSS concentrations; $y = 0.8538x + 9.3707$; $r^2 = 0.766$

Gitelson ([1992](#)) for inland waters, and also by Morel and Prieur ([1977](#)) for marine environments. These phenomena are thought to be caused by a minimum reached in the combined absorption of all constituents and the water itself and also by other factors including backscattering and absorption from other contributors such as suspended solids, other than phytoplankton (Zimba and Gitelson ([2006](#)); Mittenzwey et al. [1992](#)).

Classification of water bodies

Similar categories to the ones obtained in this research were reported by Shi et al. ([2013](#)), with optical classification of waters to obtain type-specific algorithms for better or more precise estimation of *chl-a* in optically complex inland waters. This approach was not chosen for this study as only one simple, quick, and sufficiently accurate algorithm for estimation of *chl-a* was sought. However, the defined optical classification of water bodies can be used for assessment of the received spectra as in fact it defines the degree of eutrophication, this being the key factor for the spectral shape of water reflectance. This approach could be used to observe eutrophication process and thus for rapid detection of errors in fishery or landscape management. According to this classification, quarry lakes can be compared to oligotrophic lakes as the eutrophication in these waters is low or it has just started depending on the time since the end of mining and thus on the age of the submersion. In the case of the fishponds, fish production is the crucial factor for eutrophication degree and thus for spectral signature of the water body.

Algorithms for simple but accurate estimation of WQPs

Gitelson ([1992](#)) reported linear regression relationships ($r^2 = 0.93$) for the max-red (~ 700 nm) position (from 683 nm at no *chl-a* to 713 nm at 100 mg *chl-a*/m^3), in contrast to our results that power regression gave the best results for *chl-a* estimation using various algorithms. Rundquist et al. ([1995](#)) described a highly nonlinear relationship but with less steep slope than that found by Gitelson ([1992](#)), probably due to differences in the spectral resolution of the spectroradiometers or differences in the recovery efficiencies of the respective chlorophyll techniques. A more complex three-band model, which is mostly used for large and cleaner lakes as well as MODIS/MERIS data, did not improve the accuracy of *chl-a* estimation ($r^2 = 0.90$, linear) as was presented by Zimba and Gitelson ([2006](#)).

Igamberdiev et al. ([2011]) suggested that the peak position algorithm (R_{max} near 700 nm) cannot be applied for *chl-a* estimation in very small, shallow waters due to high variability of hydromorphological characteristics, algae content and resuspension. Similar conditions occur also in fishponds where the entire water column and thus water-leaving spectra are influenced by mixing and turbulence of sediments (the effect of small mixed water bodies). Despite this fact, the algorithm was relatively simple and adequately accurate ($r^2 = 0.91$) for our localities.

Also lower values of *chl-a* can cause an uncertainty in the determination, especially for *chl-a* < 10 mg/m^3 as Mittenzwey et al. ([1992]) found in natural mesotrophic and eutrophic (5–350 mg/m^3) waters using R_{705}/R_{670} ratio. Menken et al. ([2006]), on the other hand, presented IR/red ratio as the best predictor of *chl-a* for various conditions including high turbidity and CDOM.

The best algorithm for TSS estimation was the one using single reflectance value in the NIR region. Arenz et al. ([1996]) attributed the peak at 800 nm to inorganic suspended solids. They obtained the same results ($r^2 = 0.89$) for the algorithm although using the log-linear model instead. The use of the NIR region for TSS determination in surface waters has been suggested to be due to the least impact of *chl-a* and coloured dissolved organic carbon in this spectral region (Sterckx et al. [2007]). Algorithms using single band or band ratio (Sterckx et al. [2007]; Nechad et al. [2010]) of red and NIR region of the spectrum (as for the *chl-a* estimation) produced comparable results. The algorithm based on NIR/red ratio gave slightly worse TSS estimation. However, the band ratio at NIR and green wavelengths were not significant, although Doxaran et al. ([2005]) obtained closer linear correlation (0.96) and reported that inorganic material was the predominant influence. In that case, the relationship could be used to quantify both inorganic- and organic-suspended material.

Not even algorithms using wavelength differences in the NIR part of the spectrum (Sterckx et al. [2007]) were able to provide a sufficiently good prediction of TSS in the local water conditions ($r^2 = 0.64$, linear model). Gordon and Morel ([1983]) blue/green ratio yielded no valuable results where coefficient values were lower than 0.33 for all datasets and even lower ($r^2 > 0.1$) if only the data from relatively clear quarry lakes were used (data not shown).

Airborne data

The observed differences in the reflectance values of SRM and AISA can be related to the geometry of the measurement (sensing/data acquisition) depending on different conditions within the sun–sample–sensor system and the vicarious calibration. We assume that the largest influence on the differences between SRM and AISA spectral curves lies in the method of vicarious calibration. Due to impossibility to find more reference surfaces only one reference target for the calibration of AISA signal was used in this study, which may aid in avoiding artefacts in the corrected spectra (negative reflectance), but, on the other hand, it may have caused lesser accuracy for the absolute reflectance values when close to zero. However, the shape of the spectral curve for the data acquired by the AISA system was definitely improved by the vicarious calibration performed.

Rundquist et al. ([1995]) regarded each maximum as being caused by the interaction of algal cell scattering and the minimum values by a combined effect of pigment and water absorption.

Therefore, it can be concluded that it is possible to use hyperspectral reflectance for estimation of concentration of chlorophyll in our localities. The advantage is the possibility to monitor water bodies in a large area simultaneously, as a synoptic view is gained from one image received in one flight.

Conclusions

We used RS for monitoring water quality in small, highly turbid aquatic habitats which are part of larger wetland complexes. Despite many similarities with other inland waters, the sites we investigated exhibit some differences. Several algorithms for the relationships between reflectance patterns and WQPs (*chl-a* and TSS) were tested.

Optically active compounds cause specific spectral signatures of the measured water reflectance. The measurements enabled differentiation of the water bodies into three spectral categories corresponding to their chlorophyll level. Using the collected data, relationships between water reflectance and concentrations of water compounds were also established.

The relationships between water compounds and reflectance values obtained by in situ field

measurements showed higher determination coefficients for the power model compared with the linear and exponential models. For the spectroradiometer data the best algorithm for estimation of chl-a was found to be the simple reflectance ratio of R_{714}/R_{650} ($r^2 = 0.96$) using the power law. In addition, most of the NIR and VIS (red or green) band ratios seemed to be good predictors for chl-a in our study area. The best algorithm for estimation of TSS was the single wavelength at 806 nm ($r^2 = 0.89$; power law).

These results, together with the fact that the data obtained by ground reflectance measurements correlated well with the results obtained by VNIR airborne hyperspectral AISA Eagle System, prove this method to be an effective tool for monitoring surface water quality.

These measurements confirmed functional performance of the algorithms used for estimating certain WQPs. Compared with the more traditional approaches of sample collection and analysis the potential advantages of RS include the increased spatial and temporal resolution that may prove useful and important for assessing and managing water quality. More specifically, this approach provides results of sufficient quality to distinguish basic levels of eutrophication of small inland productive waters.

References

Abd-Elrahman A, Croxton M, Pande-Chettri R et al (2011) In situ estimation of water quality parameters in freshwater aquaculture ponds using hyperspectral imaging system. ISPRS J Photogramm Remote Sens 66:463–472. doi:10.1016/j.isprsjprs.2011.02.005

Arenz RF, Lewis WM, Saunders JF (1996) Determination of chlorophyll and dissolved organic carbon from reflectance data for Colorado reservoirs. Int J Remote Sens 17:1547–1565. doi:10.1080/01431169608948723

Arst H (2003) Optical properties and remote sensing of multicomponental water bodies. Springer-Praxis book in marine science and coastal management. Springer, Berlin

Bhatti AM, Rundquist D, Schalles J et al (2009) A comparison between above-water surface and subsurface spectral reflectances collected over inland waters. Geocarto Int 24:133–141. doi:10.1080/10106040802460707

Brook A, Ben Dor E (2011) Supervised vicarious calibration (SVC) of hyperspectral remote-sensing data. Remote Sens Environ 115:1543–1555. doi:10.1016/j.rse.2011.02.013

Chipman JW, Olmanson LG, Gitelson AA (2009) Remote sensing methods for lake management: a guide for resource managers and decision-makers. Developed by the North American Lake Management Society in collaboration with Dartmouth College, University of Minnesota, and University of Nebraska for the United States environmental protection agency

Dekker AG (1993) Detection of optical water quality parameters for eutrophic waters by high resolution remote sensing. Ph.D Thesis, Vrije universiteit. Amsterdam

Doxaran D, Cherukuru RCN, Lavender SJ (2005) Use of reflectance band ratios to estimate suspended and dissolved matter concentrations in estuarine waters. Int J Remote Sens 26:1763–1769. doi:10.1080/01431160512331314092

Geomatica Algorithm Reference (2003) PCI Geomatics. 50 West Wilmot Street Richmond Hill, Ontario

Gitelson A (1992) The peak near 700 nm on radiance spectra of algae and water: relationships of its magnitude and position with chlorophyll concentration. Int J Remote Sens 13:3367–3373. doi:10.1080/01431169208904125

Gitelson A, Yacobi Y (2004) Monitoring quality of productive aquatic ecosystem: requirements for satellite sensors. BALWOIS 2004, Ohrid, FY Republic of Macedonia

Gitelson A, Szilagyi F, Mittenzwey K-H (1993) Improving quantitative remote sensing for monitoring of inland water quality. Water Res 27(7):1185–1194

Gordon HR, Morel A (1983) Remote assessment of ocean color for interpretation of satellite visible imagery: a review. Springer-Verlag, New York

Gurlin D, Gitelson AA, Moses WJ (2011) Remote estimation of chl-a concentration in turbid productive waters—return to a simple two-band NIR-red model? Remote Sens Environ 115:3479–3490. doi:10.1016/j.rse.2011.08.011

Hanuš J, Malenovský Z, Homolová L, Kaplan V, Lukeš P, Cudlín P (2008) Potentials of the VNIR Airborne Hyperspectral System AISA Eagle. GIS Ostrav 2008:27–30

Igamberdiev RM, Grenzdoerffer G, Bill R et al (2011) Determination of chlorophyll content of small water bodies (kettle holes) using hyperspectral airborne data. Int J Appl Earth Obs Geoinf 13:912–921. doi:10.1016/j.jag.2011.04.001

Jeník J, Květ J, Papáčková L (2002) Freshwater wetlands and their sustainable future: a case study of the Třeboň Basin Biosphere Reserve, Czech Republic. UNESCO, Paris

Kallio K, Kutser T, Hannonen T, Koponen S, Pulliainen J, Vepsäläinen J, Pyhälahti T (2001) Retrieval of water quality from airborne imaging spectrometry of various lake types in different seasons. Sci Total Environ 268:59–77

Kroupa M, Drbal K (1990) Chemistry of waters in flooded sand pits and its development. In: Krupauer V, Bican J, Drbal K (eds) Extracted ecosystem of Třeboň Biosphere Reserve. Academia Praha, Praha-Staré Město, pp 49–62

Le CF, Li YM, Zha Y et al (2011) Remote estimation of chlorophyll a in optically complex waters based on optical classification. Remote Sens Environ 115:725–737. doi:10.1016/j.rse.2010.10.014

Liu Y, Islam MA, Gao J (2003) Quantification of shallow water quality parameters by means of remote sensing. Prog Phys Geogr 27:24–43. doi:10.1191/0309133303pp357ra

Menken KD, Brezonik PL, Bauer ME (2006) Influence of chlorophyll and colored dissolved organic matter (CDOM) on Lake Reflectance Spectra: implications for Measuring Lake Properties by Remote Sensing. Lake Reserv Manag 22:179–190. doi:10.1080/07438140609353895

Mittenzwey K-H, Ullrich S, Gitelson AA, Kondratiev KY (1992) Determination of chlorophyll a of inland waters on the basis of spectral reflectance. Limnol Oceanogr 37:147–149. doi:10.4319/lo.1992.37.1.0147

Morel A, Prieur L (1977) Analysis of variations in ocean color. Limnol Oceanogr 22:709–722. doi:10.4319/lo.1977.22.4.0709

Moses WJ, Gitelson AA, Berdnikov S et al (2012) Operational MERIS-based NIR-red algorithms for estimating chlorophyll-a concentrations in coastal waters—the Azov Sea case study. Remote Sens Environ 121:118–124. doi:10.1016/j.rse.2012.01.024

Nechad B, Ruddick KG, Park Y (2010) Calibration and validation of a generic multisensor algorithm for mapping of total suspended matter in turbid waters. Remote Sens Environ 114:854–866. doi:10.1016/j.rse.2009.11.022

Olmanson LG, Brezonik PL, Bauer ME (2011) Evaluation of medium to low resolution satellite imagery for regional lake water quality assessments. Water Resour Res 47:W09515. doi:10.1029/2011WR011005

Ouillon S, Douillet P, Petrenko A et al (2008) Optical algorithms at satellite wavelengths for total suspended matter in tropical coastal waters. Sensors 8:4165–4185. doi:10.3390/s8074165

Pechar L (1987) Use of an acetone: methanol mixture for the extraction and spectrophotometric determination of chlorophyll-a in phytoplankton. Algol Stud Archiv für Hydrobiol Suppl Vol 46:99–117

Pechar L, Přikryl I, Faina R (2002) Hydrobiological evaluation of Třeboň fishponds since the end of 19th century. In: Květ J, Jeník J, Soukupová L (eds.) Freshwater wetlands and their sustainable future: a case study of the třeboň basin biosphere reserve, Czech Republic. Man and the Biosphere Series 28, UNESCO & The Parthenon Paris, pp 31–62

Randolph K, Wilson J, Tedesco L et al (2008) Hyperspectral remote sensing of cyanobacteria in turbid productive water using optically active pigments, chlorophyll a and phycocyanin. Remote Sens Environ 112:4009–4019. doi:10.1016/j.rse.2008.06.002

Richter R (2007) Atmospheric/topographic correction for airborne imagery, ATCOR-4 user guide, version 4.2, deutsches zentrum fuer luft- und raumfahrt e. v. (dlr) and rese applications schläpfer, p 125

Rundquist DC, Schalles JF, Peake JS (1995) The response of volume reflectance to manipulated algal concentrations above bright and dark bottoms at various depths in an experimental pool. Geocarto Int 10:5–14. doi:10.1080/10106049509354508

Schaepman-Strub G, Schaepman ME, Painter TH et al (2006) Reflectance quantities in optical remote sensing definitions and case studies. Remote Sens Environ 103:27–42. doi:10.1016/j.rse.2006.03.002

Schalles JF, Rundquist DC, Schiebe FR (2001) The influence of suspended clays on phytoplankton reflectance signatures and the remote estimation of chlorophyll. Verh Int Ver Limnol 27:3619–3625

Schläpfer D, Odermatt D (2006) MODO -modtran4 for remote sensing applications. ReSe Applications Schläpfer, Wil, p 78

Shi K, Li Y, Li L et al (2013) Remote chlorophyll-a estimates for inland waters based on a cluster-based classification. Sci Total Environ 444:1–15. doi:10.1016/j.scitotenv.2012.11.058

Sokoletsky LG, Lunetta RS, Wetz MS, Paerl HW (2011) MERIS retrieval of water quality components in the turbid albemarle-pamlico sound estuary, USA. Remote Sens 3:684–707. doi:10.3390/rs3040684

Sterckx S, Knaeps E, Bollen M et al (2007) Retrieval of suspended sediment from advanced hyperspectral sensor data in the Scheldt estuary at different stages in the tidal cycle. Mar Geod 30:97–108. doi:10.1080/01490410701296341

Sudduth KA, Jang G-S, Lerch RN, Sadler EJ (2005) Estimating water quality with airborne and ground-based hyperspectral sensing. ASAE Paper No. 052006. St. Joseph, Mich.: ASAE

WFD 2000/60/EC: Directive 2000/60/EC of the European parliament and of the council establishing a framework for the community action in the field of water policy

Yacobi YZ, Moses WJ, Kaganovsky S et al (2011) NIR-red reflectance-based algorithms for chlorophyll-a estimation in mesotrophic inland and coastal waters: lake Kinneret case study. Water Res 45:2428–2436. doi:10.1016/j.watres.2011.02.002

Zimba PV, Gitelson A (2006) Remote estimation of chlorophyll concentration in hyper-eutrophic aquatic systems: model tuning and accuracy optimization. Aquaculture 256:272–286. doi:10.1016/j.aquaculture.2006.02.038

Appendix 5

Article 0a

AIRBORNE IMAGING SPECTROSCOPY AT CZECHGLOBE – POTENTIAL, DATA PROCESSING AND QUALITY INDICATORS

Jan Hanus

Tomas Fabianek

Dr. Veroslav Kaplan

Assoc. Prof. Frantisek Zemek

Centrum vyzkumu globalni zmeny AV CR, CzechGlobe, **Czech Republic**

ABSTRACT

Airborne imaging spectroscopy techniques (also often called airborne hyperspectral remote sensing) are providing unique operational tools for local-to-regional spatial and temporal monitoring of landscape status and change. Compared to traditional multispectral data, it offers a continuous coverage of electromagnetic spectra within their spectral range, where the so-called "spectral signatures" of the surface are acquired rather than discrete values within broad spectral bands. This allows a development of new methods for Earth surface object detection including a high accuracy target detection and/or quantitative retrieval of surface properties. The application of hyperspectral remote sensing data in the scientific and even the commercial community for creation of maps is quite broad - from agriculture (yield prediction and precise farming), forestry (forest health status, biomass estimation, species composition mapping) through geology (e.g. mapping of minerals, land degradation assessment), up to limnology (e.g. water quality evaluation), and other domain (e.g. military).

Numbers of hyperspectral data providers are now present for surveys in Europe. However, each is using specific processing chain and harmonized quality indicators and quality layers accompanying hyperspectral data are often missing. That was the rationale for formation of the Joint Research Activity JRA2 "HYQUAPRO" within the FP7 EUFAR project (http://www.eufar.net). JRA2 was focused on developing of standardized quality layers for hyperspectral data. Partners of HYQUAPRO are among others PML/NERC, INTA, DLR, VITO/RSL, CVGZ - GzechGlobe, TAU, FUB, so all major processing facilities for airborne hyperspectral image data in Europe are included.

Finally 13 quality layers were agreed to be a common base, which each hyperspectral data provider should incorporate into the processing chain. According to differences among sensors and data processing approaches, each data provider may include additional quality layers, specific to their pre-processing chain.

Since 2004, the Global Change Research Centre – CzechGlobe (CVGZ, Academy of Sciences of the Czech Republic) has been operating the VNIR airborne hyperspectral sensor AISA Eagle. The AISA Eagle system is being produced by Spectral Imaging (Specim Ltd, Finland) company. A typical pre-processing of airborne hyperspectral data will be demonstrated in pre-processing chain which has been established at CzechGlobe including quality layers developed for the CzechGlobe pre-processing chain.

Keywords: airborne imaging spectroscopy, hyperspectral data processing, quality layers

INTRODUCTION

Airborne hyperspectral remote sensing (imaging spectroscopy) is still a relatively novel tool in the field of remote sensing [1]. Compared to traditional multispectral data, it offers a continuous coverage of electromagnetic spectra within their spectral range, where the so-called "spectral signatures" of the surface are acquired, rather than discrete values within broad spectral bands. The typical range of a hyperspectral sensor are the visible and near-infrared (VNIR) ranges, i.e. 400 – 1000 nm towards short-wave infrared (SWIR) within the 1000 – 2500 nm regions. This allows a development of new methods for Earth surface object detection including a high accuracy target detection and/or quantitative retrieval of surface properties.

The Global Change Research Centre (CVGZ, Academy of Sciences of the Czech Republic) has been operating the VNIR hyperspectral sensor AISA Eagle (Specim, Finland). The description of the AISA Eagle system, are given as follows.

AISA EAGLE SYSTEM DESCRIPTION

The AISA Eagle is a pushbroom airborne hyperspectral system which consists of a lightweight sensor head, data acquisition unit (rugged PC), GPS/INS unit, and downwelling irradiance sensor (FODIS). The system operates in the visible and near-infrared part of the spectra (VNIR). For the purpose of data geo-referencing a three-dimensional monitoring of the aircraft position and attitude is performed via a three-axial inertial navigation GPS/INS unit. Details of the system's basic technical specifications are shown in Tab.1.

Spectral range	400 – 1000 nm		
Spectral pixels	260		
Max. spectral resolution	2.4 nm		
Spatial pixels up to	1024, of which 71 FODIS pixels		
Spatial resolution	0.4 m – 6.0 m		
Camera	Progressive scan CCD camera		
Output	12 bits digital		
Integration time	Adjustable independently on image rate		
FODIS	Diffuse light collector and fibre optic cable		
Fore optics	23 mm	17 mm	11 mm
FOV [°]	29.9	39.7	58.4
IFOV [°]	0.029	0.039	0.057

Tab. 1 - Basic technical specifications of AISA Eagle hyperspectral sensor

The data acquisition set-up may vary in both the spatial (pixel size ranging from 0.4 to 6m) and spectral (spectral resolution from 3 up to 20mn) domain, based on flight altitude, optics used and pixel binning of the CCD matrix. Three different lenses with a field of view (FOV) of 29.9°, 39.7° and 58.4° can be used and even changed during the flight. The resulting data are a trade-off between the required resolution (both spatial and spectral) and signal-to-noise ratio (SNR). For examples of data acquisition set-up see Tab.2.

Ground pixel size [m]	Spectral resolution [nm]	Spectral bands	FOV [°]	Frame rate [Hz]	Swath width [m]	Flight height [m]
0.4	10	65	29.9	125.0	190	385
0.6	5	130	29.9	83.3	286	577
1.0	10	65	58.4	50.0	953	928
2.0	10	65	39.7	25.0	954	1426
6.0	2.5	260	58.4	8.33	2860	2790

Tab. 2 -Examples of a typical data acquisition set-up at a constant flight speed of 50 m/s

Fig. 1 - AISA Eagle on-board of a Cessna 206 aircraft

GROUND SUPPORTIVE CAMPAIGN

If a usage of hyperspectral data for scientific purposes is planned, excellent calibration and validation of hyperspectral data corrections will be necessary. In this case, it is necessary to carry out a supportive ground measurement campaign. On the other hand, for applications with lesser demands on data quality it is possible to perform simplified data corrections, i.e. FODIS corrections.

The reflectance ground measurements need to be acquired simultaneously (under the same illumination and weather conditions) to hyperspectral data acquisition. They are

required for calibration and validation in the procedure of data pre-processing. This includes: 1) atmospheric and geometric corrections of images, and 2) assessment of geometric accuracy and radiometric quality of surface reflectance values. Each flight/ground campaign is specific, depending mainly on the set-up of remote sensing data acquisition (e.g., targeting spatial resolution), and therefore needs to be based on user demands. The optical properties of reference targets are measured during image acquisition by a field portable spectroradiometer, e.g. ASD FieldSpec 4 (ASD Inc., USA). Spectral signatures measured are used for cross-checking the image data with surface reflectance measured as well as for additional calibration purposes.

Actual atmospheric conditions during data acquisition (aerosol optical thickness, water vapour content) are estimated by Microtops II Sunphotometer measurements.

Ground control points could be measured by means of GNSS receivers for geo-referencing accuracy assessment.

PRE-PROCESSING OF HYPERSPECTRAL DATA

Raw hyperspectral data of the AISA Eagle system need some basic pre-processing steps before their application by the end-users. Several software tools and packages have been developed for radiometric, geometric and atmospheric corrections of airborne remote sensing data. CaliGeo (Spectral Imaging Ltd.) is a software package specifically developed by SPECIM Ltd. to carry out the radiometric corrections and orthorectification of the raw AISA Eagle image data. The PARGE software [3], produced by ReSe Applications Schläpfer and Remote Sensing Laboratories (RSL) of the University of Zurich, is specialized in orthorectification of remote sensing images. Finally, ATCOR-4 [2] was developed by ReSe and Deutsches Zentrum fuer Luft- und Raumfahrt e. V. (DLR). ATCOR-4 is the software package designed for atmospheric, topographic and BRDF corrections of airborne spectroscopy image data. Atmospheric corrections implemented in ATCOR-4 are based on a physical model of the atmosphere MODTRAN5 [4]. PARGE and ATCOR-4 were developed as a complete package for orthorectification and atmospheric correction of airborne hyperspectral data and they were adjusted to perform atmospheric corrections even for non-orthorectified data.

Geo-referencing

Direct image orthorectification could be performed via PARGE or CaliGeo software. Data from the GPS/INS unit (geographic coordinates, altitude and attitude angles of the plane during image acquisition) and a digital elevation model (DEM) are compulsory for orthorectification in both software packages. Airborne data are mostly affected by geometric distortions caused by variations of the flight path and the attitude of the plane (roll, pitch, heading angle). Direct orthorectification is performed in two successive steps. First of all, the centre coordinates of all acquired pixels are calculated, and in the second step image data are resampled into a grid of the selected coordinate system. The process of orthorectification includes geometric corrections and image location to a desired map projection. Currently data from the AISA Eagle system are mostly orthorectified into the UTM projection, but orthorectification to another coordinate system is also possible.

Atmospheric corrections

Atmospheric correction is applied in order to remove the effect of the atmosphere (absorption by atmospherical gases and aerosols, etc.) and to produce a surface reflectance from the airborne images acquired. Several approaches to atmospheric correction can be employed.

1/ Empirical method

Acquired image spectra are forced to match the reflectance spectra of the reference target collected in the field during supportive ground measurements by means of an empirical statistical relationship. At least one reference target is required for calculation of the linear regeression of each band, however more reference targets will result in a higher accuracy of reflectance values.

2/ FODIS ratio

The whole image cube is divided by data acquired by the FODIS sensor that measures the incoming solar irradiance at the aircraft level per acquired band. The result is a sensor reflectance (atmospheric effects caused by the atmosphere between the aircraft and the ground remain uncorrected).

3/ Radiative transfer models

The most common and universal approach is using one of the atmospheric radiative transfer models, e.g. ATCOR-4 coupled with the MODTRAN4 atmospheric model. The ATCOR-4 software package also offers additional corrections of hyperspectral data, such as topographic correction, BRDF correction, etc.
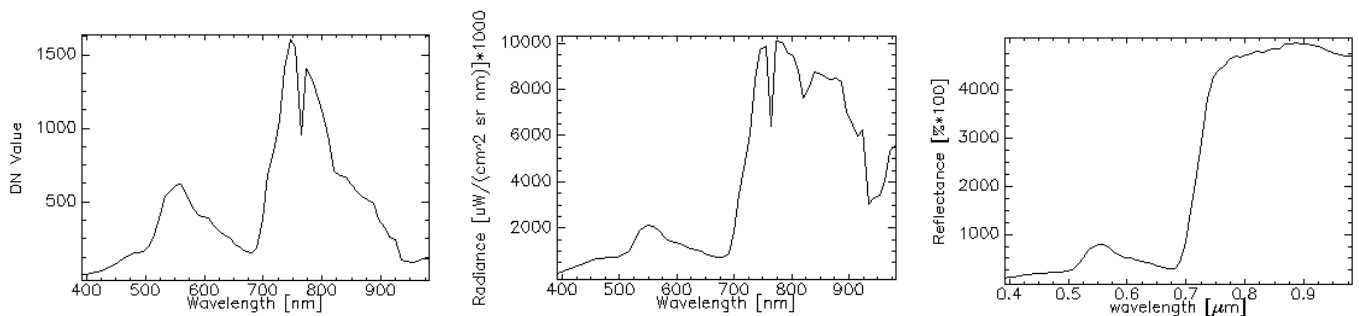
Fig. 2 – Spectral profile of a) raw acquired data, b) radiance, c) reflectance

QUALITY LAYERS

Numbers of hyperspectral data providers are now present for surveys in Europe. However, harmonized quality indicators and quality layers accompanying hyperspectral

data are often missing. That was the rationale for the submission of the FP7 EUFAR (www.eufar.net) project proposal on developing standardized quality layers for hyperspectral data. The proposal was selected for funding and became a Joint Research Activity (JRA) called HYQUAPRO. The role of CVGZ as one of HYQUAPRO partners and other partners is to develop and implement quality layers into an own hyperspectral data processing chain.

Finally 13 quality layers were agreed on as a common base, which each hyperspectral data provider should incorporate into the processing chain. According to differences among sensors and data processing approaches, each data provider may include additional quality layers, specific to their pre-processing chain. As an example, the following common quality layers were selected: saturation, problems with position and attitude information, synchronization problems, cloud and cloud shadow masks, etc. Each quality layer indicates spatial areas with reduced data quality as a result of the problems described (e.g. saturation, see Fig 3).
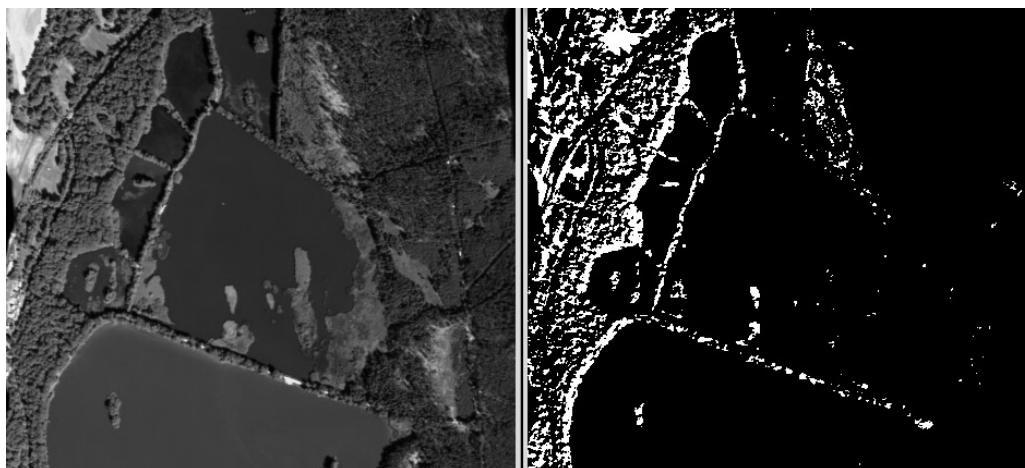

Fig. 3 - an example of a saturation quality layer, calculated for an AISA scene set up for water targets, therefore many land pixels are registered as saturated. On the left-hand side the image is displayed and on the right-hand side the appropriate quality layer.
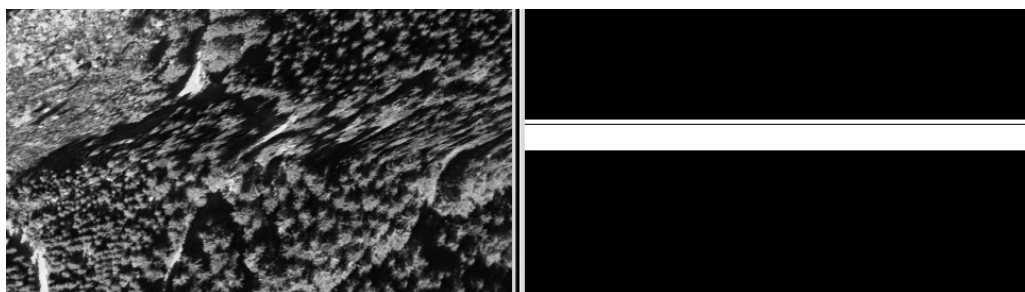

Fig. 4 - an example of a quality layer indicating reduced data quality due to rapid platform movement (roll) during data acquisition. On the left-hand side the image is displayed and on the right-hand side the appropriate quality layer.

DEVELOPMENT OF HYPERSPECTRAL REMOTE SENSING FACILITY AT CVGZ

The CVGZ as well as many other research teams in Europe see a future for remote sensing of hyperspectral data, therefore it makes sense to continue supporting and developing the imaging spectroscopy. CVGZ is the holder of the CzechGlobe (OP VaVpI) project and within this project the hyperspectral imaging facility at CVGZ will be significantly upgraded to cover a spectral range from 400 to 2500 nm (i.e. a full coverage of VNIR and SWIR spectral range). Moreover, a thermal data (LWIR spectral region) will be available as well. Nowadays are going on negotiations with AdMaS project concerning operating their laser-scanning system at the same airborne platform as hyperspectral facility of CVGZ. The first flying season with upgraded equipment is expected in the year 2014.

ACKNOWLEDGEMENTS

REFERENCES

[1]   Goetz, A. F. H. (2009). Three decades of hyperspectral remote sensing of the Earth: A personal view. Remote Sensing of Environment, 113, S5-S16. Elsevier Inc. doi: 10.1016/j.rse.2007.12.014.

[2]   Richter, R., 2007. Atmospheric/Topographic Correction for Airborne Imagery, ATCOR-4 User Giude, Version 4.2, Deutsches Zentrum fuer Luft- und Raumfahrt e. V. (DLR) and ReSe Applications Schläpfer, pp. 125. (http://www.rese.ch/atcor/atcor4/)

[3]   Schläpfer, D., 2006. Parametric Geocoding, PARGE User Guide, Version 2.3. ReSe Applications Schläpfer & Remote Sensing Laboratories University of Zurich, PDF/CDROM edition, Wil SG, pp. 195. (http://www.rese.ch/parge/)

[4]   A. Berk, G.P. Anderson, P.K. Acharya, E.P. Shettle ; MODTRAN 5.2.0.0 USER'S MANUAL

Appendix 6

Article 0b

POTENTIAL OF AIRBORNE IMAGING SPECTROSCOPY AT CZECHGLOBE

J. HANUŠ, T. FABIÁNEK, L. FAJMON

CzechGlobe – Global Change Research Institute CAS, 603 00, Bělidla 986, Brno, Czech Republic - hanus.j@czechglobe.cz

Commission TeS: WG I/2

KEY WORDS: Imaging Spectroscopy, Hyperspectral sensors, Airborne platform, Pre-processing chain

ABSTRACT:

Ecosystems, their services, structures and functions are affected by complex environmental processes, which are both natural and human-induced and globally changing. In order to understand how ecosystems behave in globally changing environment, it is important to monitor the current status of ecosystems and their structural and functional changes in time and space. An essential tool allowing monitoring of ecosystems is remote sensing (RS). Many ecosystems variables are being translated into a spectral response recorded by RS instruments. It is however important to understand the complexity and synergies of the key ecosystem variables influencing the reflected signal. This can be achieved by analysing high resolution RS data from multiple sources acquired simultaneously from the same platform. Such a system has been recently built at CzechGlobe - Global Change Research Institute (The Czech Academy of Sciences).

CzechGlobe has been significantly extending its research infrastructure in the last years, which allows advanced monitoring of ecosystem changes at hierarchical levels spanning from molecules to entire ecosystems. One of the CzechGlobe components is a laboratory of imaging spectroscopy. The laboratory is now operating a new platform for advanced remote sensing observations called FLIS (Flying Laboratory of Imaging Spectroscopy). FLIS consists of an airborne carrier equipped with passive RS systems. The core instrument of FLIS is a hyperspectral imaging system provided by Itres Ltd. The hyperspectral system consists of three spectroradiometers (CASI 1500, SASI 600 and TASI 600) that cover the reflective spectral range from 380 to 2450 nm, as well as the thermal range from 8 to 11.5 μm. The airborne platform is prepared for mounting of full-waveform laser scanner Riegl-Q780 as well, however a laser scanner is not a permanent part of FLIS. In 2014 the installation of the hyperspectral scanners was completed and the first flights were carried out with all sensors.

The new hyperspectral imaging system required adaptations in the data pre-processing chain. The established pre-processing chain (radiometric, atmospheric and geometric corrections), which was tailored mainly to the AISA Eagle instrument operated at CzechGlobe since 2004, has been now modified to fit the new system and users needs. Continuous development of the processing chain is now focused mainly on establishing pre-processing of thermal data including emissivity estimation and also on joint processing of hyperspectral and laser scanning data.

1. INTRODUCTION

1.1 Hyperspectral remote sensing at CzechGlobe

Airborne hyperspectral remote sensing (imaging spectroscopy) is an advanced tool in the field of remote sensing (RS) (Goetz, 2009). Compared to traditional multispectral sensors, which record the reflected solar radiation in several broad spectral bands, hyperspectral sensors record it into many narrow continuous spectral bands (Schaepman, 2009). Therefore imaging spectroscopy data provide almost contiguous spectral information about the Earth's surface in the optical domain of the electromagnetic spectra. A typical spectral range covered by hyperspectral sensors spans from the visible and near-infrared (VNIR) bands (i.e. 400 – 1000 nm) towards the short-wave infrared (SWIR) bands (i.e. 1000 – 2500 nm). Hyperspectal RS therefore brings an enhanced insight into spectral properties of Earth's surfaces. Furthermore, it stimulates a development of new methods for high accuracy Earth surface object detection and quantitative retrieval of surface properties (Kokaly et al., 2009).

Global Change Research Institute - CzechGlobe (CVGZ, Academy of Sciences of the Czech Republic) has been operating the VNIR hyperspectral sensor AISA Eagle (Specim Ltd., Finland) since 2004. In 2014 CzechGlobe has completed a new platform for advanced remote sensing called Flying Laboratory of Imaging Systems (FLIS). This paper introduces FLIS, i.e. an airborne carrier equipped with a suite of hyperspectral sensors and eventually a laser scanner, and further it introduces a pre-processing chain for hyperspectral RS data established at CzechGlobe.

1.2 Flying Laboratory of Imaging System (FLIS)

FLIS consists of an airborne carrier, a suite of hyperspectral sensors and eventually an airborne laser scanner.

The airborne carrier is a Cessna 208B Grand Caravan with two fuselage slits for imaging RS instruments (see Fig. 1). Both slits are equipped with an inertial measurement unit (IMU) and global navigation satellite system (GNSS) receivers POSAV410. Both systems allow near teal-time geo-processing of image data acquired by deployed imaging instruments.

The suite of airborne imaging spectroradiometers (hyperspectral system) consist of three sensors produced by the Canadian company ITRES Research Limited. The first sensor, CASI-1500, acquires data in the VNIR region. The second sensor, SASI-600, acquired data in the SWIR region and the last sensor TASI-600 covers the thermal infrared (LWIR) spectral region. Basic technical specifications of the FLIS hyperspectral systems are shown in Table 1.

The FLIS is prepared for installation of a full-waveform airborne laser scanner. For applications that require laser scanner data this instrument could rented and installed in the aircraft.

Sensor	CASI-1500	SASI-600	TASI-600
Region	VNIR	SWIR	LWIR
Spectral range [nm]	380 -1050	950 – 2450	8 000 – 11 500
Number of spatial pixels	1500	600	600
Max. spectral resolution [nm]	2.4	15	110
FOV [°]	40	40	40

Table 1. Basic technical specifications of the FLIS hyperspectral system.

2. VNIR, SWIR DATA PRE-PROCESSING CHAIN

The chain has been continuously improved by extending it with various processing schemes tailored to the CzechGlobe hyperspectral sensors and to the needs of RS data end-users.

If hyperspectral data are acquired for very demanding purposes, excellent calibration and corrections of the raw RS data is required. In this case, it is necessary to carry out a supportive ground measurement campaign, where additional data on surface reflectance, geometric accuracy of selected ground control points and atmospheric conditions are measured simultaneously to RS data acquisition. For other kinds of applications, it is possible to perform standard or simplified data corrections, i.e. by calculating so called apparent reflectance (described below). In the following sections we introduce the basic components of our pre-processing chain, i.e. radiometric, geometric and atmospheric corrections of airborne hyperspectral data and the related software tools and packages. In the Figure 1 are displayed spectral characteristics of both sensors after radiometric and atmospheric correction.

2.1 Radiometric correction

Radiometric corrections are performed by means of calibration parameters. Parameters are regularly obtained in CzechGlobe spectroscopic laboratory by procedure recommended by the sensor developer.

2.2 Atmospheric correction

Atmospheric correction is applied in order to remove the effect of the atmosphere (i.e., absorption and scattering by atmospheric gases and aerosols) and to convert at-sensor radiance values into at-surface reflectance. Atmospheric corrections are necessary in order to maintain the comparability of hyperspectral datasets acquired by different sensors, in different time and place. Several approaches of atmospheric correction can be employed.

2.2.1 Radiative transfer models: The most common and standard approach of atmospheric corrections is based on atmospheric radiative transfer models, e.g. MODTRAN or 6S. In our pre-processing chain we use the ATCOR-4 (Richter, 2007) software package for atmospheric corrections, which is based on the MODTRAN5 (Berk, et al., 2008) atmospheric model. Besides the atmospheric correction, ATCOR-4 offers additional corrections of hyperspectral data, such as nadir normalization and BRDF correction. For proper parameterization of the MODTRAN5 radiative transfer model it is necessary to estimate some atmospheric parameters. The atmospheric parameters can be either derived from hyperspectral data itself or measured in-situ. The main advantage of this approach is that it is a universal and robust method, independent of field measurements. The limiting factor of this approach is imperfect knowledge of atmospheric parameters.

2.2.2 Empirical method: In empirical methods of atmospheric correction, the acquired image spectra are forced to match the in-situ measured reflectance spectra of the reference targets. Most commonly, a simple linear regression is calculated between the image and in-situ spectra. At least one reference target is required to perform an empirical correction, however, more reference targets will increase the accuracy of corrections. The great advantage of this method is that it is simple and fast and it produces accurate solutions for an area close to reference target. The major disadvantage is that field measurements are needed.

2.2.3 Apparent reflectance: This approach is suitable for those RS applications, where the quality of RS data in not the highest priority. In this approach, an apparent at-sensor reflectance is calculated. It means that atmospheric effects caused by the atmosphere between the aircraft and the ground remain uncorrected. At-sensor apparent reflectance is calculated by dividing at-sensor radiance by incoming downwelling irradiance at the sensor level. The downwelling irradiance is measured by a hemispherical irradiance sensor mounted on the top of an airplane and the irradiance data are recorded simultaneously with the image data. This method is useful for mapping large or distant areas without proper knowledge of atmospheric parameters.
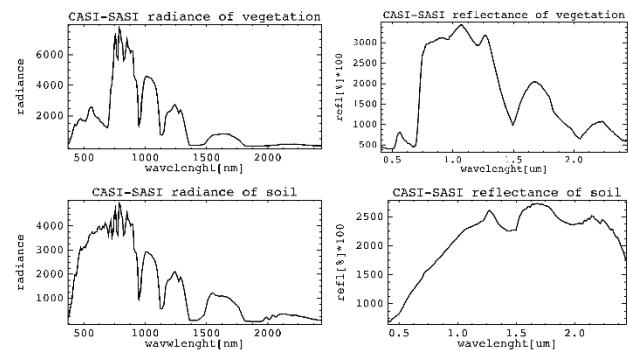

Figure 1. Example of spectral characteristics of CASI-SASI sensors after radiometric and atmospheric correction.

3. THERMAL DATA PRE-PROCESSING CHAIN

3.1 Radiometric correction

Radiometric corrections of measured data are performed using the program RadCorr Ver. 5.2.11.2. (Itres Ltd) and laboratory determined calibration parameters. Values of final image data are given in radiometric units, i.e. in $[\mu W\ cm^{-2}\ sr^{-1}\ nm^{-1}]$. Processed TASI data contain 22 spectral bands.

3.2 Atmospheric correction

Radiation measured by the sensor (L_m) is composed of radiation emitted by the surface, $\varepsilon\ B(T_s)$, reflected incoming radiation from the atmosphere, $(1 - \varepsilon)\ L{\downarrow}atm$, and direct radiation of the atmosphere, $L{\uparrow}atm$. These components can be written as the equation of radiative transfer:

$$L_m = \tau\ \varepsilon\ B(T_s) + \tau\ (1 - \varepsilon)\ L{\downarrow}atm + L{\uparrow}atm,$$

where τ is the transmittance of the atmosphere, ε is emissivity of the material, $B(T_s)$ is the radiation of black body at a temperature T_s, $L{\downarrow}atm$ is incoming radiation from the atmosphere and $L{\uparrow}atm$ is the radiation of the atmosphere only.

Variables $L{\downarrow}atm$. $L{\uparrow}atm$ and τ are determined by means of radiative transfer model MODTRAN 5.3. Model input is the actual state of the atmosphere, determined by the use of MOD07_L2 product from MODIS satellite images. After incorporating the variables in the equation of radiative transfer, we obtain the radiation escaping from the surface of the measured object:

$$LLL = \varepsilon\ B(T_s) + (1 - \varepsilon)\ L{\downarrow}atm,$$

which is the sum of emitted and reflected radiation. Examples of LLL radiance and consequent emissivity of a surface is shown in the Figure 2.
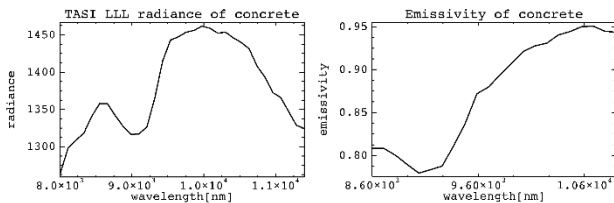

Figure 2. Example of spectral characteristics of TASI sensor after corrections.

4. GEO-REFERENCING

Geo-referencing of our airborne hyperspectral data is performed in two successive steps, direct image geocoding and resampling to a selected coordinate system. Direct image geocoding consists of geometric corrections and orthogonalization of image data. Geometric corrections compensate for image geometric distortions caused by variations in flight path and attitude of the plane (recorded as roll, pitch and heading angles by IMU). Orthogonalization compensates distortion caused by sensor acquisition geometry and surface topography.
After the geocoding step the image data are resampled into a grid of a desired coordinate system. Currently the image data are mostly transformed into the UTM map projection.
For image geo-referencing we use the PARGE software (Schläpfer, 2006). Additionally, we also use other sensor-specific software such as CaliGeo for the AISA images and GeoCorr for the ITRES sensors. All software packages require input data from the GNSS/IMU systems (i.e., geographic coordinates, altitude and attitude angles of a plane during the image acquisition) and a digital elevation/surface model (DEM/DSM) for image geo-referencing.

5. QUALITY ASSESMENT

It is recommended to verify the quality of the atmospheric correction by comparing at-surface reflectance to ground-measured spectra of selected homogenous, reference targets. Eventually, the measured reference spectra can be used for vicarious calibration. Quality of geo-referencing could be verified by means of Ground Control Points.

REFERENCES

Acharya, P.K., Anderson, G.P., Berk, A. and Shettle, E.P., 2008. MODTRAN® 5.2. 0.0 USER'S MANUAL.

Goetz, A.F.H., 2009. Three decades of hyperspectral remote sensing of the Earth: A personal view. Remote Sensing of Environment, 113, S5-S16. Elsevier Inc. doi: 10.1016/j.rse.2007.12.014.

Kokaly, R.F., Asner, G.P., Ollinger, S.V., Martin, M.E., & Wessman, C.A., 2009. Characterizing canopy biochemistry from imaging spectroscopy and its application to ecosystem studies. Remote Sensing of Environment, 113, S78-S91

Richter, R., 2007. Atmospheric/Topographic Correction for Airborne Imagery, ATCOR-4 User Giude, Version 4.2, Deutsches Zentrum fuer Luft- und Raumfahrt e. V. (DLR) and ReSe Applications Schläpfer, pp. 125. (http://www.rese.ch/atcor/atcor4/)

Schläpfer, D., 2006. Parametric Geocoding, PARGE User Guide, Version 2.3. ReSe Applications Schläpfer & Remote Sensing Laboratories University of Zurich http://www.rese.ch/parge/ PDF/CDROM edition, Wil SG, pp. 195.

Schaepman, M.E., 2009. Imaging Spectrometers. In T.A. Warner, M. Duane Nellis & G.M. Foody (Eds.), The SAGE Handbook of Remote Sensing (pp. 166-178). London (UK): SAGE